ASPECTS OF CURRENT SHEET THEORY

T. J. Tur

A Thesis Submitted for the Degree of PhD
at the
University of St Andrews

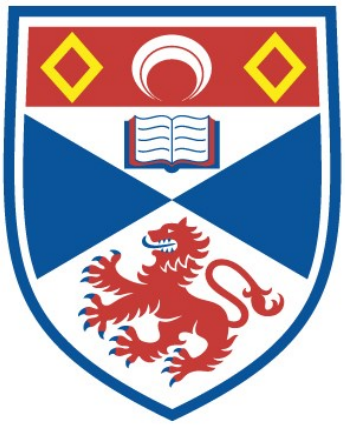

1977

A S P E C T S O F C U R R E N T S H E E T T H E O R Y

T. J. T U R

THESIS SUBMITTED FOR THE DEGREE OF DOCTOR OF PHILOSOPHY

OF THE UNIVERSITY OF ST. ANDREWS.

ProQuest LLC.
789 East Eisenhower Parkway
P.O. Box 1346
Ann Arbor, MI 48106 – 1346

ASPECTS OF CURRENT SHEET THEORY

Abstact

Current sheets are widely believed to play an important role in astrophysics when regions of magnetic flux are in motion. Several models based on the formation of current sheets have been proposed to explain such phenomena as geomagnetic storms, solar flares and prominences. In this thesis three aspects of current sheet theory are studied with particular reference to the solar flare problem.

Firstly the development of two-dimensional current sheets is investigated for several simple configurations. These include converging line current sources, converging and diverging line dipole sources and a dipole of increasing moment situated in either a uniform magnetic field or a constant dipole field. These last two may be thought of as modelling the emergence of bipolar flux from beneath the photosphere, a phenomena frequently observed prior to solar flares. The length, position and shape of the current sheet is determined from the requirement that the magnetic field be frozen-into the plasma. The sheet is found to be curved, except in the symmetrical case of converging line sources, In addition, the extra energy due to the presence of the current sheet is determined. Comparison with estimates of the energy dissipated during a flare indicate that the formation of current sheets may store an adequate amount of preflare magnetic energy, provided no reconnection occurs during the formation process.

A three-dimensional axi-symmetric model for current sheet formation is then considered. Two equal and

co-directional dipoles approach along the axis of symmetry to form an annular current sheet between them. The equations determining the magnetic field for this configuration are reduced to a single integral equation for the current density in the sheet as a function of radial distance from the axis. A numerical method is used to solve this integral equation. The inner and outer radii of the sheet are then determined from the conditions of flux conservation as for the two-dimensional case.

Finally the energetics of a current sheet that forms between newly emerging flux and an ambient field are considered. As more and more flux emerges, so the sheet rises in the solar atmosphere. The various contributions to the thermal energy balance in the sheet are approximated and the resulting equation is solved for the internal temperature of the sheet. It is found that, for certain choices of the ambient magnetic field strength and velocity, the internal temperature increases until, when the sheet reaches some critical height, no neighbouring stable state exists. The temperature then increases rapidly seeking a hotter branch of the solution curve. During this dynamic heating the threshold temperature for the onset of microinstabilities may be attained. It is suggested that this may be a suitable trigger mechanism for the recently proposed "emerging flux" model of a solar flare.

To Rebecca

ACKNOWLEDGEMENTS

I would like to thank Dr. Eric Priest for his continued encouragement and supervision during the past three years. My thanks are also due to many colleagues at St. Andrews and elsewhere for their helpful advice and discussion, especially Drs. George Phillips, Bernard Roberts, Mike Raadu and Jean Heyvaerts.

I also wish to thank my wife, Martine, for her help in preparing the manuscript and diagrams, and to Mrs. D. Woods for bravely typing this thesis.

I am grateful to the Science Research Council for financial support.

DECLARATION.

I declare that the following thesis is a record of research work carried out by me, that the thesis is my own composition, and that it has not been previously presented in application for a higher degree.

(TIMOTHY JOHN TUR)

POSTGRADUATE CAREER.

I was admitted into the University of St. Andrews as a research student under Ordinance General No. 12 in October 1973 to work on aspects of current sheet theory under the supervision of Dr. E.R. Priest. I was admitted under the above resolution as a candidate for the degree of Ph.D. in October 1974.

CERTIFICATE

I certify that Timothy J. Tur has satisfied the conditions of the Ordinance and Regulations and is thus qualified to submit the accompanying application for the degree of Doctor of Philosophy.

C O N T E N T S

1. INTRODUCTION

1.1 A PHYSICAL BACKGROUND TO SOLAR FLARES.

When a highly-conducting, magnetized plasma is subjected to sufficiently large velocity fields, current sheets may be expected to form about any line of intersection between independent flux systems. Such conditions are not uncommon in astrophysics, and one has only to look at the earth's magnetosphere or the solar atmosphere to find suitable examples. In the magnetosphere, a current sheet is likely to form where the magnetic field present in the tenuous plasma of the solar wind presses up against the earth's own field. Also, current sheets are widely believed to play an important role in the solar flare phenomenon.

In this thesis, the solar flare problem has been the chief application for the current sheet theory considered. However, many of the results will be more generally valid. Some of the physical properties of flares are reviewed below.

When we observe solar flares, we are probably witnessing the most violent and energetic transient phenomena in the entire solar system. During a flare of typical magnitude, the energy released is about one million times that of the largest recorded earthquake (of order 3×10^{19} j). As well as being highly energetic, solar flares exhibit wide variety in both form and energy spectrum. Although most flares are observed as a rapid brightening in H_α, maximum intensity being reached within a few minutes of the onset,

this is only one component of the total emission that ranges from radio waves, through all regions of the electromagnetic spectrum, to cosmic rays. In addition, quantities of plasma may be injected into the overlying solar atmosphere (for example, 10^{13} Kg at around 10^{6} ms^{-1}), and particles accelerated up to relativistic velocities. Electrons having energies of 3 MeV, and high energy nuclei to 30 GeV have been observed. The entire flare may last typically about an hour.

The first requirement of a flare model, therefore, is to explain the large amount of energy dissipated. It varies from about 10^{22}j for the so-called sub-flare, to 4×10^{25}j for major events. For larger flares, the distribution of energy has been estimated by De Jager (1969, p 2.) and is summarised in Table 1.

TABLE 1.

The approximate distribution of energy for a typical large flare.

SOURCE	Energy (Joules)
Electromagnetic radiation up to soft X-rays	10^{25}
Interplanetary blast wave	2×10^{25}
Fast electrons (hard X-rays)	5×10^{24} *
Subrelativistic particles	2×10^{24}
Relativistic particles	3×10^{24}
All other particles	10^{23}
Total	4×10^{25}

*More recently, Brown (1975) has suggested that the hard X-ray component may be as high as 2×10^{25}j, giving a total energy output around 35% higher than earlier estimates.

Many of the available energy sources (e.g. thermal and gravitational) are far too small to explain the huge quantities released, while others, such as dynamic and thermonuclear processes can be ruled out on the basis of observation. In the latter case, for example, any reactions would be detectable by their spectra and neutron emission. Only the magnetic field can adequately account for such high energy output. For example, 10^{25}j would be released during the complete annihilation of a 0.01 tesla field contained in a volume 10^{23} m^3 (the size of an active region extending about 10^8m across the solar disc and 10^7m in height). In practice, active region field strengths vary typically between some 10^{-4} tesla in the corona up to a few tesla in the vicinity of underlying sunspots and the magnetic energy associated with a large active region of the size quoted above may greatly exceed 10^{25}j. In that case sufficient energy for a flare would be released by the conversion of only a small percentage of the total magnetic energy of the region.

Many of the observed properties of solar flares support the assumption that they derive their energy from photospheric, chromospheric or coronal magnetic fields. Firstly, flares rarely occur outside active regions; Dodson and Hedeman (1970) found that, during the period 1959 to 1968, only 7% of all major flares observed occurred in the "quiet" regions. Furthermore Giovanelli (1939) noted that flares are correlated with the more complex sunspot groups in which the magnetic fields are highly contorted and sheared. Simple unipolar and bipolar groups give rise to a lower proportion of flares.

There are no large scale changes in the underlying photospheric magnetic field at the time of a flare (Rust, 1972), indicating that the

energy is not derived from the annihilation of photospheric flux. However, small scale changes are sometimes observed during large flares, (Matres et al., 1971; Harvey, 1974), but the precise nature of these changes is not fully understood.

Other important aspects of the solar flare phenomenon are the wide variety of the electromagnetic emission produced and the intensity profile associated with each component. Figure 1 shows, schematically, the simultaneous intensity curves at several wavelengths. The time develop ment of a typical large event can be conveniently divided into four stages: the preflare, impulsive, flash and main phase.

Before a flare is observed in H_{α} , preflare activity may be revealed by emission of relatively low intensity in the extreme ultra-violet (e.u.v.) and soft X-ray region of the spectrum. The duration of this phase is usually about ten minutes, but probably only represents the final stages of a much larger preflare period in which energy is somehow stored by the magnetic field.

The flash phase, in which the emission intensity and area of the flare rapidly reach their maximum, lasts typically about five minutes. In many flares, the first minute or so of the main phase may be dominated by a distinct "impulsive" phase, typified by microwave, e.u.v. and hard X-ray bursts with sharply peaked intensity profiles (see Figure 1).

Finally in the main (or decay) phase, the intensity gradually falls off on a time scale of an hour or more.

The precise height at which a flare occurs, or is initially triggered, remains largely undecided. Syrovatskii (1966) argues for

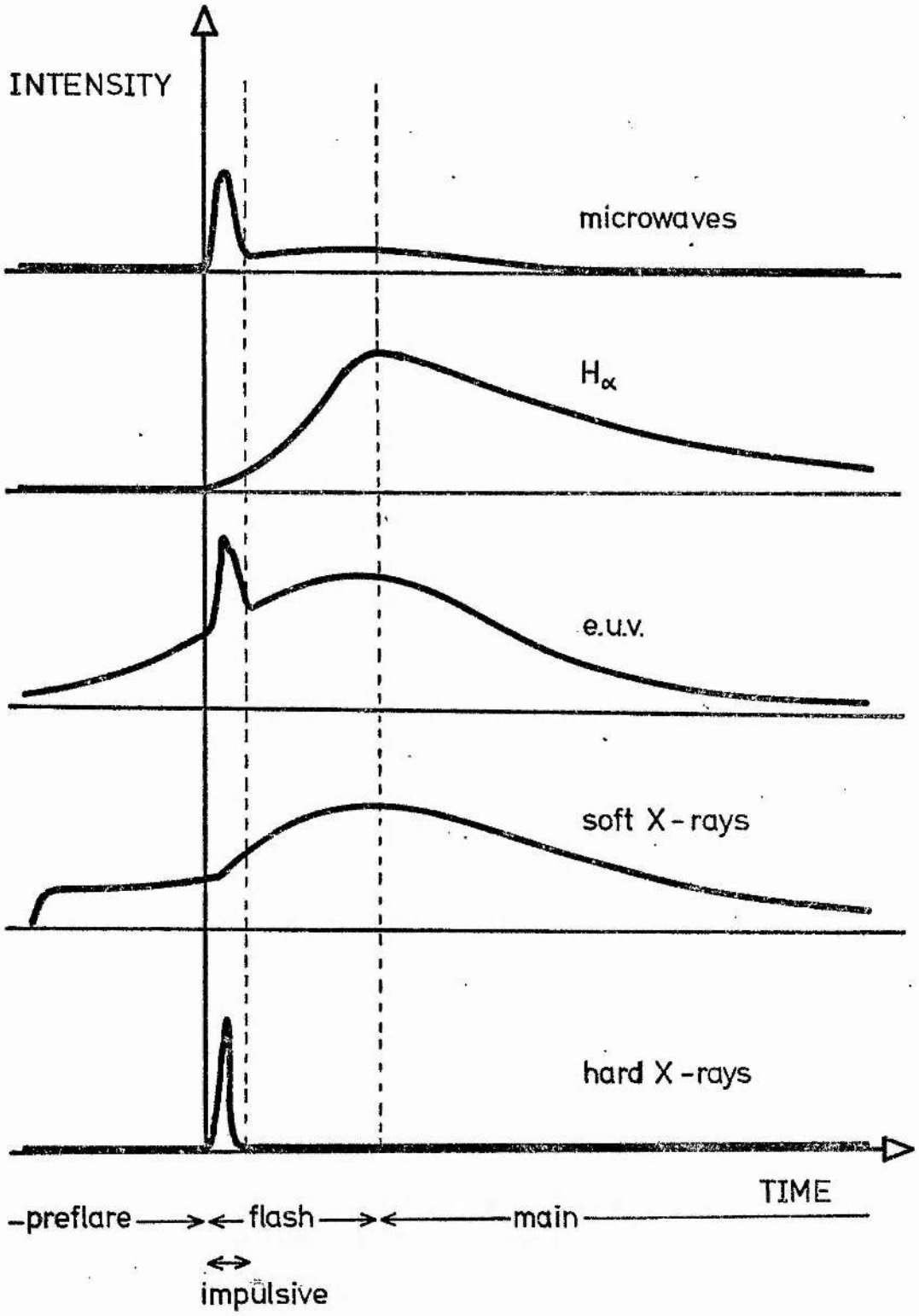

Figure 1.

Schematic representation of some of the intensity profiles at various wavelengths during a solar flare. Some phases or wavelengths may not be present during any one flare. (From Priest, 1976).

a site which is low in the solar atmosphere whereas Švestka (1973) suggests that the initial phase occurs high in the chromosphere or lower corona, and that the H_{α} component, observed in the lower chromosphere, is merely a secondary stage of the flare process. He estimates the lower limit of the altitude of the flare origin as being in the low corona or transition region. However each solar flare manifests itself over a large range of heights, and it is likely that different heights may be involved for each separate event.

Solar flares exhibit a wide variety of structures, giving important clues to their physical character and suggesting theoretical models. A classification according to morphological type would produce an extensive list. Zirin (1974) gives a short list of some of the more common types, which includes (among others):

1. The large "two-ribbon" flares.

These events may start at several points that eventually coalesce to form two strands (viewed in H_{α}) separated by a polarity inversion line, that is, a line along which the magnetic field changes polarity. The two ribbons are often seen to move slowly outwards after the flash phase. Being invariably large events they are usually of longer than average duration (Smith and Smith, 1963, p. 67), and indeed may last for several hours. The huge flare of August 7, 1972 was of this type. This event lasted over three hours, with a flash phase of nearly fifteen minutes (Zirin and Tanaka, 1972). A steady increase in the intensity of the soft X-ray component was recorded by satellite borne instruments (OSO 7) some five hours before the start of the flare (c.f. Figure 1). The event was accompanied by microwave and hard X-ray bursts during the

impulsive phase (Rust and Hegwar, 1975) and radio emission whose peak coincided with that of the $H\alpha$ flash phase. The two ribbons moved steadily outwards with a velocity of 2×10^3 ms^{-1}. Observations of the active region in which this flare occurred has provided one of the most detailed and comprehensive flare studies in recent years.

2. Explosive flares.

These can be small events, but as highly energetic as the two-ribbon flare. They take the form of an outward eruption from a relatively small bipolar source, situated near the edge of a large active region. Their energy is released in a relatively short time and in a confined area.

3. Surge flares.

Unlike the two-ribbon events surge flares are usually small in terms of energy and size. Their distinguishing characteristic is the surge of the material which erupts from the central region of the flare. This may propagate in any direction, but is well collimated for a given event, the motion of the plasma being (presumably) determined by the magnetic field.

Further clues to the mechanisms responsible for solar flares are provided by observations of the precise location, relative to the ambient magnetic field, at which events occur. Severny (1958) noticed that flares frequently occur near polarity inversion lines. There has been much evidence to substantiate this point (e.g., Rust, 1972) including the observations of the great August 1972 flares, already mentioned. Furthermore the points at which transverse

magnetic fields apparently cross over, and regions of high electric current density are favoured by flares (Severny, 1959, p. 38).

Another important observation is the high correlation between flaring and the emergence of new magnetic flux from below the photosphere (Zirin, 1974; Matres et al., 1968; Rust, 1972; Vorpahl, 1973). New flux may often emerge in the form of small satellite sunspots near the edge of large sunspot groups (Rust, 1968). The presence of emerging flux regions (which in many cases must produce magnetically neutral lines) has led Heyvaerts et al., (1976) to produce a flare model that tries to be more consistent than hitherto with observations. They suggest that solar flares occur in three stages as loops of new magnetic flux emerge from below the photosphere. Firstly, during the preflare phase, steady reconnection occurs between the emerging and ambient magnetic fields, heating the plasma and giving rise to soft X-ray emission. The emerging flux loops then reach a critical height at which they are no longer in a state of equilibrium and rapidly heats up seeking a new equilibrium. During this stage, the current density may exceed the threshold value for the onset of microinstabilities giving rise to the impulsive phase characterised by its hard X-ray component. Finally, in the main phase of the flare, a new state of field reconnection is reached with a turbulent current sheet between the ambient and upgoing magnetic field. The type of flare produced by this mechanism will depend on the environment into which flux emerges. For example, if the strong, twisted magnetic field surrounding a filament near the centre

of an active region is near the site of flux emergence, a two-ribbon flare may occur.

Lastly there are two properties of solar flares that cannot be overlooked when trying to present a comprehensive picture, namely, homology and sympathy. Homologous flares occur at the same place and with similar physical characteristics, at intervals of up to one hour. Surge flares may exhibit homology, the surge itself moving in the same direction for each event, (Zirin, 1966, p. 399). A sympathetic flare is one which appears to have been triggered by another flare, possibly at some large distance away. Surface waves are often observed propagating outwards from a flare (Moreton and Ramsey, 1960), and it is therefore conceivable that disturbances such as these could, in some way, trigger further flares. However evidence for a direct link between concurrent flares is lacking, and doubts concerning its existence have been expressed by Fritzova-Švestkova et al. (1976).

1.2. THE BASIC MAGNETOHYDRODYNAMIC EQUATIONS

The basic aim of magnetohydrodynamics (M.H.D.) is to study the behaviour of a conducting fluid in a magnetic field.

One usually starts with Maxwell's equations (M.K.S. units)

$$\nabla \times \underline{H} = \underline{j} + \frac{\partial \underline{D}}{\partial t} \quad , \tag{1.1}$$

$$\nabla \cdot \underline{B} = 0 \quad , \tag{1.2}$$

$$\nabla \times \underline{E} = -\frac{\partial \underline{B}}{\partial t} \quad , \tag{1.3}$$

and

$$\nabla \cdot \underline{D} = \rho_c \quad , \tag{1.4}$$

for the magnetic and electric fields $\underline{H}$ and $\underline{E}$ respectively where $\underline{j}$ denotes the electric current density and ρ_c the charge density. The magnetic induction $\underline{B}$ and the electric displacement $\underline{D}$ are related to the fields $\underline{H}$ and $\underline{E}$ by the constitutive relations

$$\underline{D} = \epsilon \underline{E} \quad , \tag{1.5}$$

and

$$\underline{B} = \mu \underline{H} \quad , \tag{1.6}$$

where ϵ is the dielectric constant of the medium and μ the magnetic permittivity (ϵ_0 and μ_0 in a vacuum).

In M.H.D. some simplifying assumptions to Maxwell's equations are usually made. Firstly, and most importantly, non-relativistic velocities are assumed, and the displacement current $\partial \underline{D}/\partial t$ in equation (1.1) may therefore be ignored in comparison with the remaining terms, equation (1.1) then becomes

$$\nabla \times \underline{H} = \underline{j} \tag{1.7}$$

Secondly, only slow time variations are considered. Finally a large electrical conductivity, ( ) is often(although not always) assumed and so from Ohm's Law

$$\frac{1}{\sigma}\,\underline{j} = (\underline{E} + \underline{v} \times \underline{B}) \quad , \tag{1.8}$$

one has

$$|\,\underline{E}\,| \simeq |\,\underline{v} \times \underline{B}\,| \; .$$

These assumptions can be readily justified for the solar atmosphere where the observed motions of the plasma are always at sub-relativistic speeds (e.g. 10^4 ms^{-1}), and length scales between 10^5m and 10^7m apply.

For a complete description of a conducting fluid, the electromagnetic field equations must be supplemented by the equations of motion of the plasma. In M.H.D. these are taken to be just the fluid dynamical equations which are valid whenever the motions are dominated by collisions between particles; in other words, the typical length scale for the problem concerned is much greater than the particle mean free path. The density ρ is given by the equation of continuity,

$$\frac{D\rho}{Dt} + \rho \nabla \cdot \underline{v} = 0 \tag{1.9}$$

or simply

$$\nabla \cdot \underline{v} = 0 \tag{1.10}$$

in an incompressible medium. D/Dt is the convective derivative

$$\frac{D}{Dt} \equiv \frac{\partial}{\partial t} + (\underline{v} \cdot \nabla) \ .$$

The momentum equation becomes

$$\frac{D\underline{v}}{Dt} = -\nabla p + \underline{j} \times \underline{B} + \underline{F} \quad , \tag{1.11}$$

where the Lorentz force $\underline{j} \times \underline{B}$ (per unit volume) has been included, $\underline{F}$ represents any other forces such as gravity or viscosity that may be present, and p is the hydrostatic pressure of the fluid. An equation of state provides a relationship between the pressure, density and temperature T. For a perfect gas this is

$$p = \rho R T \quad , \tag{1.12}$$

where R is the gas constant. Finally, the temperature may be obtained from a suitable energy equation.

An important consequence of Maxwell's equations and Ohm's law may be obtained by eliminating $\underline{E}$ and $\underline{j}$ between equations (1.3) (1.7) and (1.8). The elimination yields

$$\frac{\partial \underline{B}}{\partial t} = \nabla \times \left[\underline{v} \times \underline{B} - \frac{1}{\sigma} \nabla \times (\underline{B}/\mu) \right] \quad ,$$

which assuming μ and σ to be independent of position, reduces to

$$\frac{\partial \underline{B}}{\partial t} = \nabla \times (\underline{v} \times \underline{B}) + \eta \nabla^2 \underline{B} \quad , \tag{1.13}$$

the so-called induction equation. The constant

$$\eta = \frac{1}{\mu \sigma} \tag{1.14}$$

is known as the magnetic diffusivity.

By choosing ℓ_0, v_0 and B_0 to be typical length, velocity and magnetic field scales respectively the induction equation may be written in terms of the dimensionless variables

$$\underline{B}' = \underline{B}/B_0 \quad , \quad t' = tv_0/\ell_0 \quad , \quad \underline{v}' = \underline{v}/v_0 \quad \text{and}$$

$$\nabla' = \ell_0 \nabla \quad , \quad \text{as}$$

$$\frac{\partial \underline{B}'}{\partial t'} = \nabla' \times (\underline{v}' \times \underline{B}') + \frac{\eta}{\ell_0 v_0} \nabla'^2 \underline{B}' \quad .$$

Dropping the primes and defining the magnetic Reynolds' number

$$R_m = \ell_0 v_0 / \eta \quad , \tag{1.15}$$

the dimensionless induction equation becomes

$$\frac{\partial \underline{B}}{\partial t} = \nabla \times (\underline{v} \times \underline{B}) + \frac{1}{R_m} \nabla^2 \underline{B} \quad . \tag{1.16}$$

Now, for most astrophysical applications, R_m will be large compared to unity and the second term on the right hand side of equation (1.16) may reasonably be omitted. In the sun's chromosphere, for example, taking $\ell_0 = 10^5$ m , $v_0 = 10^4$ ms^{-1} , as before, and $\eta \simeq 2 \times 10^2$ m^{2}s^{-1}, the magnetic Reynolds' number is of order 5×10^6 .

The reduced induction equation

$$\frac{\partial \underline{B}}{\partial t} = \nabla \times (\underline{v} \times \underline{B}) \ , \tag{1.17}$$

for $R_m \gg 1$, has a useful physical interpretation, namely that the plasma cannot move perpendicular to the magnetic lines of force. That is to say, the magnetic field is embedded or "frozen-in" to the plasma. A proof of this theorem, due to Alfvén, can be found in most textbooks on M.H.D. (e.g. Ferraro and Plumpton, 1966, p. 19). Equation (1.17) also results in the case of a perfect conductor, since σ , or equivalently R_m , tends to infinity. Ohm's law then becomes approximately

$$\underline{E} + \underline{v} \times \underline{B} = 0 \quad .$$

Over much of the solar atmosphere (see Table 2) two simplifying

assumptions may be made to the momentum equation. When β given by

$$\beta = \frac{2\mu p}{B^2} \quad , \tag{1.18}$$

is much less than unity the hydrostatic pressure gradient may be neglected in comparison with the Lorentz force. Next, for plasma speeds well below the Alfvén speed,

$$v_A = \frac{B}{\sqrt{\mu\rho}} \quad ,$$

the convective term may also be ignored.

TABLE 2

The ratio of hydrostatic to magnetic pressure (β) and the Alfvén speed (v_A) for some regions of the solar atmosphere (adapted from Zirin, 1966, p. 373)

Region	Number Density (m^{-3})	Temperature (^oK)	Magnetic Field (tesla)	β	v_A (ms^{-1})
Photosphere (quiet)	10^{21}	6×10^3	10^{-4}	2×10^4	7×10^1
Photosphere (active)	10^{21}	6×10^3	5×10^{-3}	8×10^1	35×10^3
Sunspot	10^{21}	4×10^3	10^{-1}	10^{-2}	7×10^4
Chromosphere (quiet)	10^{19}	7×10^3	10^{-4}	25×10^2	7×10^2
Chromosphere (active)	10^{19}	2×10^4	5×10^{-3}	3×10^{-1}	35×10^4
Corona	10^{15}	10^6	5×10^{-3}	14×10^{-4}	35×10^6

Thus the equation of motion simply reduces to

$$\underline{j} \times \underline{B} = 0 \qquad (1.19)$$

for which two possibilities exist. Firstly $\underline{j}$ may be identically zero and the magnetic field is therefore governed by Laplace's equation. Alternatively if $\underline{j}$ is non-zero, but everywhere parallel to $\underline{B}$, then equation (1.19) and the field is said to be force-free. Using equations (1.6) and (1.7) the condition for a force-free field becomes

$$\nabla \times \underline{B} = \alpha \underline{B} \quad , \qquad (1.20)$$

where α is some scalar which, in general, may be a function of position. Taking the divergence of equation (1.20) and using equation (1.2) one finds that

$$(\underline{B} \cdot \nabla) \alpha = 0 \quad , \qquad (1.21)$$

and so α is a constant along each magnetic field line. For the special class of force-free fields in which α is independent of position, the curl of equation (1.20) gives

$$\nabla \times (\nabla \times \underline{B}) = \alpha \nabla \times \underline{B} \quad ,$$

which using equations (1.2) and (1.20) again yields

$$(\nabla^2 + \alpha^2) \underline{B} = 0 \qquad (1.22)$$

The potential field may therefore be regarded as a special case of the force-free field for which α is everywhere zero.

The energy W associated with a magnetic field $\underline{H}$ in a volume v is given by

$$W = \frac{1}{2} \int \underline{B} \cdot \underline{H} \, dv \quad ,$$

or when μ is independent of position

$$W = \frac{1}{2\mu} \int_V |\underline{B}|^2 \, dv \quad . \tag{1.23}$$

It is known that, if the normal component of magnetic field $\underline{B} \cdot \underline{n}$ is prescribed as the boundary S of a fixed, finite region v, then a condition that the magnetic energy W be a minimum is

$$\nabla \times \underline{B} = 0 \quad .$$

A proof of this theorem may be found, for example, in Roberts (1967, p. 112). An alternative proof in which v may become infinite is outlined below.

Let the variation in energy corresponding to a magnetic field variation of $\delta \underline{B}$, be δW. Then from equation (1.23) and the divergence theorem

$$\delta W = \frac{1}{2\mu} \int_V |\delta \underline{B}|^2 dv + \frac{1}{\mu} \int_S (\delta \underline{A} \times \underline{B}) d\underline{S} + \frac{1}{\mu} \int_V \delta \underline{A} \cdot (\nabla \times \underline{B}) dV, \tag{1.24}$$

where $\delta \underline{A}$ is just the variation in the vector potential $\underline{A}$ for the magnetic induction. For finite regions the boundary condition may

be conveniently written, using the integrated form of Maxwell's equations, as

$$\hat{\underline{n}} \times \delta \underline{A} = -\hat{\underline{n}} \times \nabla \delta\phi \quad , \qquad \text{on } s, \tag{1.25}$$

for some scalar potential ϕ (Roberts, 1967, p. 27). Substituting into the surface integral in equation (1.24), the first order terms in δW are

$$\frac{1}{\mu}\int_S \delta\phi\,(\nabla\times\underline{B}).d\underline{S} - \frac{1}{\mu}\int_S \nabla(B\delta\phi).d\underline{S} + \frac{1}{\mu}\int_V \delta\underline{A}\,.\nabla\times\underline{B}\,dV \quad . \tag{1.26}$$

From the divergence theorem the second integral is clearly zero, while the remaining ones imply an extremum when

$$\nabla \times \underline{B} = 0 \quad .$$

Furthermore, the higher order term,

$$\frac{1}{2\mu}\int_V |\delta \underline{B}|^2 \quad dV \quad ,$$

is positive definite, and the extremum is therefore a minimum.

For infinite regions, the boundary condition must be replaced by the requirement that the surface integral

$$I_s = \frac{1}{\mu} \int_S (\delta \underline{A} \times \underline{B}) \cdot dS \qquad (1.27)$$

in equation (1.24) must vanish in the limit as S tends to infinity. Writing $\delta \underline{A}$ in terms of its components parallel and perpendicular to $\underline{B}$, $\lambda \underline{B}$ and $\underline{\xi} \times \underline{B}$ respectively, I_s becomes

$$I_s = \frac{1}{\mu} \int_S (\underline{\xi} \times \underline{B}) \times \underline{B} \cdot d\underline{S} \quad , \qquad (1.28)$$

where λ and $\underline{\xi}$ are functions of position. Now if the magnetic field strength $|\underline{H}|$ falls off faster than some power of the distance L from the origin,

$$|\underline{H}| \leq L^n \quad , \qquad (1.29)$$

for some index n, then I_s is bounded above by

$$I_s^* = |\underline{\xi}| \, L^{2n+2} \quad , \qquad (1.30)$$

for sufficiently large L. In the limit $L \longrightarrow \infty$ ($S \longrightarrow \infty$), I_s^* tends to zero providing n is strictly less than -1. This condition is clearly satisfied by many naturally occurring magnetic field configurations including dipolar fields.

The above theorem may be extended to semi-infinite regions for which $\underline{B} \cdot \hat{\underline{n}} = 0$ on some bounding surface S and $|\underline{B}|$ falls off faster than $1/L$ elsewhere. This result is particularly useful when considering the field above a (bipolar) sunspot group, the photospheric surface being represented by S.

One may deduce similar results for the more general force-free

fields. Woltjer (1958a) has constructed an elegant proof that the magnetic energy has an extremum, subject to the additional constraint that $\delta \underline{A}$ vanishes at the boundary when the field is force-free. However, it does not immediately follow that this extremum represents a minimum. The higher order variations $\delta_2 W$ are found to be

$$\delta_2 W = \frac{1}{\mu} \int_V \left[\quad |\delta \underline{B}|^2 - \alpha \, \delta \underline{A} \cdot \delta \underline{B} \right] dV \ , \qquad (1.31)$$

and hence more information about α and $\delta \underline{B}$ is required before the nature of the equilibrium can be decided. In fact both maxima and minima exist, even for the limited case in which is constant. (Voslamber and Callebout, 1962, Woltjer, 1958a).

1.3. CURRENT SHEET THEORY.

The theory of current sheets in a magnetized plasma can be broadly divided into three parts: their formation and development, the reconnection process, and finally their stability. In this section some aspects of current sheet theory are reviewed under these general headings.

A. Current Sheets.

Dungey (1953) first showed that an X-type neutral point in a current-free magnetic field is locally unstable if their are no constraints on the sources of the field. He considers the (initially) current-free field

$$\underline{H}_0 = (y, x, 0) \ , \qquad (1.32)$$

in which the magnetic field lines form a family of rectangular hyperbolae (Figure 2 (a)). The limiting field lines $y = \pm x$ that pass through the origin are often termed the separatrices. If the field is now perturbed so that $\underline{H}$ becomes

$$\underline{H} = (y, (1 + \epsilon)x, 0), \qquad (\epsilon > 0), \tag{1.33}$$

the field lines close up as shown in Figure 2 (b). The current density produced by the perturbation is, using equations (1.7) and (1.33)

$$\underline{j} = (0, 0, \epsilon),$$

and the resulting Lorentz force

$$\underline{j} \times \underline{B} = (-(1 + \epsilon)\epsilon x, \epsilon y, 0). \tag{1.34}$$

The perturbed field is therefore subject to a force whose x-component is directed towards the origin and the y-component away. It is therefore unstable, the field lines tending to close further while the current density increases in magnitude.

Intuitively, one can envisage the collapsing X-type neutral point as a simple model for current sheet formation, the neutral point constricting itself into a thin sheet along the y-axis near to the origin. This idea was used by Sweet (1958) in setting up his model for the reconnection process. However, instead of the above local analysis, he considers the motions of the field lines to be externally generated, producing a current sheet (shown in Figure 2(c))

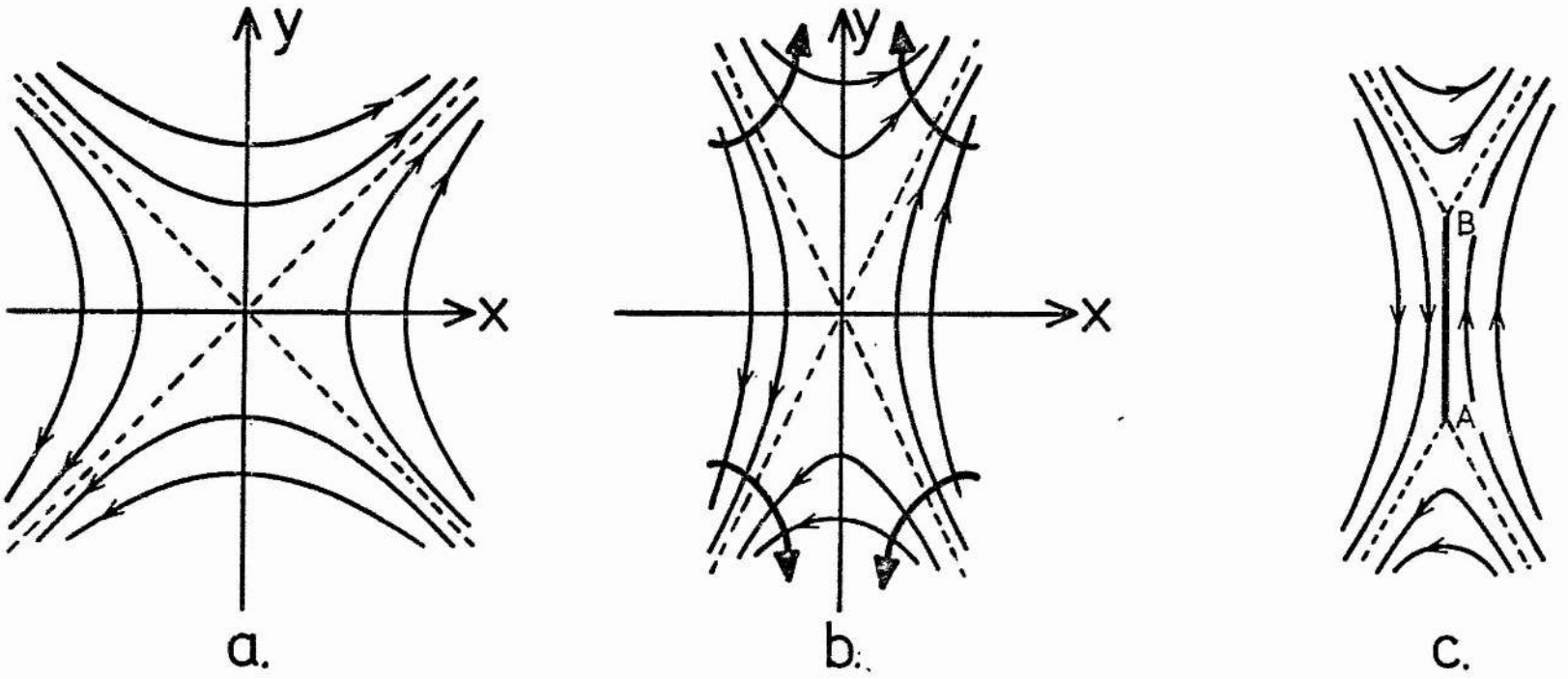

Figure 2.

The collapse of an X-type neutral point to form a current sheet.

(a) The initial magnetic field lines, (the separatrix is dashed).

(b) Collapsing field. The $\underline{j} \times \underline{B}$ forces are indicated by heavy arrows.

(c) Current sheet (AB) formed about the former X-type neutral point.

about the former neutral point.

The local analysis of the collapse of an X-type neutral point is however, unsuited when considering phenomena occurring in the solar atmosphere, where the motions of the field lines are governed by conditions at some distance from the neutral points (or lines). Syrovatskii (1966) demonstrated the formation of current sheets in a non-local analytic treatment, although some major physical assumptions were necessary. The essence of his method is outlined below.

The two-dimensional magnetic field that results from parallel line sources at $x = \pm a$, (c.f. Figure 4 (a)), contains an X-type neutral point at the origin. For $r = (x^2 + y^2)^{\frac{1}{2}} \ll 1$, the field strength $\underline{H}$ reduces to the form of equation (1.32), while the vector potential $\underline{A}$ is perpendicular to the (x, y)-plane and has magnitude

$$A_0(x, y) = \frac{1}{2}(y^2 - x^2), \qquad (r \ll 1). \tag{1.35}$$

Syrovatskii considers the effects of a small (compared to unity) displacement of the line sources towards each other. He finds that, to first order, the field strength $\underline{H}$ remains unaltered as

$$\underline{H} = (y, x, 0) \quad ,$$

while the potential becomes

$$A(x, y) = \frac{1}{2}(y^2 - x^2 - 2\delta), \quad (r_s \ll r \ll 1) \tag{1.36}$$

where r_s is the distance from the origin at which the Alfvén and

sound speeds are equal. For distances below r_s, the sound speed becomes greater than the Alfven speed or equivalently the hydrostatic pressure exceeds the magnetic pressure and the former can no longer be ignored. Figure 3 shows, schematically, the resulting field lines, indicating their translocation from the initial state.

The changes in current density $\underline{j}$ and number density n, resulting from the displacements are then estimated from considerations of mass continuity and magnetic flux conservation. It is found that the number density, in terms of its original value n_0 becomes

$$\frac{n(x, y)}{n_0} = \frac{r^2}{\sqrt{r^4 + 4\delta(x^2 - y^2) + 4\delta^2}} , \qquad (1.37)$$

implying a rarefaction of the plasma in the region $y^2 < x^2 + \delta$, and a compression elsewhere, with its densityrising most sharply near the points $x = 0$, $y = \pm \sqrt{2\delta}$. The current density near the origin has magnitude

$$j = \frac{2\delta}{r_s^2} ,$$

assuming that all the magnetic flux crossing the x-axis and originally lying between $x = 0$ and $x = 2$ is compressed into the region $0 \leq x \leq r_s$.

If no reconnection of the field lines occurs, ($R_m \gg 1$) they will become distorted as indicated in Figure 3.

The foregoing analysis has been criticized by Anzer (1973), especially as regards Syrovatskii's dynamic dissipation mechanism

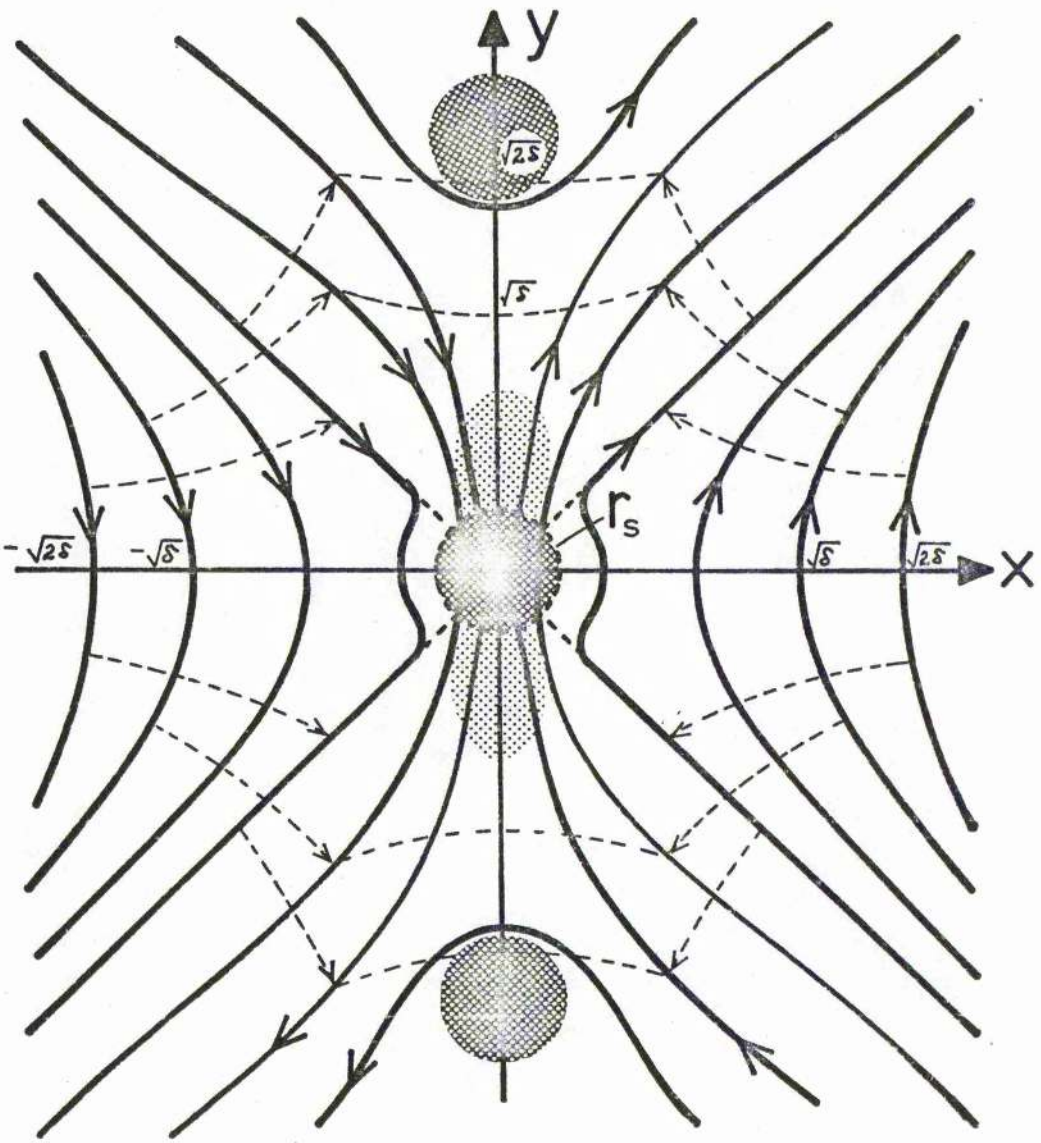

Figure 3.

The magnetic field configuration resulting from a small displacement of the field sources towards each other. When $r \gg r_s$ the field lines move as shown by the dashed lines. Near the origin, the field lines are distorted to form a current sheet. Regions of high plasma compression and rarefaction are shown by heavy and light shading respectively (from Syrovatskii, 1966).

in which the ratio of current to number density j/n determines a condition for the acceleration of charged particles. Nevertheless a treatment of the full time-dependent M.H.D. equations is required to demonstrate the formation of current sheets adequately. No such work has been undertaken analytically, and Syrovatskii's work therefore provides a useful link in current sheet theory.

A different approach to the current sheet problem has been to study the development of a sheet, its actual formation being implicitly assumed. Green (1965) devised an analytic technique for representing a two-dimensional magnetic field in which a current sheet has formed.

Initially the field due to two line currents of strength I_0 and situated on the x-axis at $\pm a_0$, is considered. The resulting magnetic field $\underline{H}_0$ (Figure 4 (a)) will be a potential one (except at the line sources), and can be expressed in terms of the complex variable $z = x + iy$ as

$$H_{0y} + i H_{0x} = \frac{4 I_0 z}{(a_c^2 - z^2)} \quad . \tag{1.39}$$

If the sources now move to new positions $x = \pm a (a < a_0)$, in a perfectly conducting fluid, a current sheet is assumed to form along the y-axis between $y = \pm L$. The resulting field (Figure 4 (b)) will no longer be potential, due to the currents induced by the motions. However, if it is assumed that the currents are confined to the magnetic neutral sheet between $\pm L$, the remaining field will

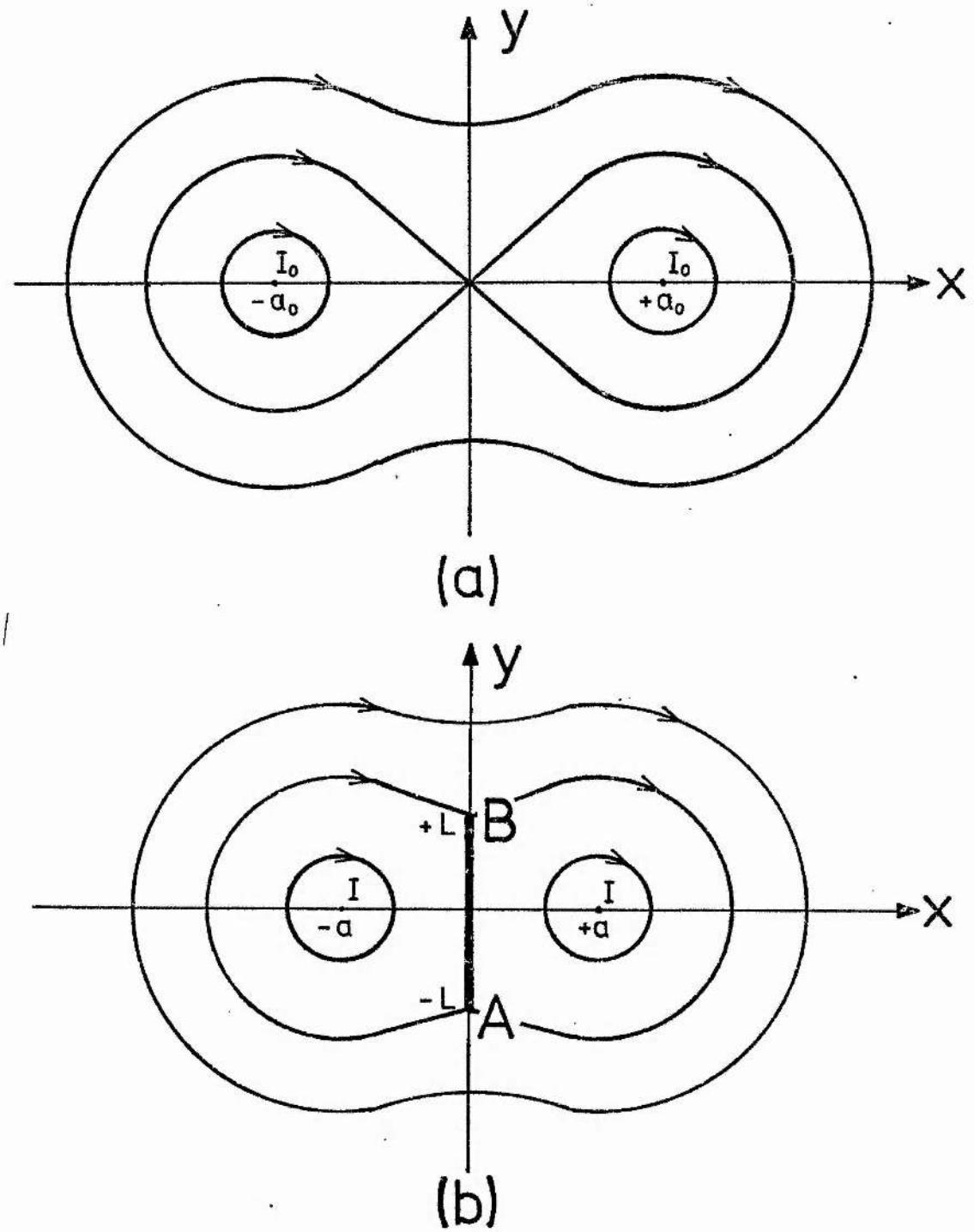

Figure 4.

(a) The magnetic field due to two parallel line sources at $x = a_o$. Outside these sources, the field is current-free and therefore a potential one. An X-type neutral point is formed at the origin. (b) After displacement, a neutral current sheet is formed between A and B.

be current-free and can again be neatly written as an analytic function of z, namely

$$H_y + i H_x = \frac{4aI(L^2 + z^2)^{\frac{1}{2}}}{(a^2 + L^2)^{\frac{1}{2}} (a^2 - z^2)} \quad . \tag{1.40}$$

Here, the currents flowing at $x = \pm a$ are equal to I; in general I will not be equal to I_0 as the displacement will induce currents. The current sheet is represented by a branch cut in the complex plane, giving the required singularity and field reversals as one goes from negative to positive values of x across the sheet.

Green's method was utilized by Priest and Raadu (1975) to investigate the magnetic energy stored when a current sheet is formed in the solar atmosphere by the compression of antiparallel magnetic fields. They consider two bipolar regions whose footpoints approach under the influence of subphotospheric motions (see Figure 5). The magnetic sources are approximated by two line dipoles, of equal moment $(2\pi D_0/\mu)\hat{x}$, situated at $x = \pm a_0$ on the real axis of the complex plane. By using a two-dimensional model, they were able to express the resulting magnetic field in terms of z.

Initially, the field (B_{ox}, B_{oy}) is potential and so may be represented, in the upper-half plane, by the analytic function

$$B_0(z) \equiv B_{0x} - i B_{0y} = \frac{2 D_0 (z^2 + a_0^2)}{(z^2 - a_0^2)^2} \quad . \tag{1.41}$$

If the dipoles now move to new positions $x = \pm a$ ($< a_0$), while the

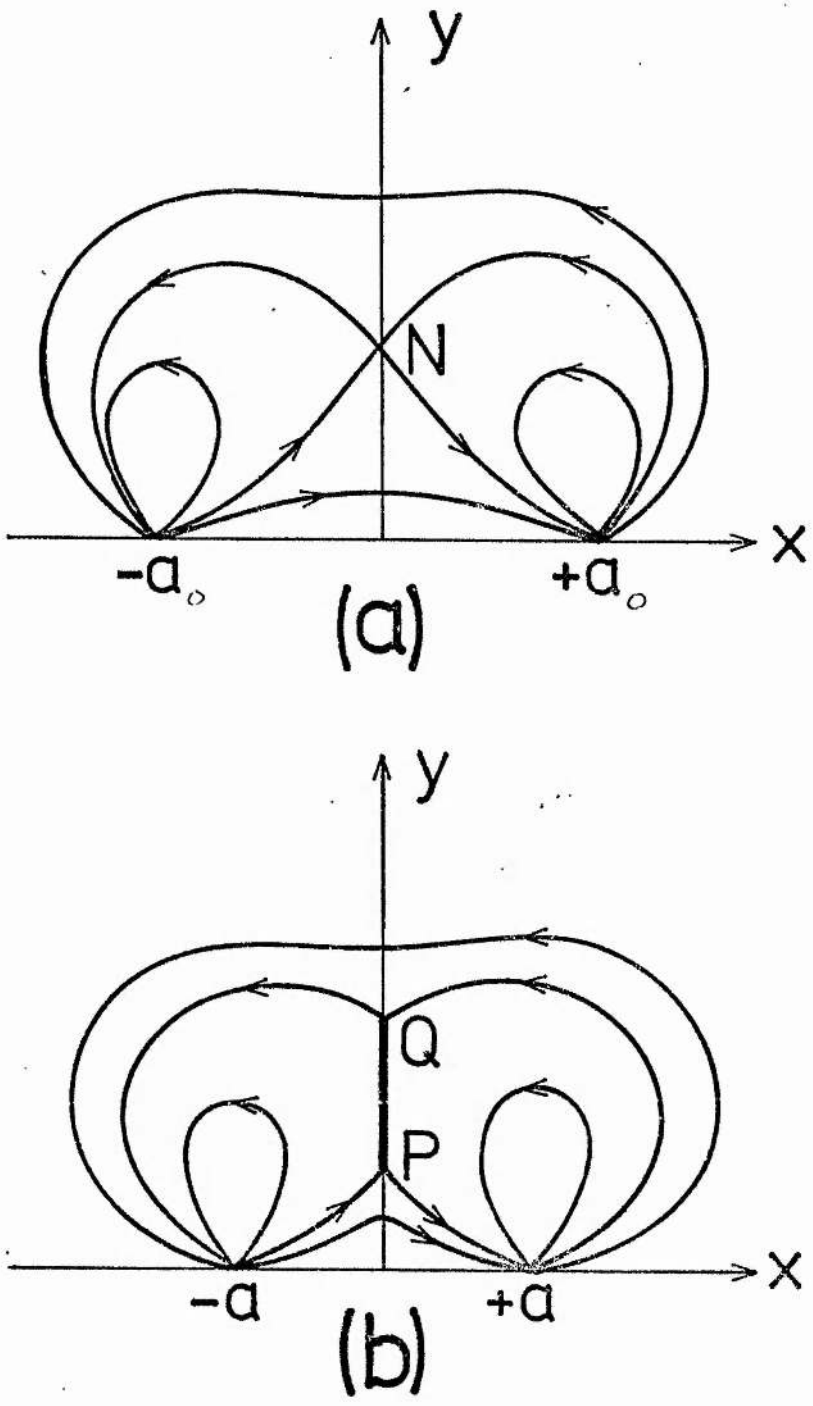

Figure 5.

(a) The potential field in the upper half plane due to two line dipoles at $x=\pm a_0$. A neutral point is situated at N on the vertical axis. (b) After displacing the sources towards each other, a neutral sheet is formed between P and Q along the y-axis.

field remains frozen into the plasma, a current sheet is formed between $y = p$ and $y = q$. The stressed field may be written

$$B(z) = B_x - i B_y = \frac{E(z^2 + p^2)^{\frac{1}{2}}(z^2 + q^2)^{\frac{1}{2}}}{(z^2 - a^2)^2} \quad , \qquad (1.42)$$

where E is a constant, chosen to give the correct behaviour at the sources, and the square roots are defined so as to give the cut. The values of p and q were found from the condition that the flux crossing a given contour remains constant as the field is transformed. Finally the energy due to the presence of the current sheet was determined. Such stored energy is sufficient to account for a large flare when the motions of the footpoints are relatively small.

Although the above models are two-dimensional, they would remain essentially unaltered by the addition of a constant component of magnetic field in a direction perpendicular to the plane being considered. The term "neutral sheet" to describe a region of magnetic field reversal is therefore not strictly correct if such perpendicular components are to be allowed. In this thesis, the term current sheet will be used, although in most cases the two will be synonymous.

Complementing the analytic methods for the investigations of both current sheets and the reconnection process are numerical and experimental techniques. Fukao and Tsuda (1973 (a)) provide convincing evidence for current sheet formation and the reconnection of field lines using a simple finite difference scheme to solve the

steady M.H.D. equations. In a later paper (1973 (b)), they extend their analysis to include time dependence. Experimental evidence has chiefly come from Bratenahl, Baum and co-workers (Baum et al., 1973 (a), (b) ; Bratenahl and Baum, 1976). Their apparatus consists of a double inverse pinch device in which two insulated, current carrying rods (not unlike the line currents in Figure 4 (a)) produce a discharge in a preionized argon atmosphere. Unfortunately the results obtained are of limited applicability when comparisons are made with astrophysical events, mainly due to the low global value of R_m (of order unity in their experiments).

B. Reconnection.

Returning to Dungey's (1953) simple analysis of the collapse of an x-type neutral point, it is obvious that the process cannot proceed indefinitely. As more and more plasma is squeezed into the region along the y-axis, a point must be reached when the plasma density becomes high enough for the diffusion term in the conduction equation (1.14) to be important. The freezing in condition will therefore break down and the magnetic field lines will be able to slip through the plasma and be reconnected at the neutral point.

Sweet (1958 (a) and (b)) proposed a steady mechanism, based on Joule dissipation, for magnetic field reconnection in a current sheet, but it was shown by Parker (1963) that this mode was too slow to account for the rapid energy release of a solar flare. However, direct evidence for Sweet's mechanism in current sheets

present in the solar wind (d-sheets) has been claimed on the basis of data from satellite-borne instruments (Burlaga and Scudder, 1974).

Figure 6 illustrates, schematically, the magnetic field configuration for the reconnection process. In the exterior region, of typical dimension L_e, antiparallel field of strength B_e is carried inwards at a speed of v_e to the inner or diffusion region. The diffusion region, represented by a rectangular region of length L and width ℓ, admits magnetic field with strength B_i and velocity v_i along the sides, and ejects it with strength B_0 and velocity v_0 from the ends.

The order-of-magnitude relationships

$$v_i = \eta/\ell \quad , \tag{1.43}$$

$$v_i L = v_0 \quad . \tag{1.44}$$

and

$$v_0 \simeq v_{Ai} \equiv \frac{B_i}{(\mu\rho)^{\frac{1}{2}}} \tag{1.45}$$

derived by Sweet (1958 (a)) and Parker (1963) for steady incompressible reconnection, determine v_0, ℓ and L given the input parameters B_i and v_i. Much attention has been paid to the so-called "fast" reconnection mode for which L is much less than L_e, to achieve a time scale which is comparable with that observed for flares.

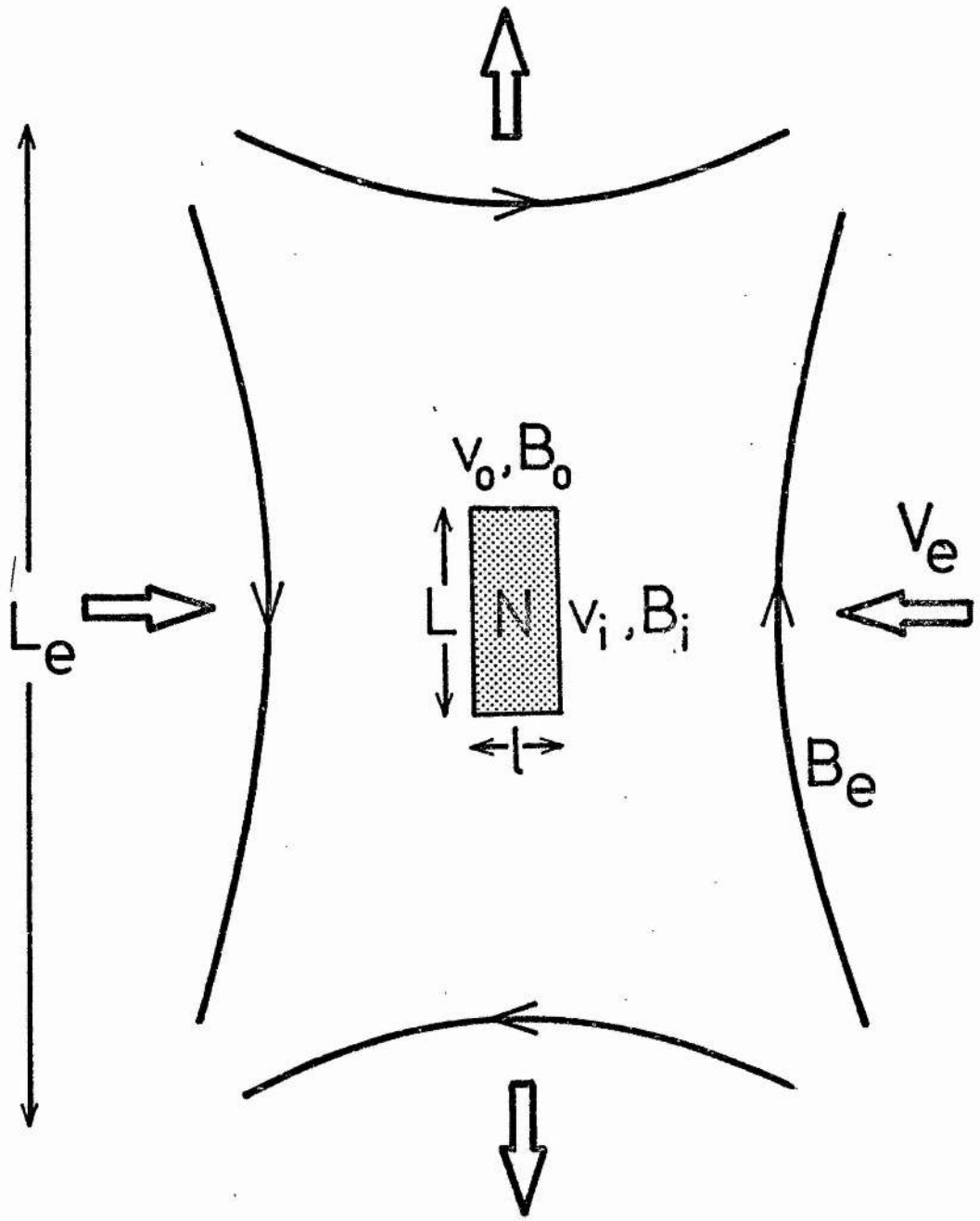

Figure 6.

An overall picture of the magnetic field configuration for the reconnection process. The diffusion region is the shaded rectangle at N; the flow is represented by the large arrows (from Priest, 1976).

The first model for a fast reconnection process was prepared by Petschek (1964). He supposed that the external region contained four stationary slow magnetohydrodynamic shock waves through which the magnetic field direction was rapidly altered (Figure 7 (a)). As the plasma passes through the shocks, magnetic energy is converted into kinetic energy and heat. The reconnection rate, that is, the maximum inflow speed in the external region has been established for Petschek's mechanism by Roberts and Priest (1975). They find that, as the angle made by each shock wave with the y-axis varied, v_e attained a maximum value, dependant upon R_{me} , where

$$R_{me} = \frac{v_A L_e}{\eta} = \frac{B_e L_e}{\eta \sqrt{\mu \rho}} \quad . \tag{1.46}$$

Typically the maximum Alfvén-Mach number

$$M_{e\ max} = \frac{v_{e\ max}}{\left[\frac{B_e}{(\mu \rho)^{\frac{1}{2}}} \right]} \tag{1.47}$$

is of order 0.1 for $R_{me} = 10^2$, decreasing slowly to 0.02 where $R_{me} = 10^6$.

Several objections have been raised against Petschek's mechanism (Green and Sweet, 1966; Priest, 1972) and alternative solutions to the reconnection problem have been proposed by Sonnerup (1970)

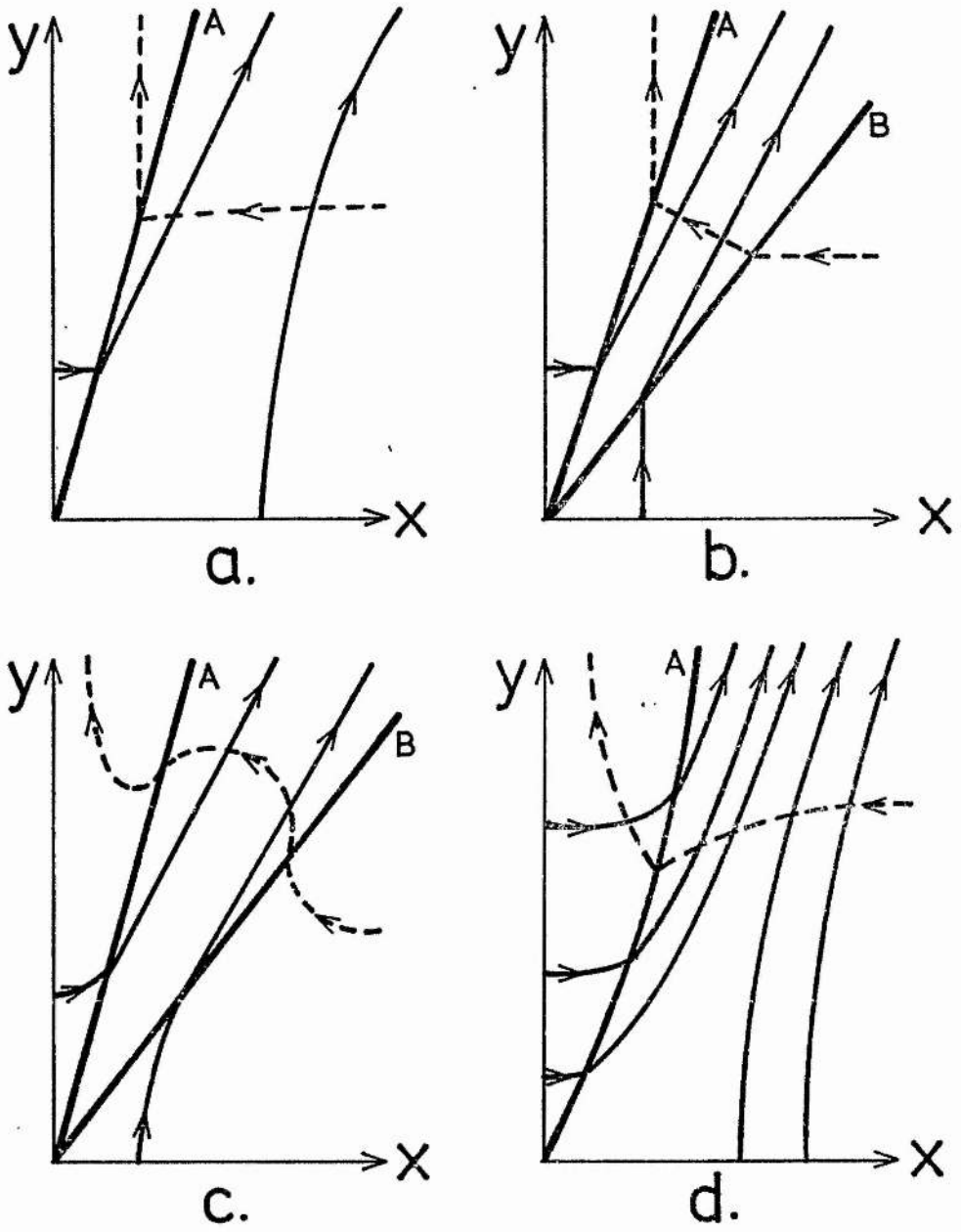

Figure 7.

Schematic representations of one quadrant of the various reconnection models due to (a) Petschek (b) Sonnerup (c) Yeh and Axford and (d) Soward and Priest (from Priest 1976).

→ magnetic field lines ——— shock waves ·-→ stream lines

and Yeh and Axford (1970). Unfortunately, both models contain four extra discontinuities (OB in Figures 7 b and 7 c) which are not physically acceptable, as they have to be generated at corners situated in the external flow region. Furthermore Sonnerup's model may be regarded as a special case of Yeh and Axford's, and Vasyliunas (1975) was able to show that the latter model was mathematically unsound.

Recently Soward and Priest (1976) have solved the reconnection problem with a single discontinuity per quadrant, but relaxing the restriction, imposed by Petschek, that the shock wave should remain straight. Their analysis is more rigorous than Petschek's order-of-magnitude one, and is fairly lengthy. It is summarized by Priest and Soward (1976) in I.A.U. Symposium No. 71. They find that the shocks, magnetic field lines, and velocity streamlines are all curved as indicated in Figure 7 d.

The inflow speed is found to be

$$v_e = \frac{v_i}{(8 R_e M_i / \pi)^{\frac{1}{2}}} , \qquad (1.48)$$

where

$$R_e = \frac{\pi}{8M_i} + \log_e \left[\frac{L_e}{(L M_i)} \right] , \qquad (1.49)$$

and L are defined by equations (1.43) and (1.44) and

$$M_i = \frac{v_i (\mu\rho)^{\frac{1}{2}}}{B_i} \qquad (1.50)$$

is the Alfvén-Mach number at a distance ℓ from the neutral point. Using the condition

$$v_i B_i = v_0 B_0 = v_e B_e \quad , \tag{1.51}$$

due to the constancy of the electric field, equations (1.43), (1.44), (1.45), (1.48), (1.49) and (1.50) are solved for the relationship

$$\frac{\pi}{8M_e} = \frac{\pi}{8M_i} + \frac{1}{2} \log_e (R_{me}^2 M_i M_e) \quad , \tag{1.52}$$

between the Alfvén-Mach numbers M_i and M_e and R_{me}. Differentiation of equation (1.52) with respect to M_i for constant R_{me}, yields a maximum value for M_e, occurring when $M_i = \pi/4$. In Figure 8, the values of $M_{e(max)}$ are plotted against $\log_{10} R_{me}$ to indicate the comparison with Petschek's original values for the maximum reconnection rate. Soward and Priest find a somewhat lower rate, for a given value of R_{me} than did Petschek.

An alternative approach to the problem of determining the maximum reconnection rate was used by Roberts and Priest (1975). They retain Petschek's original configuration with four straight discontinuities, but make allowance for the finite length of the diffusion region and include a non-zero angle between the shock waves and the y-axis (see Figure 9). A detailed analysis of the external region lying upstream of the shocks again reveals a lower maximum reconnection rate compared with Petschek's original estimates. The resulting values of $M_{e(max)}$ are very close to those obtained by

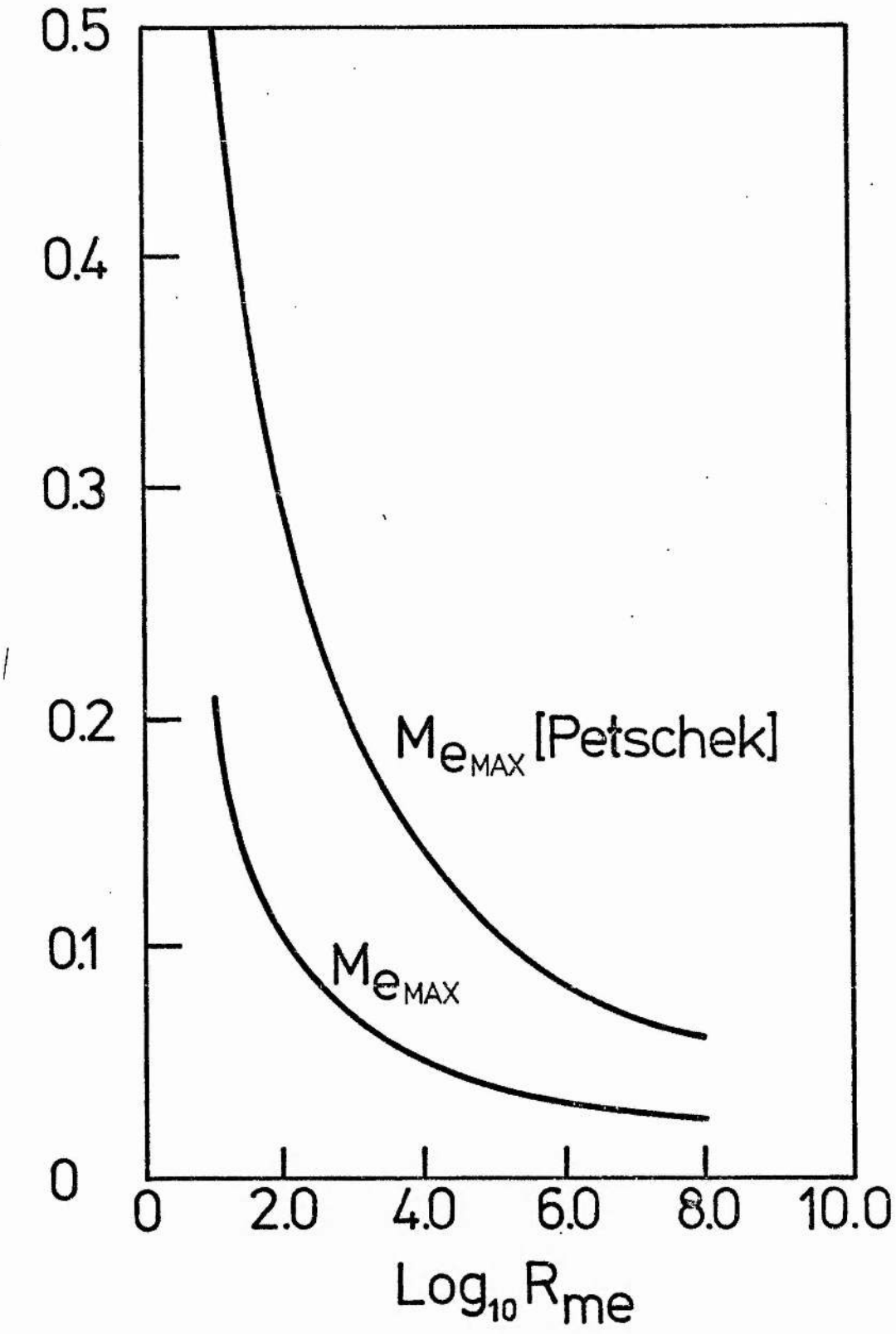

Figure 8.

Values of $M_{e_{max}}$ obtained by Soward and Priest (1976) as a function of R_{me}. The corresponding values obtained by Petschek are also shown (from Priest and Soward, 1976).

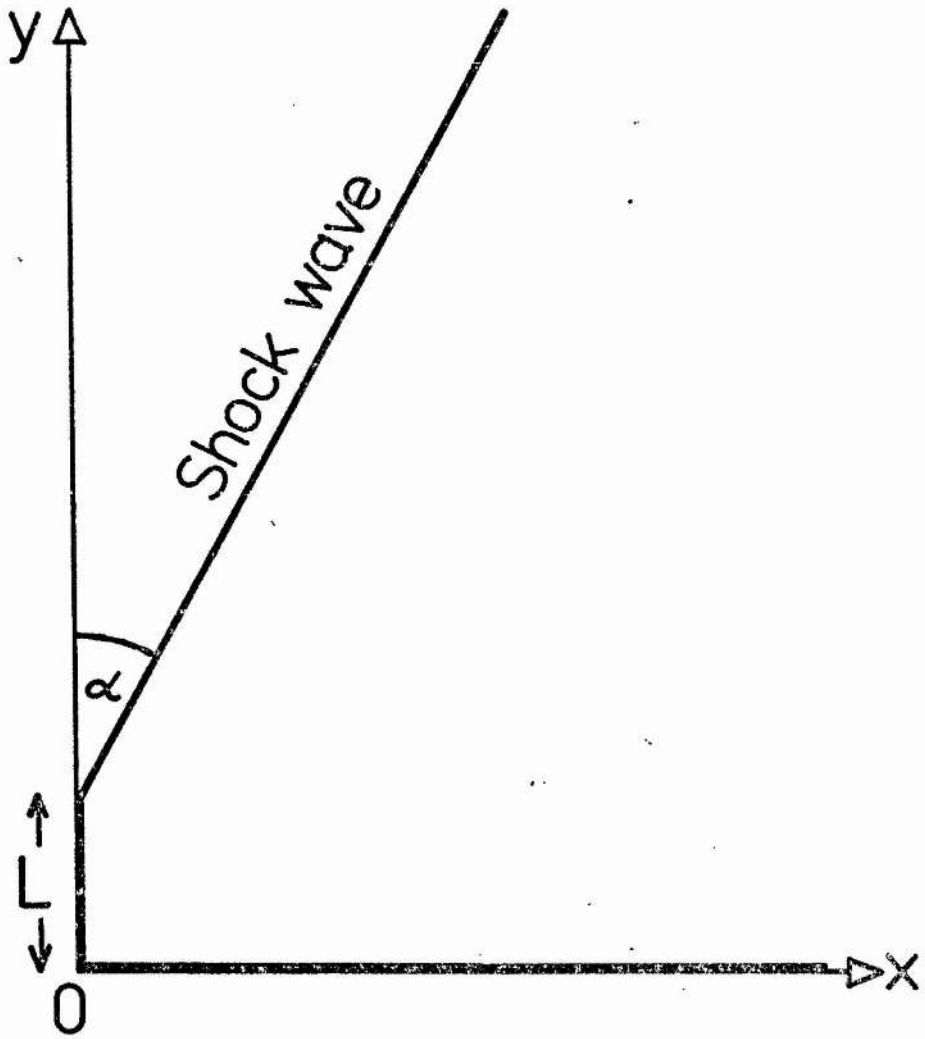

Figure 9.

The geometry of one quadrant of the external region used by Roberts and Priest in solving the boundary-value problem in the upstream region, bounded by the heavy lines in the figure (from Roberts and Priest, 1976).

Soward and Priest (1976), shown in Figure 8.

C. Stability.

Any discussion of magnetohydrodynamic phenomena such as current sheets should include some comment on the stability of a system where equilibrium has been established. A large number of current sheet instabilities have been investigated e.g. (Furth et al., 1963; Chapman and Kendall, 1963; Priest and Heyvaerts, 1975), but attention will be focussed on one particular aspect: namely, a possible instability responsible for the triggering of solar flares.

It was Sweet (1969) who suggested that the preflare state must be in a metastable state. That is, stable for small perturbations, but unable to find a neighbouring stable equilibrium after a sufficiently large perturbation. Furthermore, he asserts that a trigger mechanism due to a thermal instability is as yet the only rigorously established metastable state. Recently Heyvaerts and Priest (1976) have investigated a current sheet instability which may be produced as the sheet evolves from one stable thermal equilibrium to another. They consider the thermal energy balance inside a current sheet, formed above an emerging flux region, the energy conservation equation being

$$E = J + H + K - R \quad , \tag{1.53}$$

in which E represents the convective gain in thermal energy through the sheet, while J, H and K are the joule heating, mechanical heating and conduction terms respectively. R represents the radiative

cooling. Each term in equation (1.53) was approximated and the resulting equation solved for the temperature (T_c) at the centre of the current sheet. Figure 10 shows schematically the type of solution curve to equation (1.53) obtained by Heyvaerts and Priest. Here, T_c is plotted against the height above the photosphere of the sheet. Lower in the solar atmosphere the current sheet follows the lower ("cool") part of the curve passing through a series of equilibria between A and B. However, at a critical height, a further increase necessitates a sudden heating of the interior of the sheet as it seeks a new equilibrium position at D. During this dynamical process, a point (C) is reached where current-driven microinstabilities arise. Particles may be accelerated to high velocities, escaping along field lines. Heyvaerts and Priest suggest that it is at this point that the flare is triggered, giving rise to the short impulsive phase characterised by the production of high energy particles.

The above ideas were further developed and incorporated into the "emerging flux model" for solar flares of Heyvaerts et al., 1976. Syrovatskii (1976) found qualitatively similar results to those of Heyvaerts and Priest, but his analysis neglects all heat sources except joule heating which is balanced by radiation losses.

1.4 AIMS OF THIS THESIS

In this thesis three problems are considered.

Firstly, the development of two-dimensional current sheets is pursued using Green's (1965) analytic technique, the position and

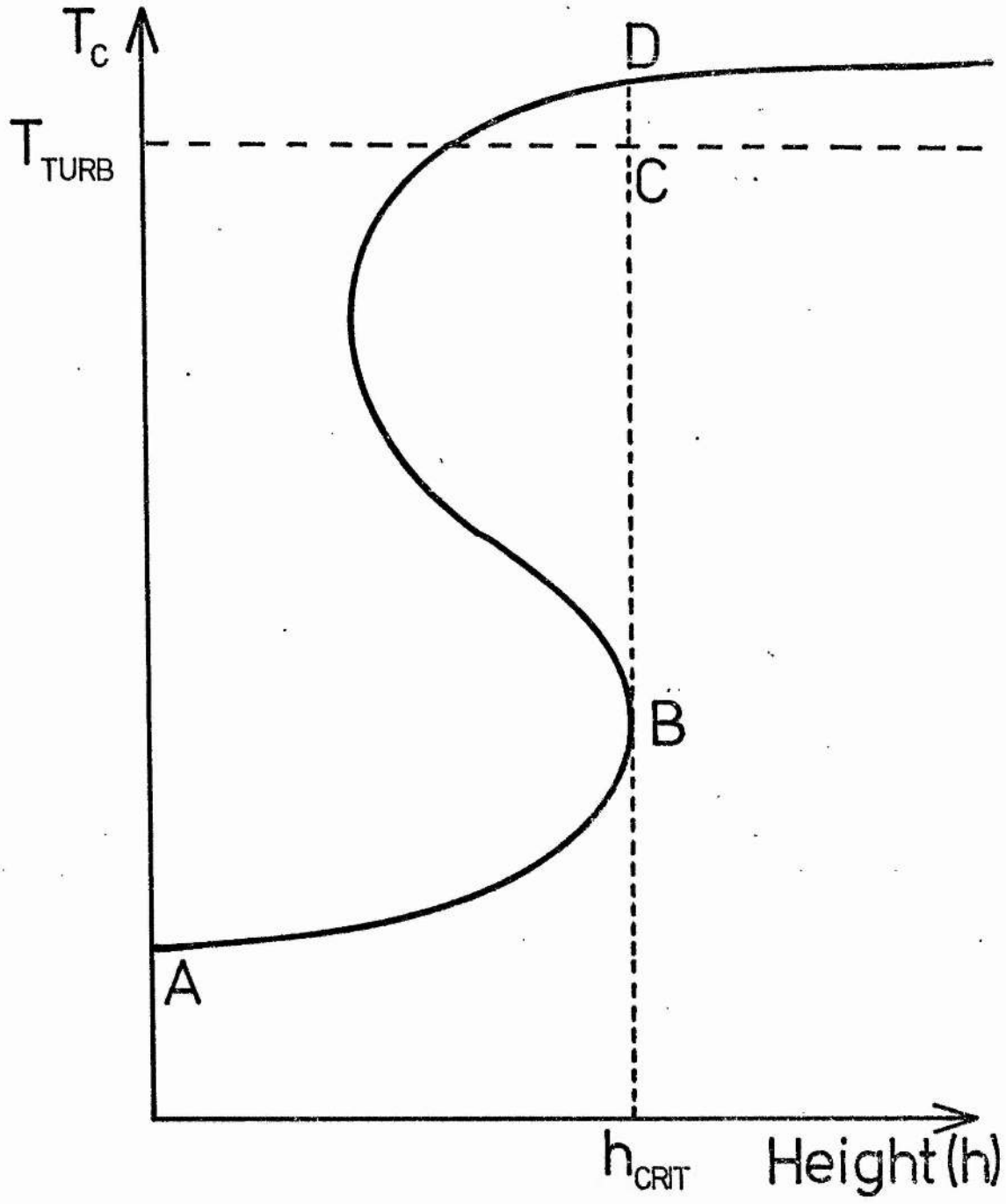

Figure 10.

The temperature T_c in the current sheet as a function of height h in the solar atmosphere. T_{turb} represents the threshold at which the critical current density for turbulence onset is surpassed.

shape of current sheets in more general situations than have previously been considered are deduced. Furthermore the energy stored in excess of potential is determined for two cases of particular relevance to the solar flare problem. Green's method itself is supported by showing that the equation for the magnetic field for converging line sources can be obtained by an alternative method.

In the subsequent chapter, a method is given for obtaining the current distribution in, and position of, a neutral sheet formed in three-dimensional space. By imposing the condition of axial symmetry the equations governing the magnetic field are reduced to an integral equation. This is solved numerically.

Finally, the problem of the solar flare trigger mechanism is investigated, extending and reviewing the ideas of Heyvaerts and Priest (1976). The effects of finite current sheet width limitations are taken into account. Also, the equations are modified to include a region, lower in the atmosphere, where steady reconnection does not occur. Some light is shed on the distinction between commonly occurring flare types (the impulsive and non-impulsive events), on the basis of this work.

CHAPTER 2.

TWO-DIMENSIONAL CURRENT SHEET FORMATION AND MAGNETIC ENERGY STORAGE.

In this chapter, two-dimensional current sheets that are formed between line sources are investigated. Firstly, Green's (1965) results for converging line currents are reproduced to illustrate a possible alternative method. Then his work is extended to determine the length of the current sheet so formed. The remaining sections concentrate on the magnetic fields generated by line dipoles, and the problems of determining the lengths, shapes and positions of current sheets formed by them. In addition the energy stored by the sheet bearing magnetic field, in excess of potential, is calculated for some cases.

2.1. CURRENT SHEET FORMATION BETWEEN CONVERGING LINE CURRENTS.

Green's (1965) technique for determining the magnetic field between two converging line sources (reviewed in Section 1.3) is largely one of "solution by inspection". The magnetic field (equation (1.40)) is seen to satisfy the boundary conditions at the sheet, at large distances from the sources, and as one approaches the sources themselves. The expression for $H(z)$ is chosen to be an analytic function and therefore is necessarily a solution to Laplace's equation. Furthermore, since a solution to Laplace's equation has been found, which satisfies all the given boundary conditions, it must be unique. Nevertheless, the method is a powerful one when considering two-dimensional fields and is subsequently used in this

chapter. However, it cannot be extended to include the three-dimensional case. In this section Green's results are reproduced using an alternative approach, which, despite its length, gives a valuable clue to solving the three-dimensional problem in Chapter 3.

Consider two line currents of strength $4\pi I$, (directed into the page), situated at $\eta = \pm a_0$ of the complex plane $\zeta = \xi + i\eta$ The magnetic field $H_{os}(\zeta)$ (in M.K.S. units) due to the source at $\eta = \pm a_0$, is given by

$$H_{os}(\zeta) = \frac{+2I}{\zeta - ia} \quad , \tag{2.1}$$

that is

$$H_{os}(\zeta) \equiv H_{os_\eta} + i H_{os_\xi} = \frac{2I\xi}{\xi^2 + (\eta - a_0)^2} + \frac{2iI(\eta - a_0)}{\xi^2 + (\eta - a_0)^2} \quad , \tag{2.2}$$

splitting into real and imaginary parts.

If the source at $\zeta = ia_0$, and its image below the ξ-axis now converge to the new positions $\zeta = \pm ia$, a current sheet is assumed to form along the ξ-axis between $\xi = \pm L$ (Figure 11). The problem is to determine the field $H(\zeta)$ in the upper-half plane subject to the following boundary conditions:

(i) $H_\xi = 0$ on $\eta = 0$, $|\xi| > L$;

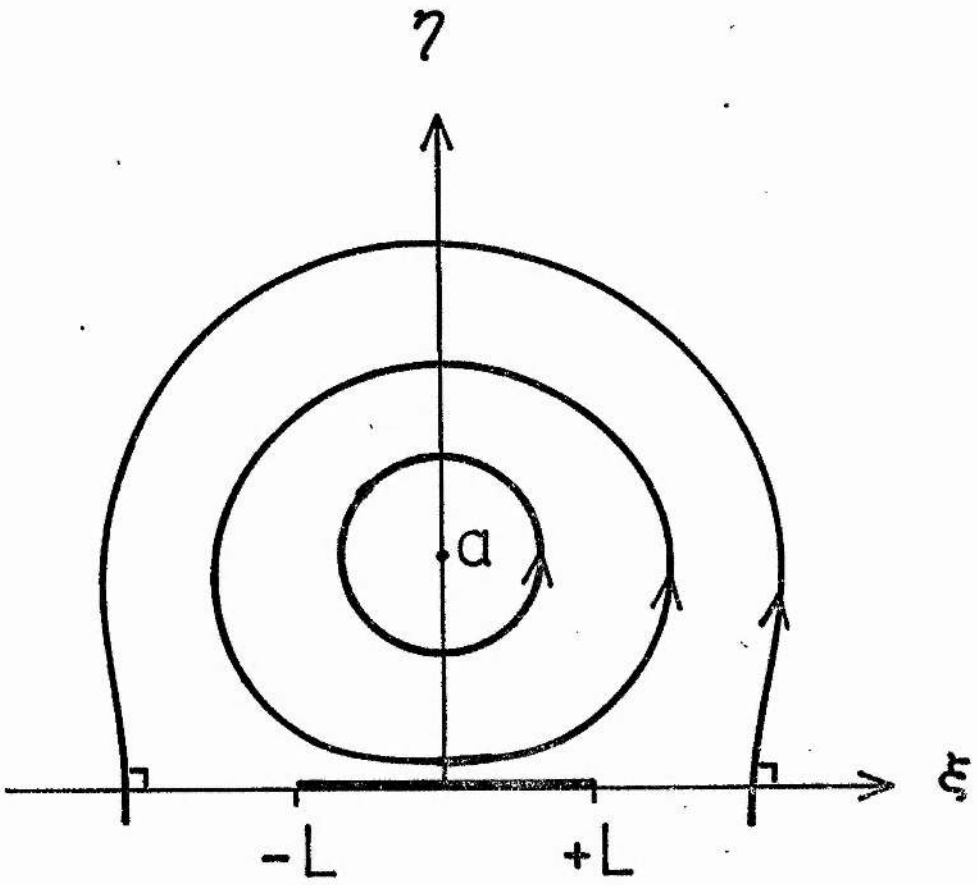

Figure 11.

Schematic representation of the magnetic field lines in the upper half ζ-plane. The field lines are perpendicular to the -axis for $|\xi| > L$ and parallel for $|\xi| < L$.

(ii) $H_\eta = 0$ on $\eta = 0$, $|\xi| < L$;

(iii) $H(\zeta) \simeq \frac{\text{constant}}{\zeta} \longrightarrow 0$ as $|\zeta| \longrightarrow \infty$;

(iv) $H(\zeta) \longrightarrow \frac{-2I}{\zeta - ia}$ as $\zeta \longrightarrow ia$.

The last condition is not a true boundary condition, but a requirement that the field assumes the usual form near the line source.

Since an analytic solution is being sought, the principal of superposition allows the field $H(\zeta)$ to be split into two components,

$$H(\zeta) = H_s(\zeta) + H_c(\zeta), \tag{2.3}$$

where $H_s(\zeta)$ and $H_c(\zeta)$ represent the contributions due to the line sources and the current sheet respectively. $H_s(\zeta)$ is completely known, and is given by equation (2.1) with the zero subscript suppressed. This expedient reduces the task to that of determining the field $H_c(\zeta)$ subject to the new boundary conditions:

(i) $H_{c\xi}(\zeta) \equiv H_\xi - H_{s\xi} = \frac{2Ia}{\xi^2 + a^2}$ on $\eta = 0$, $|\xi| > L$;

(ii) $H_{c\eta}(\zeta) \equiv H_\eta - H_{s\eta} = \frac{2I}{\xi^2 + a^2}$ on $\eta = 0$ $|\xi| < L$;

(iii) $H_c(\zeta) \simeq \frac{\text{constant}}{\zeta} \longrightarrow 0$ as $|\xi| \longrightarrow 0$,

Conditions (i) and (ii) are simply deduced by subtracting the relevant

component of $H_s(\zeta)$ given by equation (2.2) with $\eta = 0$, along the ξ-axis, while the third follows from equation (2.3) and the fact that $H_s(\zeta)$ itself scales as $1/\zeta$ as ζ tends to infinity.

Such two-dimensional, mixed boundary value problems have been discussed at length by Muskelishvili (1946), who reduces the problem to one of solving an integral equation. The solution to the above problem is given as

$$H_c(\zeta) = \frac{1}{\pi i}\frac{\sqrt{\zeta - a}}{\sqrt{\zeta - b}} \int_{-\infty}^{+\infty} \frac{h(t)\sqrt{t-b}}{(t-\zeta)\sqrt{t-a}}\, dt + C\frac{\sqrt{\zeta - a}}{\sqrt{\zeta - b}} \qquad (2.4)$$

(see Muskelishvili (1946) p. 252).

Here $a = -L$, $b = +L$ and $h(t)$ is given by the boundary conditions as

$$h(t) = \begin{cases} \dfrac{2\,I\,t}{(t^2 + a^2)} & |t| < L, \\ \dfrac{2\,iI\,a}{(t^2 + a^2)} & |t| > L; \end{cases} \qquad (2.5)$$

The constant C is determined by condition (iii) as follows. In general the first term in equation (2.4) is unbounded as $\zeta \to b$. Thus, by choosing

$$C = -\frac{1}{\pi i}\int_{-\infty}^{+\infty} \frac{h(t)\, dt}{\sqrt{t-a}\ \sqrt{t-b}}\ , \qquad (2.6)$$

the right hand side of equation (2.4) becomes bounded for all finite ζ .

With these substitutions the field becomes equal to

$$H_c(\zeta) = \frac{\sqrt{\zeta^2 - L^2}}{\pi i} \left[\int_{R_1} \frac{2iIa\,dt}{(t-\zeta)(t^2+a^2)\sqrt{t^2-L^2}} + \int_{R_2} \frac{2it\,dt}{(t-\zeta)(t^2+a^2)\sqrt{t^2-L^2}} \right], \quad (2.7)$$

in which the range of integration has been split into the two domains R_1 and R_2, for which $|t| > L$ and $|t| < L$ respectively. Adding

$$\int_{-L}^{+L} \frac{2Iai\,dt}{(t-\zeta)(t^2-a^2)\sqrt{t^2+L^2}}$$

to the first integral in equation (2.7) and subtracting it from the second one yields

$$H_c(\zeta) = \frac{2I\sqrt{\zeta^2-L^2}}{\pi i} \left[ia \int_{-\infty}^{+\infty} \frac{dt}{(t-\zeta)(t^2+a^2)\sqrt{t^2-L^2}} + \int_{-L}^{+L} \frac{(t-ia)\,dt}{(t-\zeta)(t^2+a^2)\sqrt{t^2-L^2}} \right]. \quad (2.8)$$

The first integral in equation (2.8) may be evaluated by completing the contour in the upper half t-plane and calculating the residues in the usual manner, while the second can be split into standard forms using partial fractions. After some manipulation the net result is,

$$H_c(\zeta)\,\frac{2I\sqrt{\zeta^2-L^2}}{\zeta^2+a^2}\left[\frac{\zeta+ai}{\sqrt{\zeta^2-L^2}}-\frac{2a}{(a^2+L^2)^{1/2}}\right]$$

and so

$$H(\zeta)\equiv H_c(\zeta)+H_s(\zeta)=\frac{-4aI\,(\zeta^2-L^2)^{1/2}}{(a^2+L^2)^{1/2}(a^2+\zeta^2)} \qquad (2.9)$$

Finally a rotation of the axis through 90° effected by the substitution $\zeta = i\,z$, reduces equation (2.9) to Green's original result,

$$H_z = H_y + i\,H_x = \frac{4aI(z^2+L^2)^{\frac{1}{2}}}{(a^2+L^2)^{\frac{1}{2}}(a^2-z^2)} \qquad (2.10)$$

Green did not pursue his analysis much beyond this point. He indicated that L and I could be determined by conditions of flux conservation as the sources converged. However, of greatest interest from the point of view of the flare problem would be to determine the length of the sheet (L). For simplicity, I will be kept constant, although this restriction may lead to erroneous results, especially for large displacements. A further assumption must be

imposed, namely that each line source has finite size. The need for this restriction arises because the magnetic flux crossing any contour radiating from a line source is infinite in this model. Each source is therefore assigned a radius ϵ (assumed constant) that is much smaller than a and L.

The flux F_0 which initially cuts the real axis between the origin and $x = a_0 - \epsilon$ (the edge of the line source) is given by

$$F_o = \int_0^{a_o-\epsilon} \left[H_{oy}\right]_{y=o} \, dx \quad , \tag{2.11}$$

which using equation (1.39) becomes

$$F_o = -2 I_o \log_e \left(\frac{2\epsilon}{a_o}\right) \quad , \tag{2.12}$$

to first order in ϵ

If the sources now approach, allowing no reconnection, the flux F between the origin and the source at $x = + a$ will be the same as F_0 and equal to

$$\int_0^{a-\epsilon} \left[H_y\right]_{y=o} \, dx \quad ,$$

giving

$$F = \frac{4 I_o a}{(a^2+L^2)^{1/2}} \int_0^{a-\epsilon} \frac{(L^2+x^2)^{1/2}}{a^2-x^2} \, dx \quad , \tag{2.13}$$

using equation (2.10). To lowest order in ϵ this becomes

$$F = \frac{-4I_0 \operatorname{cosech}^{-1}\left(\frac{L}{a}\right)}{\left[1+(4a)^2\right]^{1/2}} - 4I_0 \log_e\left[\frac{\epsilon L/a}{\left(1+(4/a)^2\right)^{1/2}(2a\epsilon)^{1/2}}\right] \quad (2.14)$$

Equating F and F_0, the flux conservation condition reduces to

$$2\left\{\frac{\operatorname{cosech}^{-1}(4/a)}{(1+(4/a)^2)^{1/2}} + \log_e\left[\frac{4/a}{2(1+(4/a)^2)^{1/2}}\right]\right\} = \log_e\left(\frac{a}{a_0}\right). \quad (2.15)$$

Inspection of the above equation reveals a singularity as $a/a_0 \longrightarrow \frac{1}{4}$. At this point L becomes infinite indicating that the assumptions made about the constancy of I and ϵ do not allow the result to be taken to such a low value of a/a_0. The graph of L/a_0 against a/a_0 (Figure 12) shows the increase in length of the current sheet down to $a/a_0 = \frac{1}{4}$. An improved analysis, in which I and ϵ were allowed to vary, would be needed to produce a more useful result for the length (L).

The foregoing analysis could be revised for the situation in which the line currents diverge to form a sheet along the x-axis. The magnetic field produced could again be represented by a simple analytic function of z, and the constancy of the flux between the end of the sheet and the source be used to determine L.

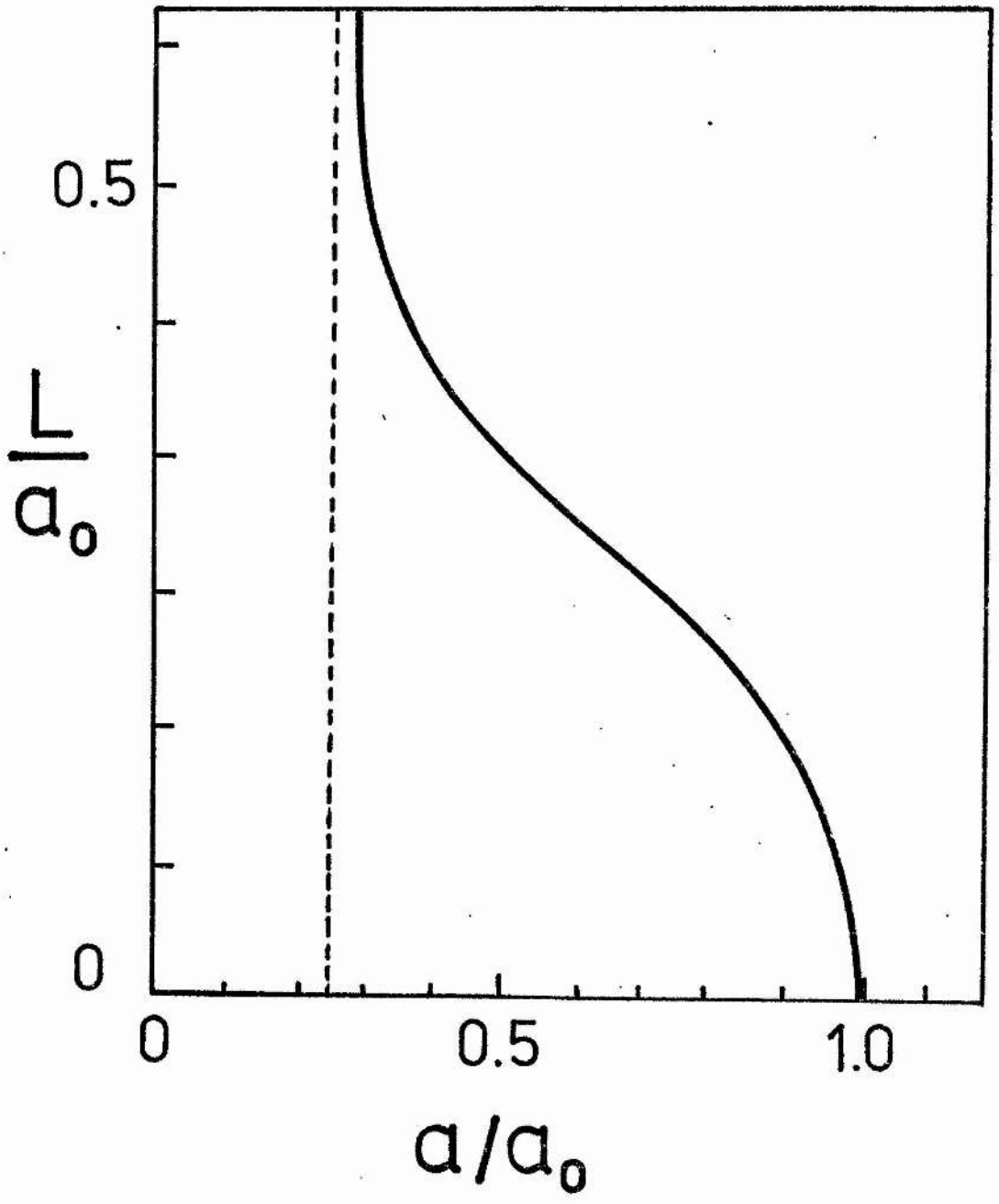

Figure 12.

The length L of the current sheet formed between two line sources as the distance a between them decreases.

2.2. THE FORMATION OF CURRENT SHEETS BETWEEN DIPOLES OF UNEQUAL STRENGTH.

The example chosen by Priest and Raadu (1975) to illustrate the formation of a current sheet was symmetric about the x-axis (Figure 4) and hence only a straight sheet was studied. In Sections (2. 2) and (2. 3), the restrictions of symmetry are relaxed so that the resulting current sheets will be curved, as one may expect in more realistic circumstances. For instance, the formation of a current sheet between an established active region and an emerging pair of satellite sunspots near its edge may be modelled by two line dipoles, the moment of the smaller one increasing in strength. Such a model is presented in this section. Contrastingly section (2.4) deals with the sheet formation when new flux (approximated by a line dipole of increasing moment), presses up against a pre-existing, uniform magnetic field. This situation may occur in fibril crossings, where flares are sometimes located (Zirin and Taraka, 1973) and may be relevant to X-ray bright point flares.

The approximation of bipolar magnetic fields by simple line dipoles is not too inaccurate for two regions whose dimensions are much smaller than their separation. Thus, the coronal bipolar magnetic fields bridging two or more active regions, recently observed from Skylab (Sheeley et al., 1976) may be modelled in this way. The approximations may also provide some useful information for smaller scale lengths and it is used in the following sections for simplicity.

Consider the magnetic field due to two line dipole sources of moment $(2\pi D_A/\mu)\hat{\underline{x}}$ at $x = +a$ in the complex z-plane, and $(2\pi D/\mu)\hat{\underline{x}}$ at $x = -a$ (Figure 13a). Assume that, at some initial

time, $D = D_0$ and the field is potential, that is, in its minimum energy state. It may then be represented by the following analytic function of the complex variable $z = x + iy$,

$$B_0(z) \equiv B_{0x} - iB_{0y} = \frac{D_0}{(z+a)^2} + \frac{D_A}{(z-a)^2} \qquad (2.16)$$

The X-type neutral point present in this initial configuration is located at

$$z_N \equiv x_N + iy_N = -a_0\left(\frac{D_A - D_0}{D_A + D_0}\right) + \frac{2ia_0(D_0 D_A)^{1/2}}{D_0 + D_A} \qquad (2.17)$$

which is clearly at a distance a_0 from the origin.

If the moment of the smaller dipole increases, keeping its position fixed, a current sheet is assumed to form as the field lines of opposite polarity on either side of the neutral point are pressed together. The new field is shown diagrammatically in Figure 13b. A similar effect would occur if the moments remained constant, while the distance between the sources decreased, a possibility which is discussed at the end of the section.

The new magnetic field is assumed to be current-free everywhere outside the current sheet and dipoles. It may therefore be represented by an analytic function of z that behaves like

$$\frac{\text{constant}}{(z \pm a)}$$

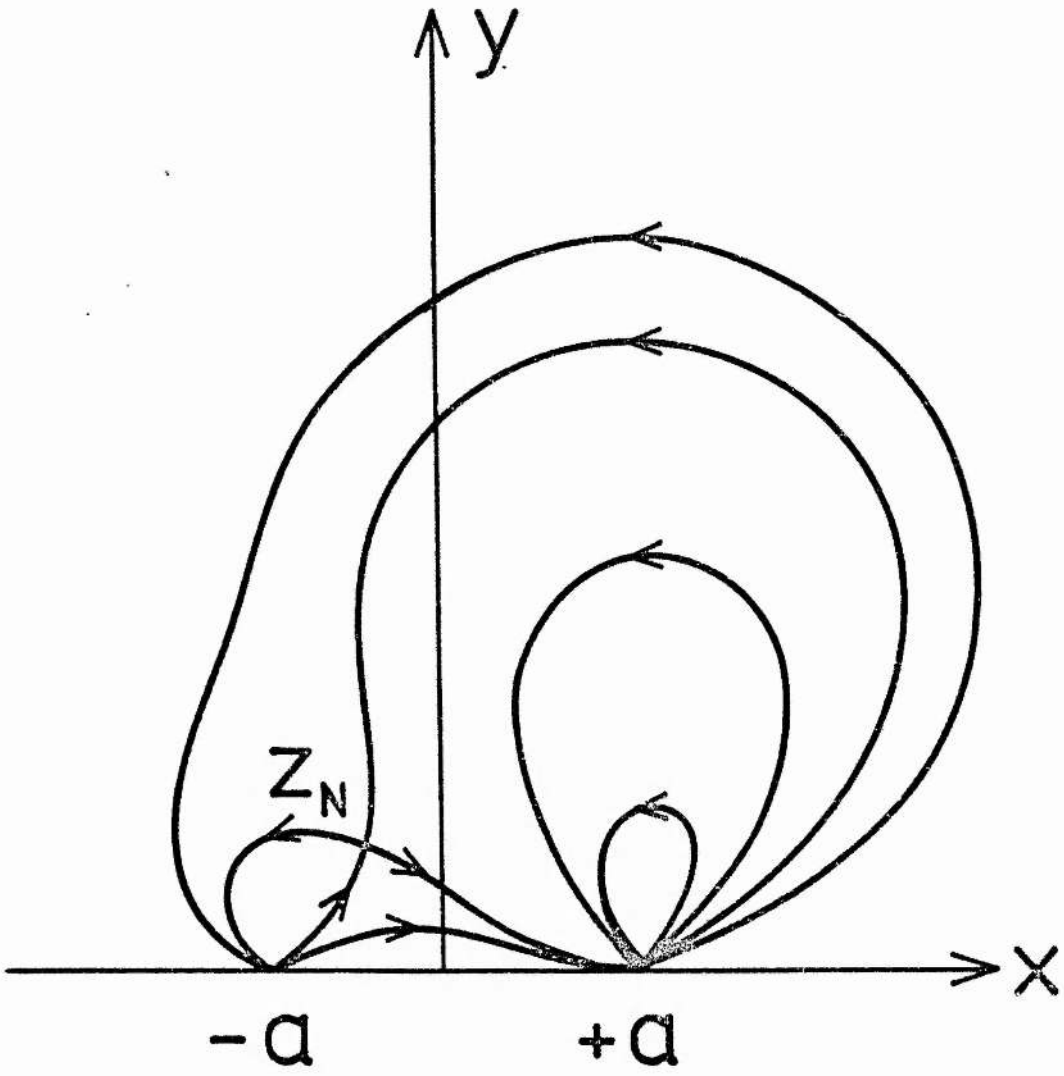

Figure 13a.

Schematic representation of the magnetic field configuration in the plane perpendicular to two line dipoles at x=±a, for the purely potential situation, with a neutral point at Z_N.

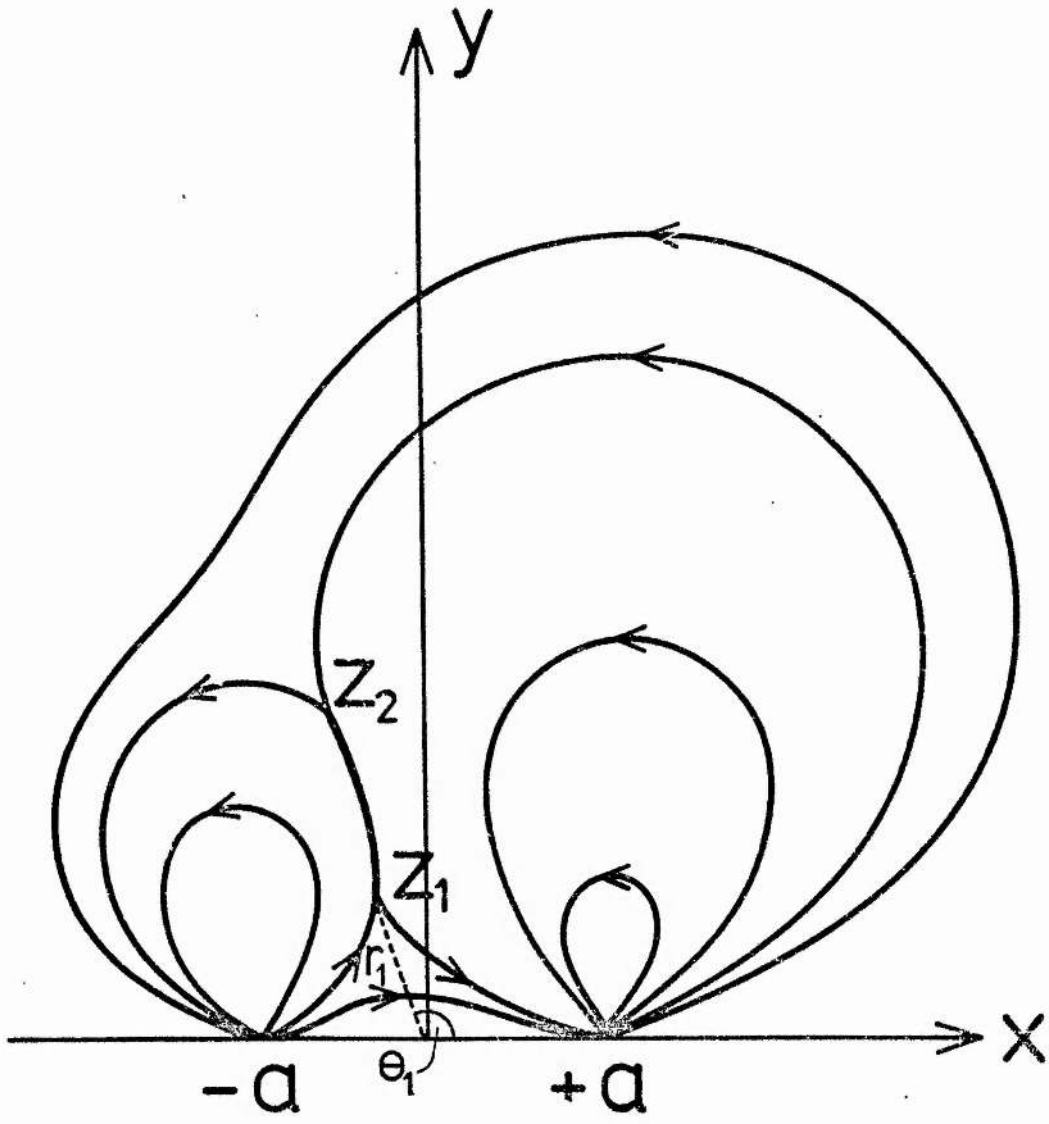

Figure 13b.

Schematic representation of the magnetic field configuration in the plane perpendicular to two line dipoles at x=±a, after an increase in moment of the smaller dipole resulting in the formation of a current sheet between $Z_1 = r_1 \exp(i\theta_1)$ and $Z_2 = r_2 \exp(i\theta_2)$.

near $z = \pm a$ and the satisfying following boundary conditions:

(i) as $|z| \to \infty$, $|\underline{B}| \simeq \frac{\text{constant}}{|z|^2} \to 0$

(ii) $B_y = 0$ on the real axis $(z \neq \pm a)$.

The sheet and its image below the axis are represented by branch cuts from z_1 to z_2, and z_1^* to z_2^*, respectively (a star denoting the complex conjugate). The field possessing these properties is

$$B(z) \equiv B_x - iB_y = \frac{E\left[(z - z_1)(z - z_2)(z - z_1^*)(z - z_2^*)\right]^{1/2}}{(z^2 - a^2)^2} \qquad (2.18)$$

where E is a constant to be determined, and the square roots are defined so as to give the cuts. In the particular case where the dipole moments are equal, $z_1^* = -z_1$, $z_2^* = -z_2$ and so the original result of Priest and Raadu (1975), with $z_1 = ip$ and $z_2 = iq$, is recovered.

The current sheet, and hence the branch cut representing it, will now be curved owing to the departure from symmetry. However, its shape does not affect the form of equation (2.18), as a branch cut may follow any simply connected path between its end points. The precise form adopted by the sheet will be deduced from considerations of flux conservation.

The five unknown quantities $z_1 = x_1 + iy_1$, $z_2 = x_2 + iy_2$ and E can be determined from the behaviour of the field near $z_1 = \pm a$

and the frozen-in flux conditions.

Firstly, as z^2 approaches a^2, the expression for $B(z)$ in equation (2.18) must reduce to that of dipole fields with moments $D(>D_0)$ at $z = -a$, and D_A at $z = +a$. From these conditions,

$$E = \frac{4\,D a^2}{\left[(a-z_1)(a-z_2)(a-z_1^*)(a-z_2^*)\right]^{\frac{1}{2}}} \quad , (z \longrightarrow +a)$$

$$E = \frac{4\,D a^2}{\left[(a+z_1)(a+z_2)(a+z_1^*)(a+z_2^*)\right]^{\frac{1}{2}}} \quad , (z \longrightarrow -a). \qquad (2.19)$$

Next, the magnetic flux crossing a contour that stretches from the neutral point (z_N) to the real axis in Figure 13a must be the same as that crossing its counterpart from z, in the final configuration, Figure 13b. Equating these fluxes, one obtains

$$\int_0^{y_N} \left[B_{ox}\right]_{x=x_N} dy = \int_0^{y_1} \left[B_x\right]_{x=x_1} dy \quad ,$$

or, having substituted for B_{ox} from equation (2.16)

$$\frac{(D_0\,D_A)^{\frac{1}{2}}}{a} = \int_0^{y_1} \left[B\,x\right]\, x = x_1 \; dy \quad , \qquad (2.20)$$

where the integral on the right hand side has to be evaluated numerically.

Finally, the flux crossing the positive imaginary axis in the two figures can be equated. For the initial configuration this

is just

$$\int_0^{\infty} \left[B_{ox} \right]_{x=0} \, dy ,$$

which, on substitution for B_{ox}, is identically zero, a result one might have deduced from physical considerations as follows. The number of lines of force crossing the positive y-axis from left to right in Figure 13 a must be the same as that crossing in the opposite direction. This follows directly from the fact that equal numbers of lines of force must leave and enter each dipole source. Since, in an intuitive manner, the magnetic flux is proportional to the number of field lines crossing a chosen contour, then clearly the net flux threading the y-axis must be zero.

The flux crossing the positive y-axis in the final configuration is given by

$$\int_0^{\infty} \left[B_x \right]_{x=0} dy = \frac{1}{2} \oint_m \int_{y=-\infty}^{+\infty} \left[B(z)^* \right] dz \quad . \tag{2.21}$$

The integral on the right hand side may be evaluated by completing the contour and calculating the enclosed residues. By choosing contours that pass either side of the branch cuts, the two independent conditions

$$\left.\begin{aligned} \frac{1}{2} \oint_m \int_{y=-\infty}^{+\infty} \left[B(z)^* \right]_L dz &= 0 \\ \frac{1}{2} \oint_m \int_{y=-\infty}^{+\infty} \left[B(z) \right]_R dz &= 0 \end{aligned}\right\} \tag{2.22}$$

are obtained, where L and R denote contours to the left and right of the cuts respectively. Calculating the residue at $z = -a$, the first condition yields

$$\frac{1}{a-z_1} + \frac{1}{a-z_2} + \frac{1}{a-z_1^*} + \frac{1}{a-z_2^*} = \frac{2}{a} \quad , \tag{2.23}$$

while, from the second condition, using the residue at $z = +a$ gives

$$\frac{1}{a+z_1} + \frac{1}{a+z_2} + \frac{1}{a+z_1^*} + \frac{1}{a+z_2^*} = \frac{2}{a} \tag{2.24}$$

Equations (2.22), (2.23) and (2.24) may be greatly simplified to produce the following set of relations

$$a^2 = r_1 r_2 \quad , \tag{2.25}$$

$$\Theta_1 = \Theta_2 = \cos^{-1}\left[\frac{a^2 + r_1^2}{2ar_1}\,\frac{D - D_A}{D + D_A}\right] \quad , \tag{2.26}$$

$$E = \frac{2a\, r_1 (D + D_A)}{(r_1^2 + a^2)} \quad , \tag{2.27}$$

where $r_1 \exp(i\,\Theta_1)$ and $r_2 \exp(i\,\Theta_2)$ are the polar representations of z_1 and z_2, respectively. Equations (2.25) and (2.26) have a simple geometric interpretation. The latter implies that the end points of the current sheet are constrained to lie on a straight line through the origin, while from equation (2.25), they are seen to be

inverse points with respect to a circle of radius a, centred at the origin. These results suggest that the magnetic field for the asymmetric situation being studied here may be derived by a simple mapping of the symmetrical field investigated by Priest and Raadu. However, no transformation was found that could map one field onto the other.

As well as the end-points, the shape of the current sheet may be determined, since the flux (F) crossing an ordinate between the real axis and a point (x_s, y_s) lying on the sheet, namely

$$F = \int_0^{y_s} \left[B_x \right]_{x = x_s} dy \quad , \tag{2.28}$$

must remain constant for x_s between x_1 and x_2. Equation (2.28) thus determines y_s as a function of x_s and can be evaluated numerically. As D increases in value, the shape and position of the current sheet change. In Figure 14, a particular case is shown where the locus of the end points of the sheet is plotted (dashed curve). The ratio of the dipole moments (D/D_A) is assumed to be initially 0.01, increasing finally to $D/D_A = 1.0$. Several plots of the shape of the sheet are superimposed.

The current sheet is curved away from the smaller dipole. The magnetic pressure and tension must balance everywhere outside the sources. In particular, since the magnetic field increases more rapidly on the lower side of the sheet than above, the

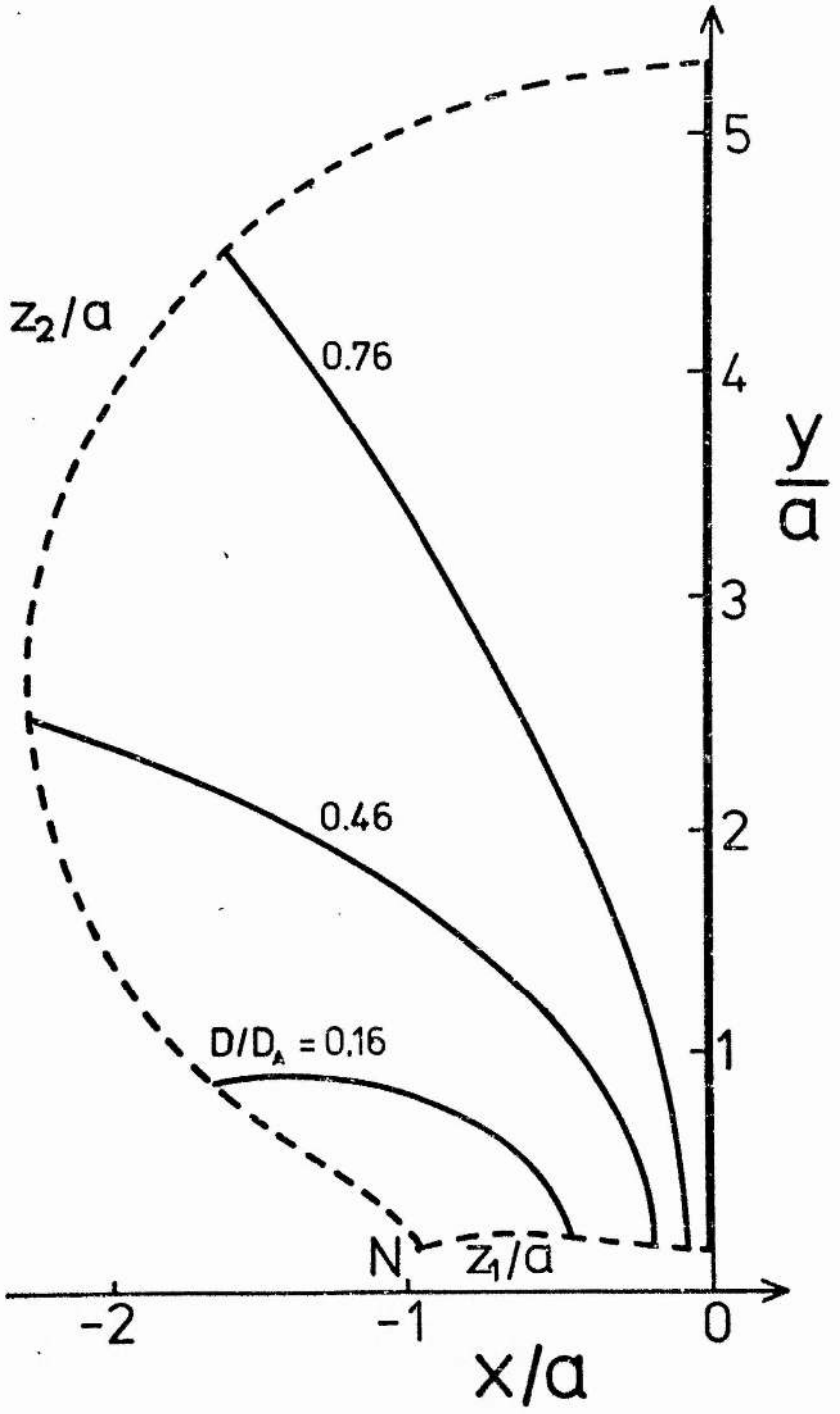

Figure 14.

The locus (dashed) of the end points of a current sheet as the moment of a dipole at x=-a increases from $0.01D_A$ to D_A, where D_A is the moment of a constant dipole at x=a. Several examples of the sheet, showing its shape are superimposed.

corresponding pressure difference must be balanced by the tension along the field lines which results from the curvature shown. As D approaches D_A the curvature decreases until, in the limit, the symmetrical situation investigated by Priest and Raadu (1975) is reached.

A current sheet may also be formed if the dipoles were to move towards each other while their moments remained constant. The analysis would be almost identical to the above with D_0 and D_A constant, but the dipole sources moving from some initial position $z = \pm a_0$ say, to $z = \pm a$ $(a < a_0)$. Equations (2.25) to (2.27) would hold (with $D \equiv D_0$), the end points of the sheet still being constrained to lie on a radius vector from the origin. In equation (2.20), the left hand side is just

$$\frac{(D_0 D_A)^{\frac{1}{2}}}{a_0} ,$$

and the computation of z_1 and z_2 may be carried out as before. Again, the shape of the current sheet may be found from equation (2.28).

In Figure 15 a few examples of the locus of the end points of the current sheet are plotted against the decreasing dipole separation (a/a_0).

Figure 16 shows the variation in the angle of inclination (θ_1) as a/a_0 decreases. As the ratio of the dipole moments (D_0/D_A) approaches unity, the current sheet becomes straighter and closer to the vertical axis, until in the limit $\frac{D_0}{D_A} = 1$, the symmetrical case with a straight sheet is obtained.

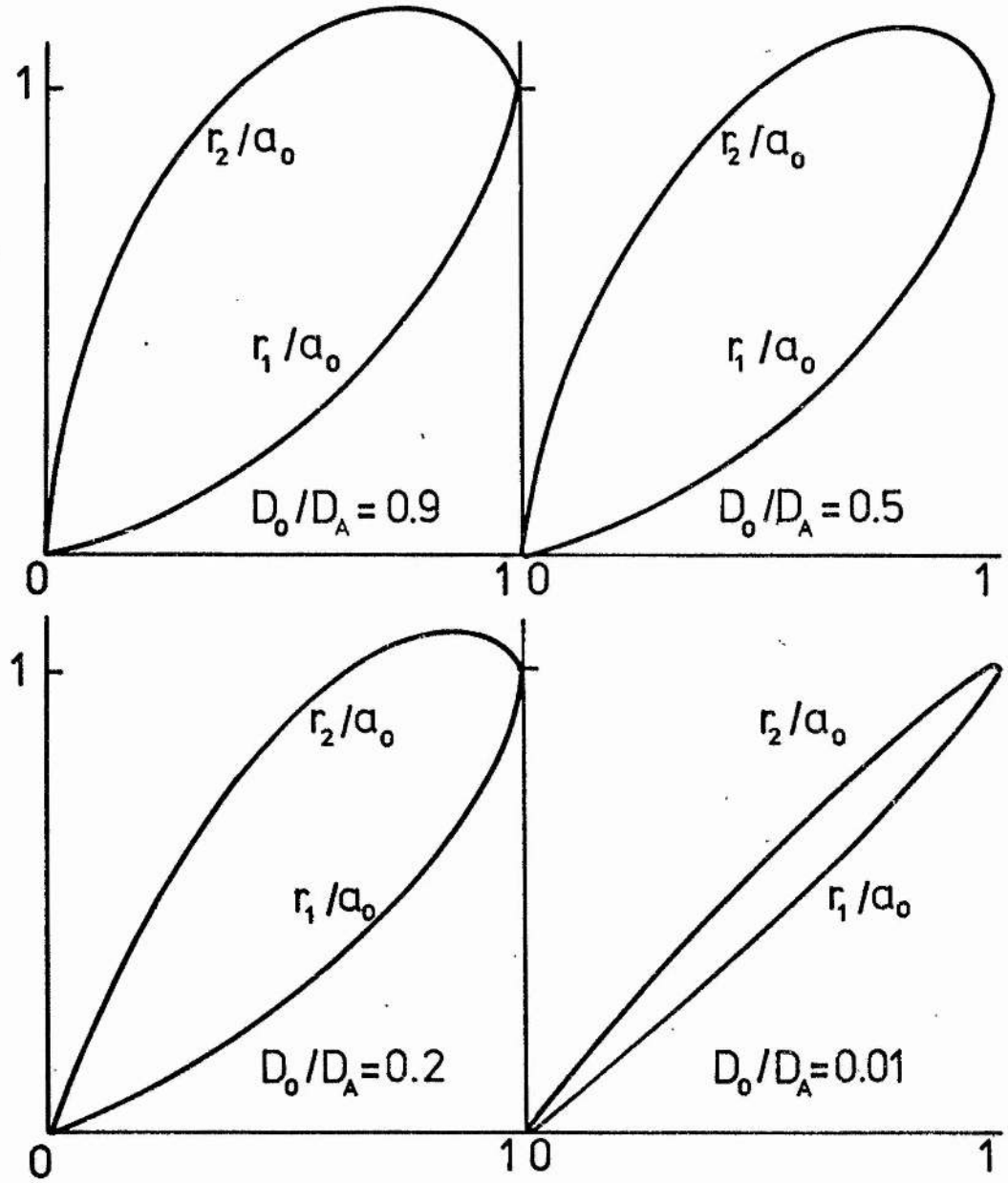

Figure 15.

The loci of the end points (r_1/a_0 and r_2/a_0) of the current sheet for D_0/D_A = 0.9, 0.5, 0.2 and 0.01, as the dipole separation a/a_0 decreases.

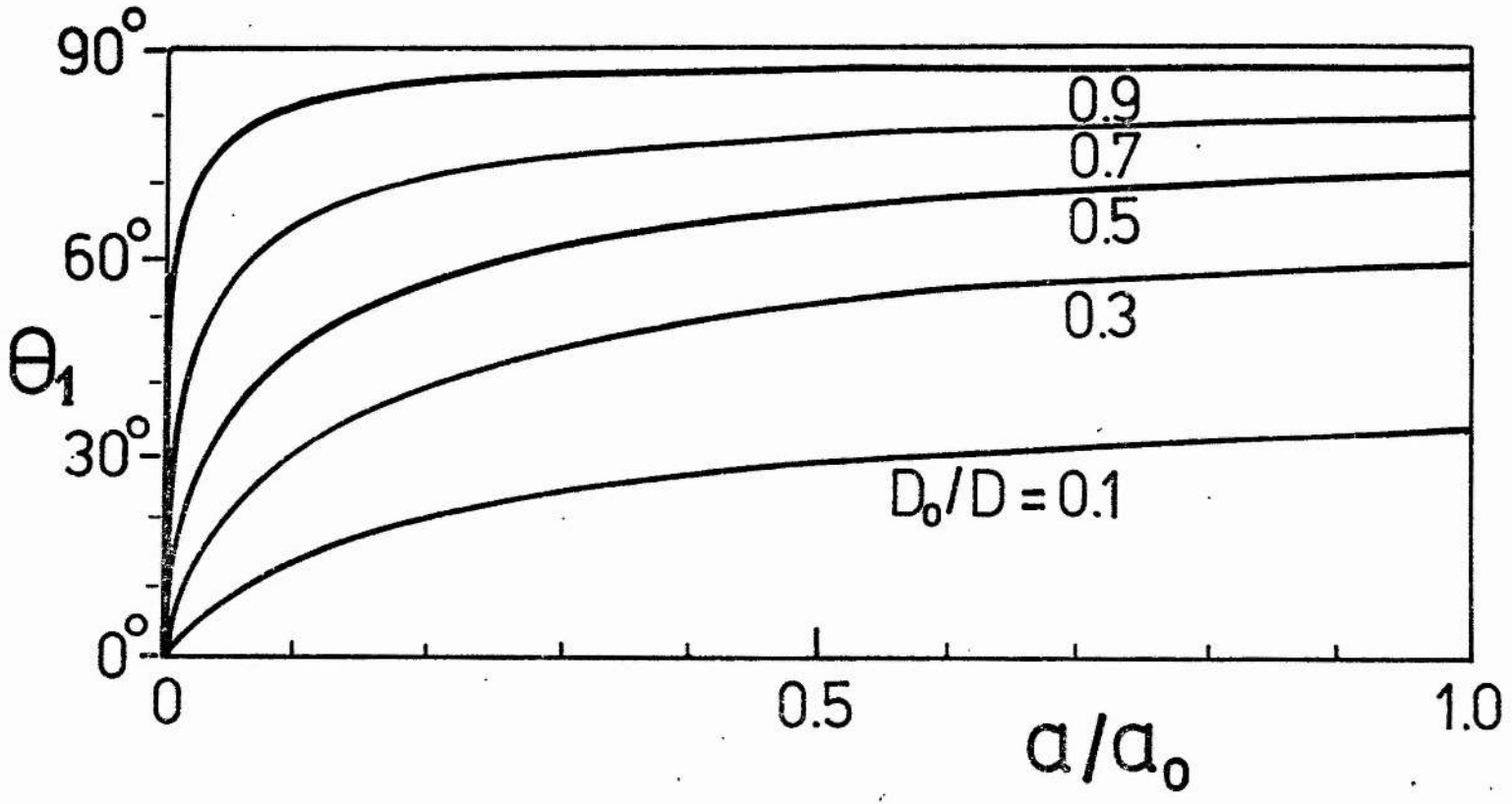

Figure 16.

The angle of inclination ($\theta_1=\theta_2$) of the current sheet (referred to the negative x-axis) as the dipole separation increases.

2.3. THE ENERGY ASSOCIATED WITH THE MAGNETIC FIELD.

Having obtained E_1, z_1 and z_2, the energy associated with the magnetic field may be determined. In particular, the energy stored in excess of potential due to the presence of the current sheet may be evaluated.

The magnetic energy is normally given by the integral

$$W = \frac{1}{2\mu} \iint B B^* \, dx dy .$$

evaluated over the entire (x,y)-plane. Alternatively, following Priest and Raadu (1975), a numerical evaluation of the double integral may be avoided by considering the self and mutual energies of the sources of the field.

The energy W associated with a particular field that arises from n sources may be expressed as

$$W = \sum_{l=1}^{n} W_l + \sum_{\substack{l=1 \\ m>l}}^{n} W_{lm} , \qquad (2.29)$$

where W_l is just the self energy of the source l,

$$W_l = \frac{1}{2} \int_l A_l j \, dV \qquad (2.30)$$

and W_m the "mutual" or interaction energy

$$W_{lm} = \int A_m j \, dV = \int_m A_l j \, dV \quad , \tag{2.31}$$

between sources l and m. In equations (2.30) and (2.31) j is the current density and $A_l \hat{\underline{k}}$ the vector potential for the magnetic field due to the source . Alternatively, if one of the sources, m say, is a dipole of moment $(2\pi D / \mu)\hat{\underline{x}}$, then equation (2.31) becomes

$$W_{lm} = -\left(\frac{2\pi D}{\mu}\right)\hat{\underline{x}} \cdot \underline{B}_{lm} \quad , \tag{2.32}$$

where $\underline{B}_{lm}$ is the magnetic induction at the position of the dipole m due to the source (Coulson, 1958, p.40).

The magnetic field given by equation (2.18) arises from four sources: the two dipoles, the current sheet and its image below the axis, denoted by the subscripts 1,2,3 and 4 respectively. Thus, the energy W, for the entire complex plane, may be written

$$W = W_1 + W_2 + W_3 + W_{12} + W_{13} + W_{14} + W_{23} + W_{24} + W_{34} \, , \tag{2.33}$$

which may be compared with that (W_p) of the initial (purely potential) field,

$$W_p = W_1 + W_2 + W_{12} \tag{2.34}$$

The self energies of the dipoles are infinite if one assumes

them to have zero dimensions. However for the applications in mind in this thesis, namely bipolar regions, the sources have some finite size. To simulate this each dipole is assumed to have a constant radius r_0. Then, using equations (2.30) and (2.31) the energy W_P becomes

$$W_P = \frac{\pi}{2\mu}\left[\frac{(D_A^2 + D_o^2)}{2r_o^2} - \frac{D_o D_A}{a^2}\right] \tag{2.35}$$

By contrast, the magnetic energy W_s, in the upper half plane, due to the presence of the current sheet and its image alone, is

$$W_s = \frac{1}{2}\,(W_3 + W_4 + W_{31} + W_{32} + W_{14} + W_{24} + W_{34}), \tag{2.36}$$

which, using conditions of symmetry and equations (2.30) and (2.31) becomes

$$W_S = \frac{1}{2}\int_3 A_s j\,dV + \int_3 (A_1 + A_2)\,j\,dV \quad , \tag{2.37}$$

where A_s is just the potential at the sheet due to all sources. If one assumes that no reconnection has occurred, A_s is the same as the potential at the neutral point N in the initial situation, namely

$$A_S = \int_0^{y_N} \left[B_{ox}\right]_{x=x_N} dy \quad , \tag{2.38}$$

which, having used equation (2.16) becomes $(D_0/D_A)^{\frac{1}{2}}/a$. The first integral, W_{s_1}, say, in equation (2.37) may be written

$$W_{s_1} = \frac{1}{2} \int_{\text{Sheet}} \underline{j} \cdot \underline{A}_s \, dS$$

$$= \frac{1}{2\mu} \int_{\text{Sheet}} \nabla \times \underline{B} \cdot \underline{A}_s \, dS$$

where equations (1.6) and (1.7) have been used. Now, for a thin box about the current sheet, $\underline{A}$ is approximately constant, and so, using Stokes' theorem,

$$W_{s_1} = \frac{A_s}{\mu} \, Re \int_{z_1}^{z_2} \left[B(z) \, dz \right]_R \,, \tag{2.39}$$

where $$B(z) = \frac{E\left[(z-z_1)(z-z_2)(z-z_1^*)(z-z_2^*) \right]^{\frac{1}{2}}}{(z^2-a^2)^2}$$

the integral being evalued along the right hand side of the branch cut. A numerical integration is needed for this. The second integral in equation (2.37) becomes

$$\frac{\pi (D+D_A)^2}{8\mu a^2} \left[\frac{r_1^2 - a^2}{r_1^2 + a^2} \right] \,, \tag{2.40}$$

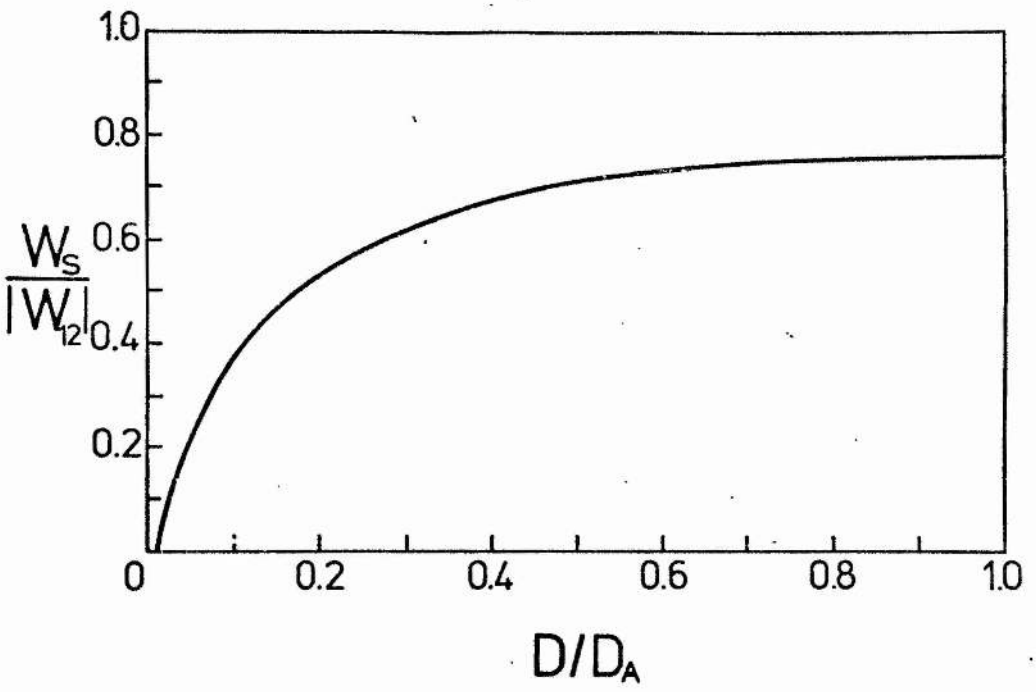

Figure 17.

The stored magnetic energy W_s due to the presence of the current sheet, relative to the mutual energy $|W_{12}|$ of the dipoles, as the moment of the smaller dipole increases.

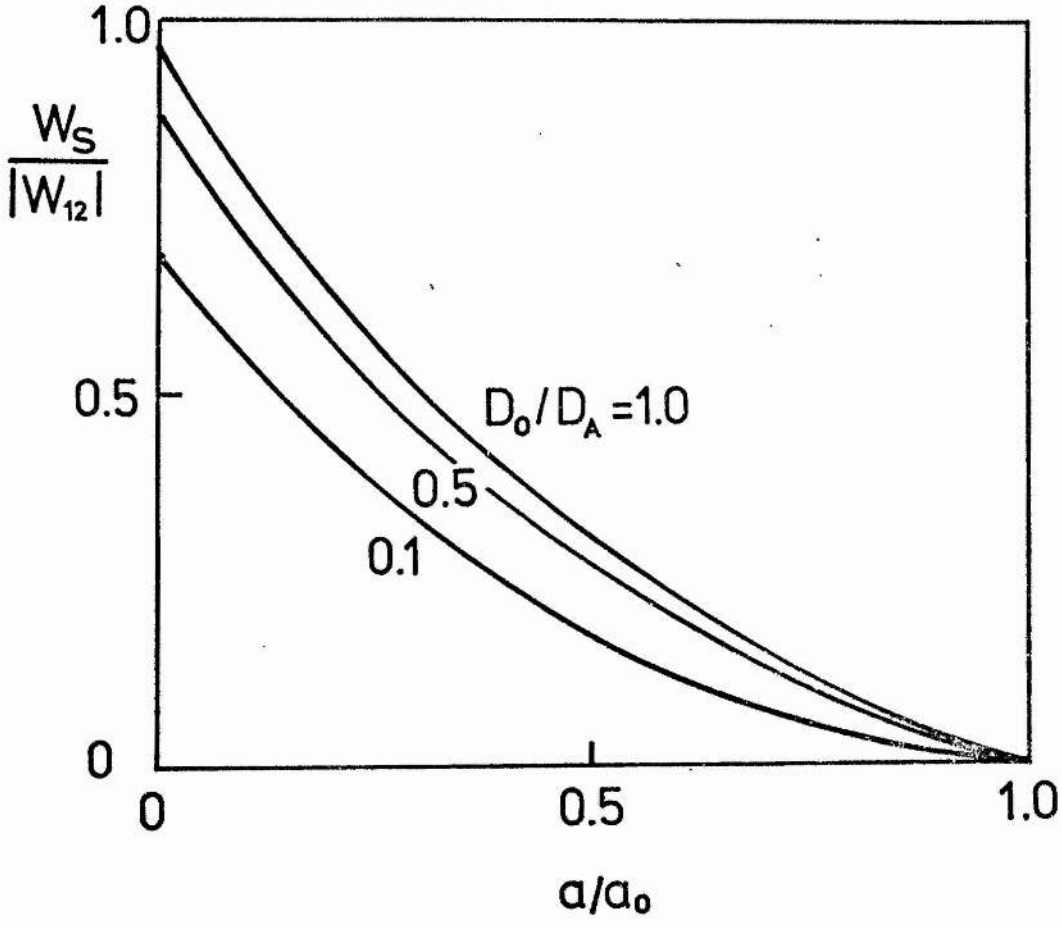

Figure 18.

The stored magnetic energy W_s due to the presence of the current sheet, relative to the mutual energy W_{12} of the dipoles, as two dipoles of moment D_o and D_A converge.

having used equations (2.18) and (2.29).

In Figure 17 the stored energy W_s is plotted against D/D_A as the moment D of the smaller dipole increases. W_s is there normalised with respect to the magnitude of the mutual energy W_{12} for the dipole sources alone. According to equation (2.35) the ratio of the total dipole source energy W_p to W_{12} is

$$W_p/W_{12} = a_2(D_A^2 + D_0^2) / 2 D_A D_0 r_0^2 - 1, \qquad (2.41)$$

which depends on the particular value one takes for the source size r_0. The stored energy W_s, normalized with respect to W_{12} may then be calculated from equations (2.37), (2.39), (2.40) and (2.41) for given r_0. For example, with a source size r_0 of order a, an increase in moment from $0.01\ D_A$ would provide $W_s/W_p \simeq 0.01$. If instead $r_0 = a/5$, W_p/W_{12} is much larger, and an increase from $0.1\ D_A$ to $0.25\ D_A$ would be required to produce the same ratio of stored to potential energy.

On the other hand one may estimate the energy stored, in excess of potential, as the dipoles converge, their moments being kept constant. In Figure 18, plots of stored energy are shown for various values of D_0/D_A as a/a_0 decreases.

2.4. CURRENT SHEET FORMATION ABOVE AN INCREASING DIPOLAR SOURCE.

Another interesting configuration arises when a dipole, of increasing moment, lies in a uniform magnetic field. Again, it is assumed that a current sheet forms as oppositely opposed flux is compressed at the x-type neutral point in the magnetic field. Figures 19 (a) and 19 (b) illustrate the behaviour

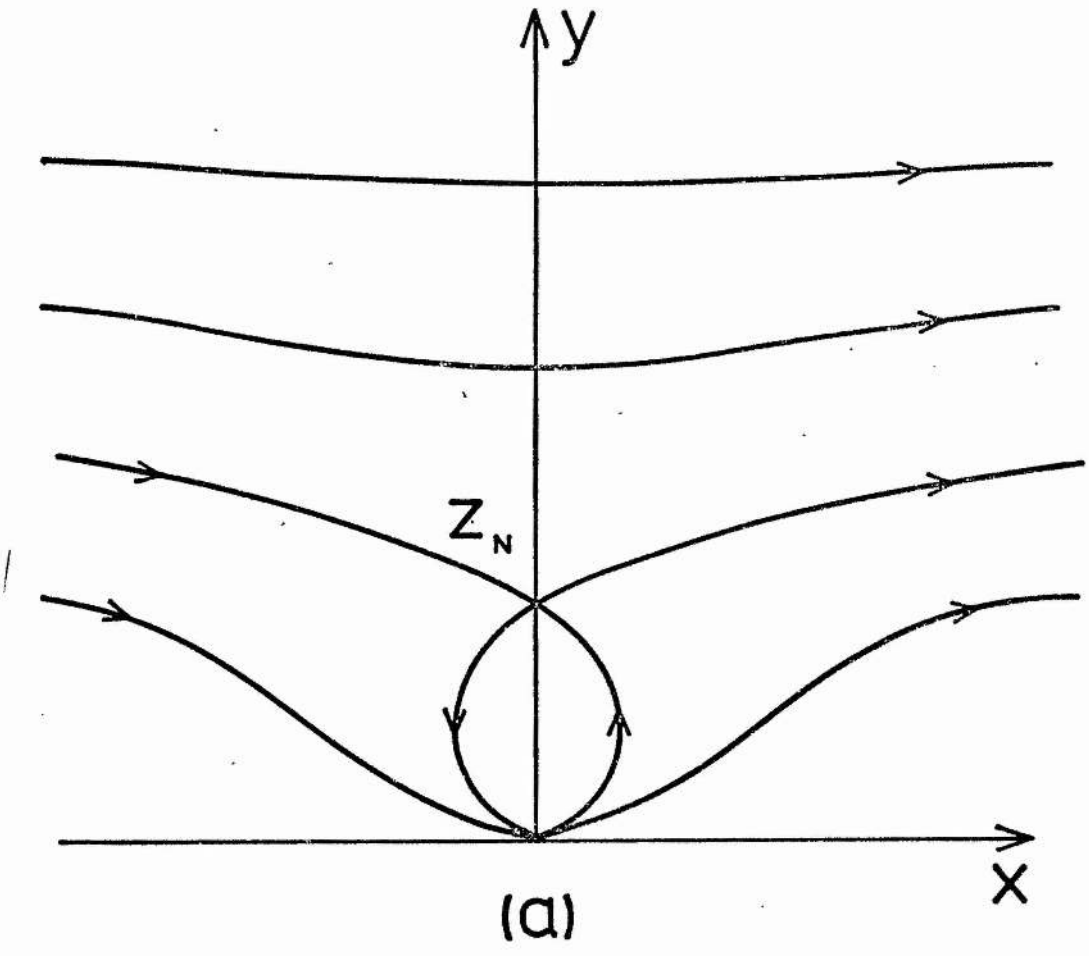

Figure 19a.

A schematic representation of the magnetic field due to a dipole of increasing moment in a uniform field. The initial, current-free situation.

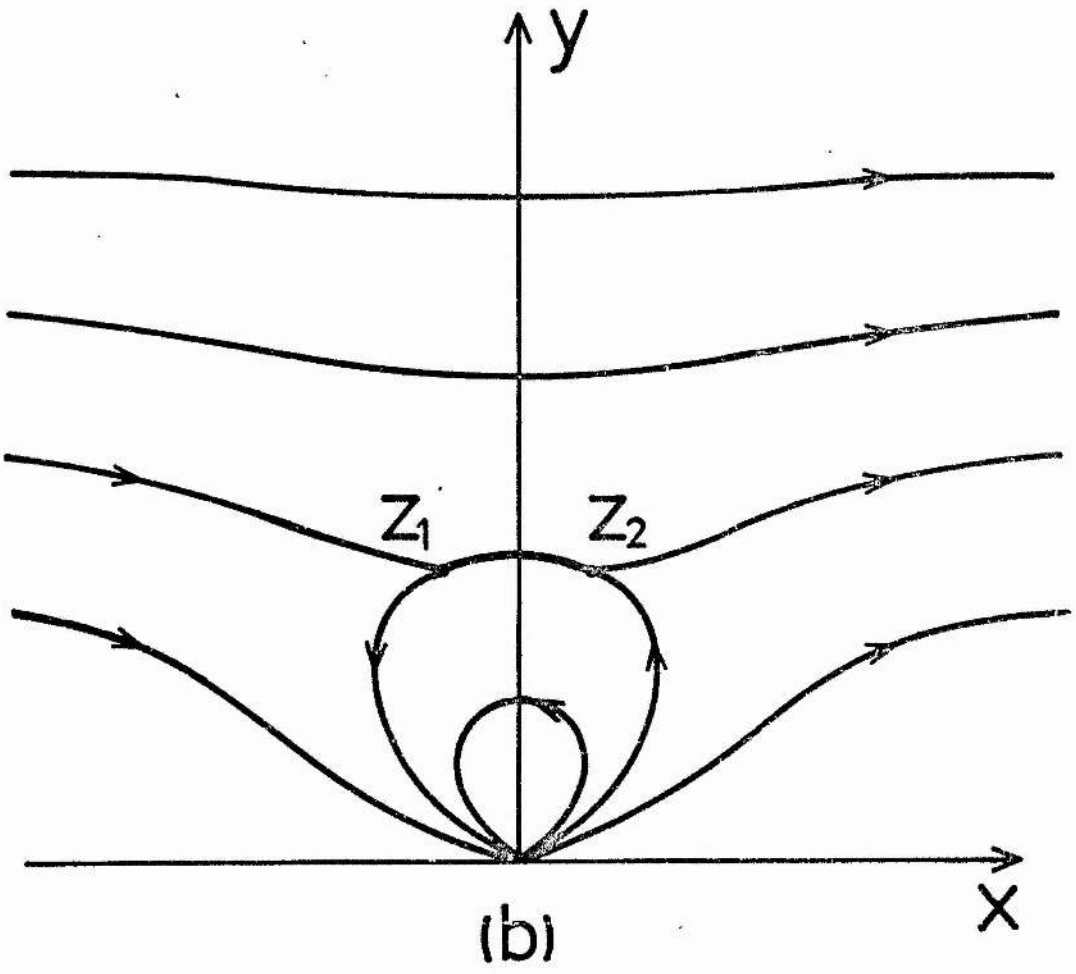

Figure 19b.

A schematic representation of the magnetic field due to a dipole of increasing moment in a uniform field. The final field bearing a current sheet joining z_1 and z_2.

of the field diagrammatically.

Suppose that initially there are no currents outside a dipole of moment $(2\pi D_0/\mu)\hat{\underline{x}}$, that is situated at the origin. The ambient field $\underline{b} = (b,0,0)$ is taken to be uniform. As in section 2.2, it is assumed that no reconnection occurs as the moment of the dipole increases to $(2\pi D/\mu)\hat{\underline{x}}$, so that a current sheet forms about the x-type neutral point as the dipolar and uniform fields press together.

The initial field may be represented by the analytic function

$$B_0(z) \equiv B_{ox} - iB_{oy} = b + \frac{D_0}{z^2} \quad , \qquad (2.42)$$

and similarly for the final field

$$B(z) \equiv B_x - iB_y = \frac{\left[(z^2 - z_1^2)(z^2 - z_1^{*})\right]^{1/2}}{z^2} \qquad (2.43)$$

where the end points of the current sheet are z and (by symmetry) $z_2 = -z_1^{*}$. The roots are defined to give the branch cuts from z_1 to z_2 and z_1^{*} to z_2^{*}.

Unlike the previous case there are now (due to symmetry of the field) only three unknowns to be found, namely E and $z_1 = x_1 + iy_1$. These may be determined from the boundary conditions at infinity where the field becomes uniform, and at the origin where the dipolar

behaviour of the source dominates, together with one condition of flux conservation. The boundary conditions yield

$$E = b \tag{2.44}$$

from the behaviour at infinity, and

$$b\, z_1 z_2 = D_0 \,, \tag{2.45}$$

from that at the origin.

The choice of flux condition is somewhat restricted by the presence of the uniform field which, in the ideal model presented here, is of infinite extent. For example, the flux crossing the positive y-axis is infinite. A contour stretching from the neutral point

$$y_N = \sqrt{\frac{D_0}{b}}$$

to $x = \infty$, parallel to the x-axis is therefore chosen for the flux condition. Initially the flux F_0 crossing this contour is calculated from

$$F_0 = \int_{x=0}^{\infty} \left[\mathrm{Im}\, B_0(z)^* \right]_{y=y_N} dx = \frac{D_0}{y_N} \tag{2.46}$$

having substituted from equation (2.42). Equating F_0 to the flux between $x = x_1$ and $x = \infty$ $(y = y_1)$, the final condition is

$$(bD_o)^{1/2} = \int_{x=x_1}^{\infty} \mathcal{I}_m B(z)^* \Big|_{y=y_1} dx \quad , \tag{2.47}$$

which has to be numerically evaluated.

The integration in equation (2.47) is not straightforward, owing to the infinite upper limit. Suppose that the range of integration were to be split at some large value of x, X say. The integral on the right hand side then becomes

$$\mathcal{I}_m \int_{x_1}^{X} \left[\sqrt{\left(1-\left(\frac{z_1}{z}\right)^2\left(1-\frac{z_2}{z}\right)^2\right)} \right]_{y=y_1} dx$$

$$+ \mathcal{I}_m \int_{X}^{\infty} \left[\sqrt{\left(1-\left(\frac{z_1}{z}\right)^2\right)\left(1-\left(\frac{z_2}{z}\right)^2\right)} \right]_{y=y_1} dx$$

Now, for sufficiently large X, the integrand of the latter contribution can be expanded as an infinite series to give

$$\mathcal{I}_m \int_{X}^{\infty} \left[\left(1-\tfrac{1}{2}\left(\frac{z_1}{z}\right)^2+\ldots\ldots\right)\left(1-\tfrac{1}{2}\left(\frac{z_2}{z}\right)^2+\ldots\ldots\right) \right]_{y=y_1} dx \, ,$$

which to highest order is

$$-\frac{1}{2}\,\mathcal{I}_m \int_X^\infty \left[\frac{z_1^2 + z_2^2}{z^2}\right]_{y=y_1} dx \simeq \frac{1}{X^2} \quad .$$

Hence by taking a large but finite upper limit of integration, the truncation error may be justifiably neglected. In practice an upper limit of $X = 50$ was used in the computation.

In Figure 20, the position of z_1 is plotted as the dipole moment of D increases relative to its original value D_0. It is seen that the locus of z_1 tends, approximately, to a straight line for D/D_0 much greater than 1.5. Again a few examples of the shape of the current sheet are shown, deduced from the flux condition (2.28).

The flux conditions (2.47) for the end point z_1 may be rearranged, using equations (2.43) and (2.44), to

$$1 = \int_{\bar{x}=\frac{x_1}{y_N}}^\infty \mathcal{I}_m \left\{ \frac{\sqrt{\left(Z^2 - \left(\frac{z_1}{y_N}\right)^2\right)\left(Z^2 - \left(\frac{z_2}{y_N}\right)^2\right)}}{Z^2} \right\} d\bar{x} \quad , \qquad (2.48)$$

where $\bar{x} = x/y_N$ and $Z = \bar{x} + i(y_i/y_N)$. The condition is therefore of the form

$$1 = f\left(\frac{x_1}{y_N} \quad , \quad \frac{y_1}{y_N}\right) \quad ,$$

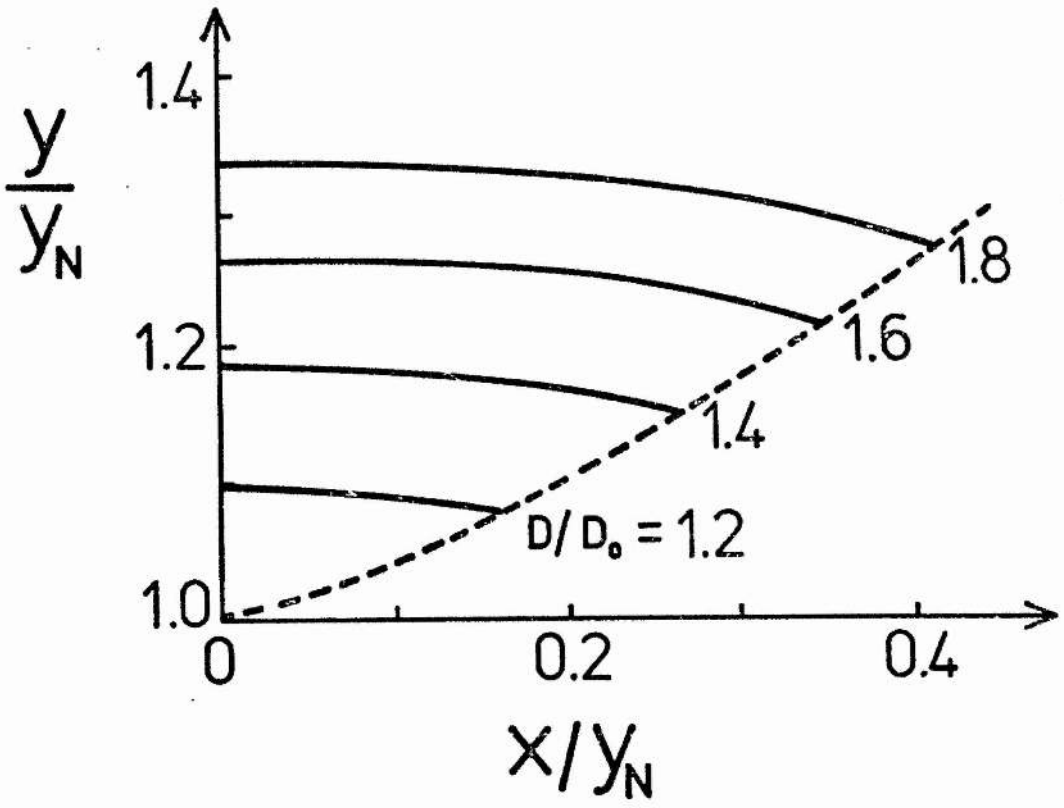

Figure 20.

The position of the end point $z_2(=-z_1^*)$ of the current sheet which forms between a constant horizontal field and a dipole (at the origin) whose moment increases. The shape of the right hand of the sheet is shown for a few cases.

for some function f, and so the slope of the curve shown in Figure 20 is independent of y_N. For large D/D_0 the gradient is approximately 0.8.

Similar methods to those outlined in the previous section may be used to evaluate the energy stored in this configuration. Again, infinite energies result from the idealized magnetic field source used. This difficulty is overcome by assigning a finite size, r_0, for the dipole source, as before, and also a length scale, L_0, for the extent of the ambient field $\underline{b}$.

The potential energy (W_p) associated with the initially current-free field is

$$\frac{W_p}{W_M} \simeq \frac{1}{4}\left(\frac{y_N}{r_0}\right)^2 + \frac{1}{8}\left(\frac{L_0}{y_N}\right)^2 - 1 \quad , \tag{2.49}$$

normalized with respect to the mutual energy, W_M, between the dipole and the uniform magnetic field,

$$W_M = \frac{-2\pi D_0 b}{\mu}$$

In the final state the magnetic energy due to the presence of the current sheet in the upper-half plane is given by

$$W_s = W_3 + W_{13} + W_{23} + \frac{1}{2} W_{43} \quad , \tag{2.50}$$

where the subscripts 1, 2, 3 and 4 refer to the uniform field, the dipole and the current sheet and its image, respectively. Using

equations (2.30), (2.31) and (2.32), the stored energy may be rewritten as

$$W_s = \frac{1}{2} \int_{\text{Sheet}} (A_s + A_b) j \, dV + \frac{\pi D}{2\mu} \left[b + \frac{D(x_1^2 - y_1^2)}{(x_1^2 + y_1^2)^2} \right] \qquad (2.51)$$

where A_b is the potential due to the field b at the sheet, and may be approximated by by_N for sheets of small length compared with Y_N. Also

$$A_s = by_N + D_o y_N^{-1}$$

is the potential due to the entire field at the current sheet. The integral in equation (2.51) may, after using Stokes' theorem, be approximated by

$$\frac{(A_s + A_b)}{4\mu} \quad Re \int_{z_2}^{z_1} B(z) \, dz \quad ,$$

where B(z) is given by (2.43). Equation (2.51) therefore reduces to

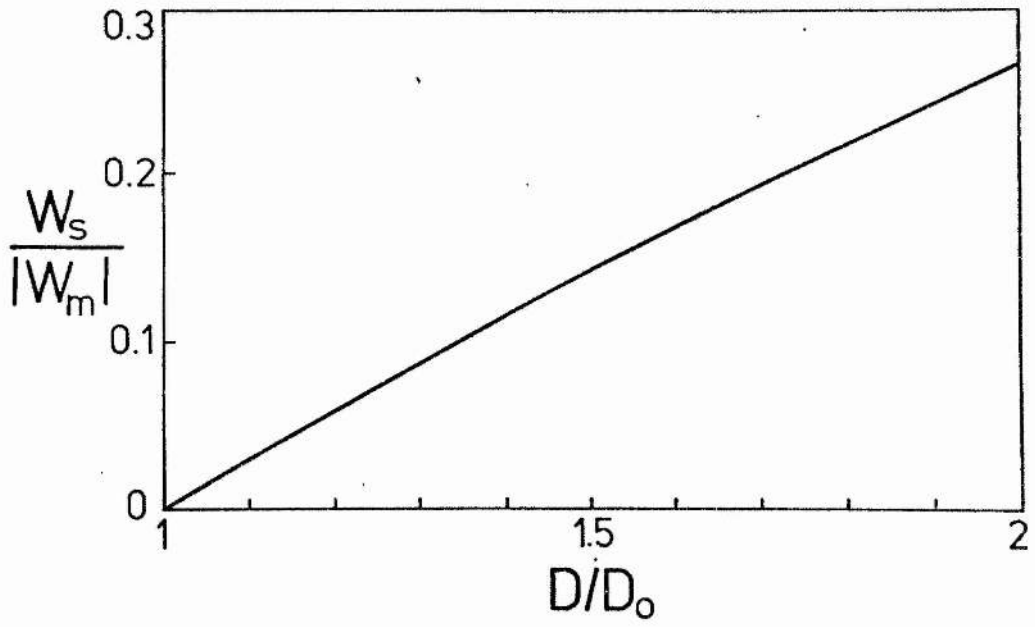

Figure 21.

The stored magnetic energy W_s for a dipole of moment D emerging into a uniform field, relative to the mutual energy W_m between the dipole and the uniform background field.

$$\frac{W_S}{|W_M|} \sim \frac{3}{8\pi y_N} \operatorname{Re} \int_{z_1}^{z_2} \frac{\left[(z^2-z_1^2)(z^2-z_2^2)\right]^{1/2}}{z^2} \, dz$$

$$+ \frac{D}{4D_0}\left[1 + \frac{D}{D_0}\left(\frac{y_N^2 (x_1^2 - y_1^2)}{(x_1^2+y_1^2)^2}\right)\right], \qquad (2.52)$$

the integral being evaluated along the top of the branch cut. The results of the numerical computation of the stored energy are shown in Figure 21 where $W_S/|W_M|$ is plotted as a function D/D_0 .

2.5. SHEET FORMATION BETWEEN DIVERGING DIPOLE SOURCES.

As a final illustration of current sheet formation, the situation that arises when two sources are moved apart is investigated. Syrovatskii (1966) points out that for the two line currents considered in his model, separation of the sources would result in a current sheet being formed along the horizontal rather than the vertical axis. This is equivalent to a rotation of the axes in Figure 3 through 90^0. In this section the current sheet formed between two dipoles, moving away from each other, is studied.

Suppose that initially there are no currents outside two dipole sources of moment $(2\pi D/\mu)\,\hat{\underline{x}}$, situated at $x = \pm a_0$ of the complex plane. Assuming no reconnection occurs as the dipoles move to their new positions $x = \pm a$ $(a > a_0)$, a current sheet will form about the neutral point as the field lines above and below it are drawn together (Figure 22.)

In the usual manner the analytic expression for the initial

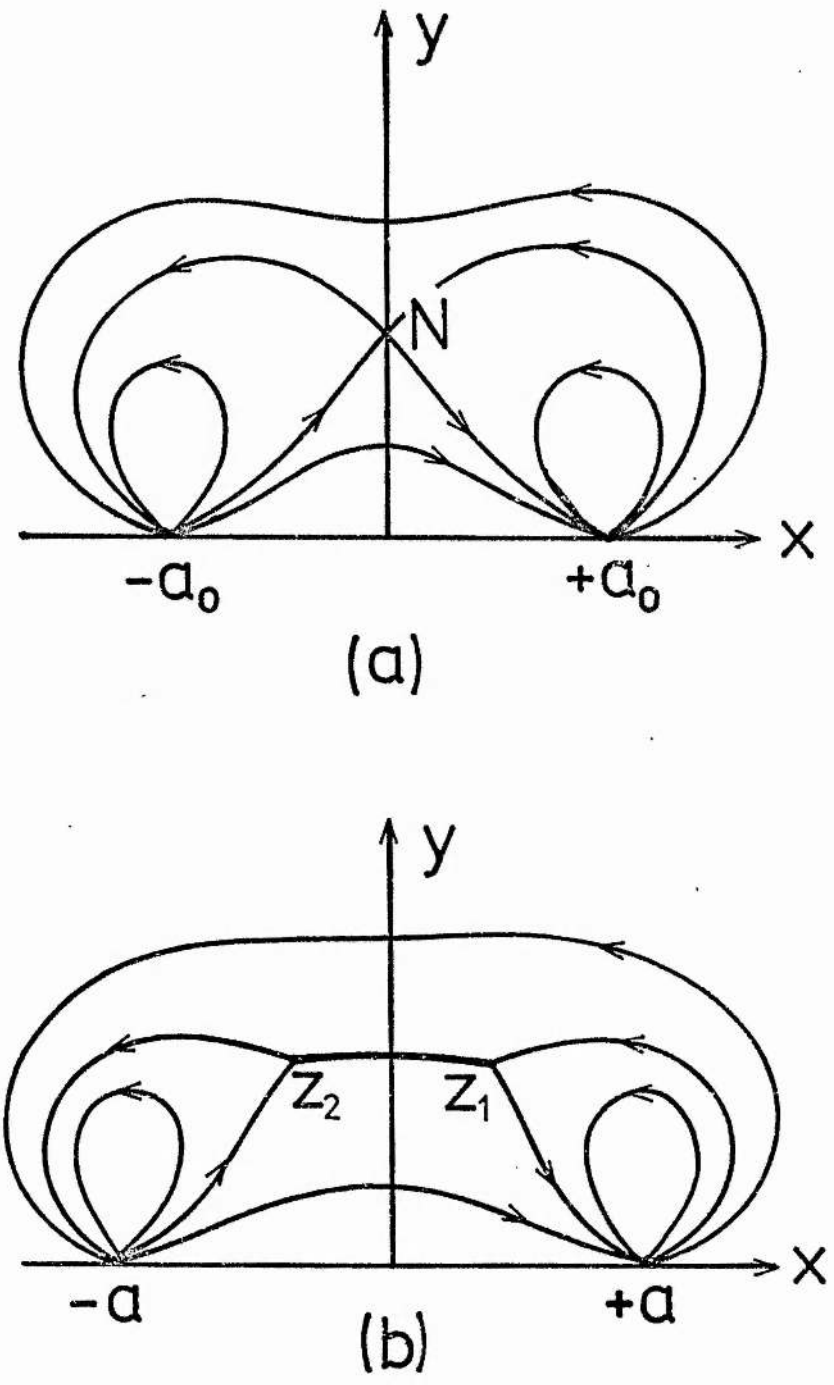

Figure 22.

A schematic representation of the magnetic field due to two dipoles of equal moment, (a) in the initial current-free situation, (b) after the dipoles have moved to their new positions $x=\pm a$ ($a>a_o$); a current sheet joins z_1 and z_2.

field is

$$B_0(z) \equiv B_{0x} - i\, B_{0y} = \frac{2D(z^2 + a_0^2)}{(z^2 - a^2)^2} \tag{2.53}$$

and similarly for the final field

$$B(z) \equiv B_x - i\, B_y = \frac{E\left[(z^2 - z_1^2)(z^2 - z_2^2)\right]^{\frac{1}{2}}}{(z^2 - a^2)^2} \tag{2.54}$$

where the square roots are defined to give the cuts. By symmetry, $z_1 = -z_2^*$ and $z_2 = -z_1^*$. The constant E may be determined from the behaviour of the field as $z^2 \longrightarrow a^2$; hence

$$E = \frac{4Da^2}{\left[(a^2 - z_1^2)(a^2 - z_2^2)\right]^{\frac{1}{2}}} \tag{2.55}$$

The two remaining unknowns, x_1 and y_1 are deduced from the flux conditions. Firstly, equating the total flux crossing the y-axis in both cases (it is identically zero as in section 2.2), yields the condition

$$0 = \mathrm{Re} \int_0^\infty \left[B(z)\right]_{x=0} dy,$$

or

$$0 = \tfrac{1}{2}\,\mathrm{Re} \int_{-\infty}^{\infty} \frac{E\sqrt{(y^2 + z_1^2)(y^2 + z_2^2)}}{(a^2 + y^2)^2}\, dy \quad , \tag{2.56}$$

since the integrand is an even function. Completing the contour and

calculating the residues, equation (2.56) reduces to

$$z_1^2 \, z_2^2 = a^4 \quad ,$$

which with $z_1 = - z_2^*$ becomes simply

$$r = a \quad , \tag{2.57}$$

where $r = |z_1| = |z_2|$. As in section 2.2, the flux conservation equations produce an extremely simple result that points to the existence of a mapping from one current sheet bearing field to another. Again, however, no transformation could be found. The second condition is obtained by equating the flux crossing ON in the first instance with that crossing the line $x = x_1$ from $y = 0$ to y_1 in the final configuration, that is,

$$\frac{D}{q_0} = \int_0^{y_1} \left[B_x \right]_{x = x_1} \, dy \quad . \tag{2.58}$$

Finally, the shape of the current sheet may be found using equation (2.28). Several examples of this are shown in Figure 23.

2.6. APPLICATION TO SOLAR FLARES.

Two of the configurations discussed in this chapter may be used to model possible current sheet formation prior to solar flares. The first, in which a dipole increases its moment relative to its much larger neighbour, may simulate the emergence of a satellite spot pair near the edge of a pre-existing bipolar group. Flare activity is

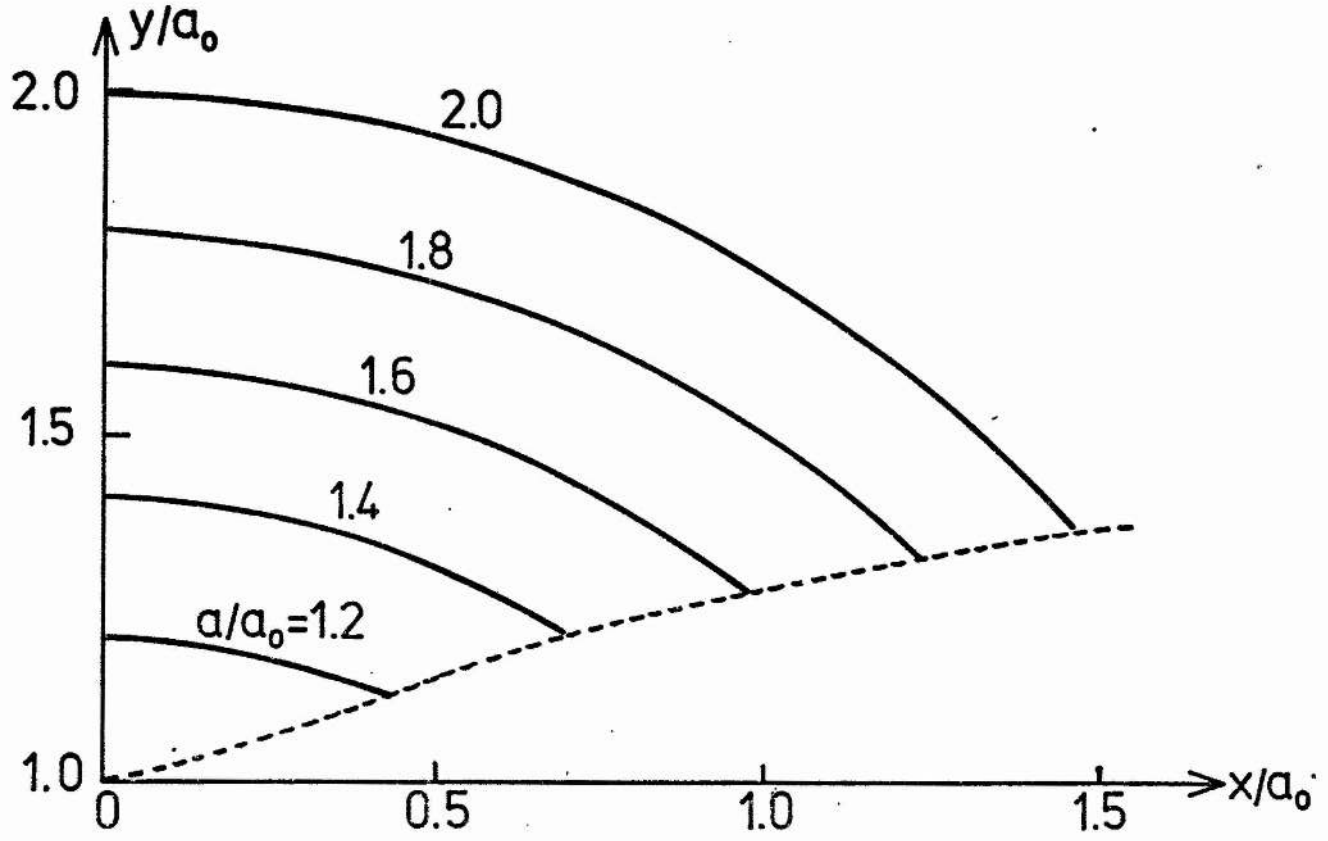

Figure 23.

The position of the end point z_1 (dashed) of the current sheet formed when two equal dipoles move apart. The shape of the right half of the sheet is shown for a few cases.

often observed in these circumstances (Rust, 1968). Secondly, when new flux emerges directly beneath a uniform magnetic field, a current sheet may form as the model in section (2.4) suggests.

The former configuration is similar to that envisaged by Priest and Heyvaerts (1974) when considering the so-called absorbing features discussed by Matres et al. (1972). They focus their attention on absorbing features occurring at the edge of an active region. These, it is suggested, may be due to small surges from the ends of the current sheet (formed as satellite flux emerges), as it becomes unstable.

The model is consistent with the observations of Homologous flares. A cycle of events may be envisaged in which flux emerges at (for example) the edge of a bipolar flux region, forming a current sheet. At some stage the sheet becomes susceptible to an instability that triggers a flare and, possibly, the ejection of matter in a direction determined by its position. The current sheet is then dissipated, and the cycle recurs as flux continues to emerge. Subsequent flares will therefore arise from similar magnetic field configurations to the first, so accounting for the observed properties of homology.

The initial, purely potential, configuration in each case represents the minimum energy associated with the system. This follows directly from the theorem proved in section (1.2). It is therefore only the energy stored in excess of potential which can be released during a flare. This extra energy may be stored when chromospheric (and coronal) currents are produced by the relatively slow motions of underlying photospheric plasma. The magnetic

Reynolds' number (R_m) for a scale length of 10^6m and a plasma speed of order 10^3m s^{-1} is large ($R_m \simeq 10^7$ when the resistivity η is about 10^2 $m^2 s^{-1}$) and so the magnetic field may be regarded as being "frozen-into" the plasma. The motions of the photospheric plasma therefore distort the overlying magnetic fields to produce two types of current.

(i) Volume currents which satisfy the force-free condition (equation (1.21)) arise from, for example, the twisting motions of the feet of the flux tubes (Alfvén and Carlqvist, 1967., Anzer, 1968; Low 1973).

(ii) A current sheet may evolve at the boundary between converging magnetic flux regions of opposite polarity (Sweet, 1958 a,b; Sturrock, 1972).

Although both types may, in general, be associated with flare production, only the latter is relevant to the subject of the present thesis.

If one takes typical values of 10^{25} j for the total energy output of a large event, and 10^{27} j as the energy of a large active region (roughly equivalent to a field of 5×10^{-2} tesla contained in a volume of 10^{24} m^3) , then the potential field will produce energy sufficient for a flare if perturbed by a factor of only 1%.

From the Figures 17 and 21, it is clearly seen that such energies are easily achieved. In the first example, with a source size r_0 of order a, an increase in moment from 0.01 D_A to 0.035 D_A would provide W_s/W_p 0.01. If instead $r_0 = a/5$, W_p/W_{12} is much

larger and an increase from 0.01 D_A to 0.25 D_A is required. For an emerging bipolar group, taking source size r_0 of order Y_N and $L_0 \simeq 10\ Y_N$ for the sake of illustration, an increase in dipole moment to approximately 1.5 times its original value is sufficient. Again, if $r_0 = Y_N/5$, say, then the dipole moment needs to increase to 1.7 times its initial value to make $W_s/W_p \simeq 0.01$. In either case the corresponding length of the current sheet is small compared with a typical length scale for the problem: the dipole separation 2a, or the height of the initial neutral point Y_N.

When applying these idealized models to the solar atmosphere, some restrictions must be imposed on the speed at which new magnetic flux emerges.

At one extreme the flux must emerge at a speed which is much less than the Alfvén speed (V_A), so that a series of equilibria can be established. This assumption is valid sufficiently high in the atmosphere. In the photosphere, where the magnetic field strength and number density may be 0.1 tesla and 10^{22} m^{-3} respectively, the Alfvén speed is only 2×10^4 ms^{-1}. But, for instance, in the chromosphere, where the field strength may be 0.01 tesla and the number density 10^{16} m^{-3}, say, the Alfvén speed takes a value 2×10^6 ms^{-1}, much larger than the observed speeds for emerging flux (10^3 to 10^4 ms^{-1}).

A lower limit for the speed at which flux merges at the current sheet is imposed by the assumption that there is no significant reconnection. This is a most stringent supposition since the strong excess gas pressure inside the current sheet tries to eject plasma and magnetic flux from its ends. It is valid provided the flux merges at a speed which is much greater than the largest allowable

reconnection speed V_{max}. However, V_{max} itself depends on the details of the reconnection process. In the photosphere and chromosphere the latest results (Priest and Soward, 1976) indicate that V_{max} may be as low as $V_A/40$, for $R_m = 10^8$.

In view of the above restrictions on the validity of present non-reconnecting current sheet models, it is convenient to divide the solar atmosphere into three regimes. Very low down $V \simeq V_A$ and the analysis fails, because appreciable volume currents are present. At intermediate heights, in perhaps the low chromosphere, $V_{max} < V < V_A$ and a current sheet forms with no reconnection, as described in this chapter. Higher up, $V < V_{max}$ and so the emerging flux reconnects with the overlying field. Still higher, in the lower corona, the fluid equations fail and a collisionless theory becomes necessary. However, in this regime, the theory is not sufficiently well developed to determine the limitations on the reconnection process, if it should prove that reconnection is inhibited in some cases, the present analysis may be relevant there too.

CHAPTER 3

A MODEL FOR A THREE DIMENSIONAL CURRENT SHEET

3.1. THE MAGNETIC FIELD EQUATIONS.

The techniques so far employed to study the development of current sheets rely on the use of complex variable expressions for the magnetic field. As soon as an attempt is made to generalize to three dimensions, the complex variable method becomes redundant, and a new approach must be sought.

In this chapter, a simple three-dimensional current sheet is considered. For simplicity, the symmetric field arising from two codirectional magnetic dipole sources of equal moment is considered. It is assumed that, as the sources move towards each other in a perfectly conducting medium, an annular neutral current sheet is formed in the plane midway between them (Figures 24(a) and (b)). This configuration closely resembles the two-dimensional picture in which two equal line dipoles approach along the real axis of the complex plane to form a current sheet on the imaginary axis (Priest and Raadu, 1975). The problem has been set up in spherical polar coordinates (r, θ, ϕ), although cylindrical coordinates could probably have been used. However, there is no azimuthal (ϕ) dependence in view of the symmetry of the problem.

Suppose two dipoles, each of moment $(2\pi D/\mu)\hat{\underline{u}}$, lie initially at $r = \alpha_0$ on the radius vectors $\theta = 0$ and $\theta = \pi$, where $\underline{u}$ is a unit vector perpendicular to the $\theta = \pi/2$ plane, that is

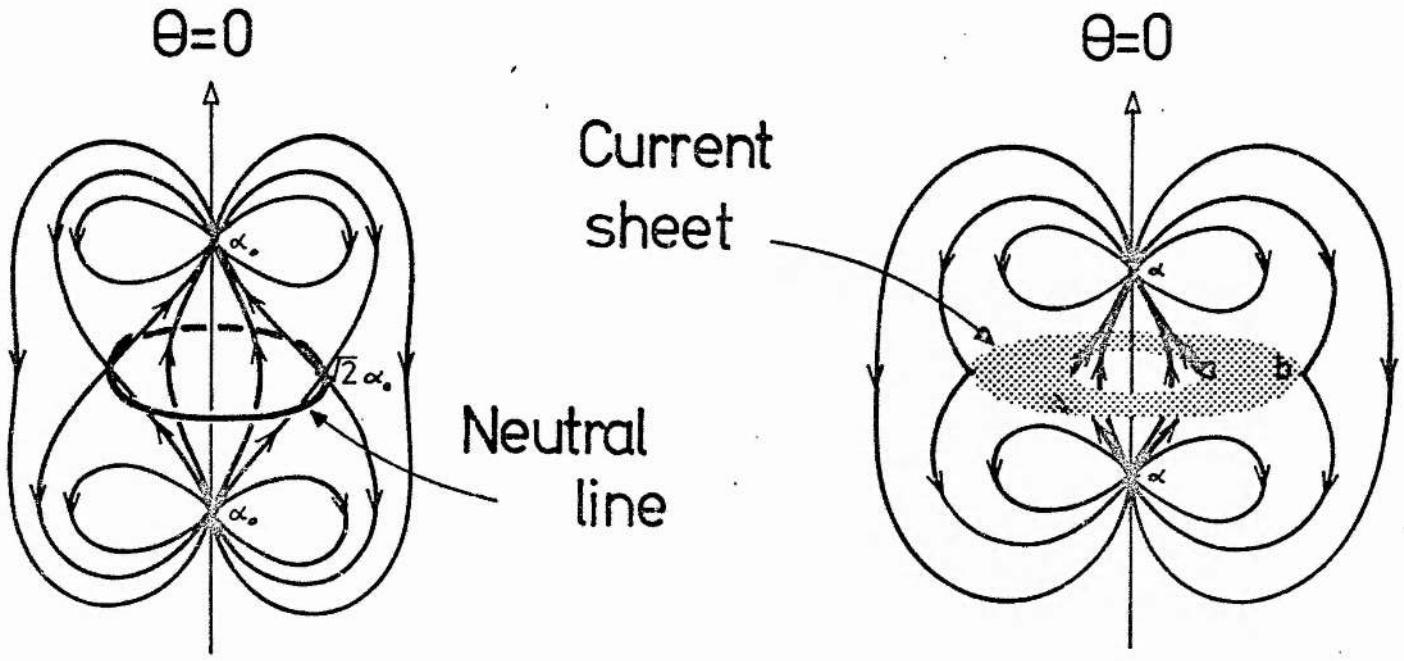

Figure 24.

Schematic representation of the three- dimensional magnetic field due to two dipoles. (a) The purely potential field. (b) The field resulting from a movement of the dipoles towards each other. A current sheet forms an annulus in the $\theta = \pi/2$ plane.

$$\hat{\underline{u}} = (\hat{\underline{r}})_{\Theta} = 0$$

The resulting magnetic field $\underline{B}_0$ is current-free outside the sources and therefore a scalar potential Φ_0 for the field may be found such that

$$\underline{B}_0 = - \nabla \Phi_0 \quad , \tag{3.1}$$

where

$$\Phi_0 = \frac{D \cos \Theta_1}{r_1} + \frac{D \cos \Theta_2}{r_2} \quad ,$$

r_1, r_2, Θ_1 and Θ_2 being shown in Figure 25, that is

$$\Phi_0 = \frac{D(r \cos \Theta - \alpha)}{\{\alpha^2 - 2\alpha r \cos \Theta + r^2\}^{3/2}} + \frac{D(r \cos \Theta + \alpha)}{\{\alpha^2 + 2\alpha r \cos \Theta + r^2\}^{3/2}} \tag{3.2}$$

If the two dipoles are moved close together without reconnection, an annular current sheet is assumed to form between $r = a$ and $r = b$ ($\Theta = \pi/2$) about the former neutral line. Again, as there are no currents outside the sources on the current sheet, the field $\underline{B}$ may be described by a scalar potential Φ. The solution to Laplace's equation,

$$\nabla^2 \Phi = 0 \quad , \tag{3.3}$$

is therefore required, subject to the boundary conditions imposed by the current sheet and the sources. The principle of superposition is used to construct a solution which is an integral sum of the potentials arising from the individual current loops which one may suppose to make up the current sheet.

The field $\underline{B}$ may be considered to be due to three sources, namely the two dipoles and the current sheet. One then defines Φ as

$$\Phi = \Phi_s + \Phi_D \,, \tag{3.4}$$

where Φ_s is the potential arising solely from the current sheet, and Φ_D is that arising from the dipole sources.

The potential Φ_s may be found as follows. The potential Ω at a point $r = d$ on the axis of symmetry ($\Theta = 0$), due to a circular current loop of radius ρ in the plane $\Theta = \pi/2$ is (Jeans, 1911, p. 341)

$$\Omega = 2\pi I(\rho) \left[1 - \frac{d}{(\rho^2 + d^2)^{1/2}} \right] \,, \tag{3.5}$$

where $I_{(\rho)}$ is the current in the loop. The right hand side of equation (35) may be expanded, using the binomial theorem, to yield

$$\Omega = \begin{cases} 2\pi I(\rho) \left[1 - \sum_{n=0}^{\infty} (-1)^n \frac{(2n)!}{4^n (n!)^2} \left(\frac{d}{\rho} \right)^{2n+1} \right] & d < \rho \\ 2\pi I(\rho) \left[\sum_{n=1}^{\infty} (-1)^{n+1} \frac{(2n)!}{4^n (n!)^2} \left(\frac{\rho}{d} \right)^{2n} \right] & d > \rho \end{cases} \tag{3.6}$$

For a point (r, Θ) off the axis of symmetry, the potential (ϕ_ρ) due to a current loop in the $\Theta = \pi/2$ plane may be expressed as the solution to Laplace's equation, in spherical polars, as

$$\phi_\rho = \sum_{n=0}^{\infty} A_n r^n P_n(\cos\Theta) \tag{3.7}$$

Because a finite field strength is required on the $\Theta = 0$ axis, the terms involving $r^{-(n+1)}$ have been suppressed. The coefficients A_n may be determined by the values of the potential along the axis of symmetry given by equation (3.6). Thus ϕ_ρ becomes

$$\phi_\rho = \begin{cases} 2\pi I(\rho) \left[1 - \sum_{n=0}^{\infty} (-1)^n \frac{(2n)!}{4^n (n!)^2} \left(\frac{r}{\rho}\right)^{2n+1} P_{2n+1}(\cos\Theta)\right] & (r < \rho) \\ 2\pi I(\rho) \sum_{n=1}^{\infty} (-1)^{n+1} \frac{(2n)!}{4^n (n!)^2} \left(\frac{\rho}{r}\right)^{2n} P_{2n-1}(\cos\Theta) & (r > \rho) \end{cases} \tag{3.8}$$

The potential $\bar{\Phi}_B$ due to the current annulus may be taken as the

integral over ρ of $\phi\rho$ from a to b, the inner and outer radii of the sheet. Care must be taken to split the range of integration at $\rho = r$, since $\phi\rho$ changes in form at this point. In terms of the spherical polars (r, θ, ϕ), Φ_s may be written

$$\Phi_s(r,\theta) = \begin{cases} 2\pi \int_a^b \left[1 - \sum_{n=0}^{\infty} (-1)^n \frac{(2n)!}{4^n (n!)^2} \left(\frac{r}{\rho}\right)^{2n+1} P_{2n+1}(\cos\theta)\right] I(\rho)\, d\rho, \\ \qquad (r < a) \\ 2\pi \int_a^r \sum_{n=1}^{\infty} (-1)^{n+1} \frac{(2n)!}{4^n (n!)^2} \left(\frac{\rho}{r}\right)^{2n} P_{2n-1}(\cos\theta) I(\rho)\, d\rho \\ \quad + 2\pi \int_r^b \left[1 - \sum_{n=0}^{\infty} (-1)^n \frac{(2n)!}{4^n (n!)^2} \left(\frac{r}{\rho}\right)^{2n+1} P_{2n+1}(\cos\theta)\right] I(\rho)\, d\rho, \\ \qquad (a < r < b) \\ 2\pi \int_a^b \sum_{n=1}^{\infty} (-1)^{n+1} \frac{(2n)!}{4^n (n!)^2} \left(\frac{\rho}{r}\right)^{2n} P_{2n-1}(\cos\theta) I_\rho\, d\rho. \\ \qquad (r > b) \end{cases} \tag{3.9}$$

The problem is now reduced to that of determining the unknown function $I(\rho)$ from the boundary conditions on Φ_s at $\Theta = \pi/2$. These conditions are found by subtraction of the (known) boundary conditions for Φ and Φ_D as follows. Firstly, the $\Theta = \pi/2$ plane is split into two domains, the annular current region ($a \leq r \leq b$) and the remaining exterior ($0 \leq r < a$) and ($r > b$), denoted by N and M respectively. The net field is then normal in M and tangiential in N (see Figure 25), so that the boundary conditions on Φ are

$$\left[\frac{\partial \Phi}{\partial n}\right]_{\Theta=\pi/2} = 0 \qquad (\text{for } r \text{ in } N)\,;$$

$$\left[\frac{\partial \Phi}{\partial t}\right]_{\Theta=\pi/2} = 0 \qquad (\text{for } r \text{ in } M)\,; \tag{3.10}$$

where $\partial/\partial n$ and $\partial/\partial t$ denote the normal and tangiential derivatives $\partial/r\partial\Theta$ and $\partial/\partial r$, respectively. Using equation (3.2) for the potential due to the two dipoles alone, one has

$$\left[\frac{\partial \Phi_D}{\partial n}\right]_{\Theta=\pi/2} = \frac{2D(r^2 - 2a^2)}{(r^2+a^2)^{5/2}} \qquad (r \text{ in } N)\,,$$

$$\left[\frac{\partial \Phi_D}{\partial t}\right]_{\Theta=\pi/2} = 0 \qquad (r \text{ in } M)\,. \tag{3.12}$$

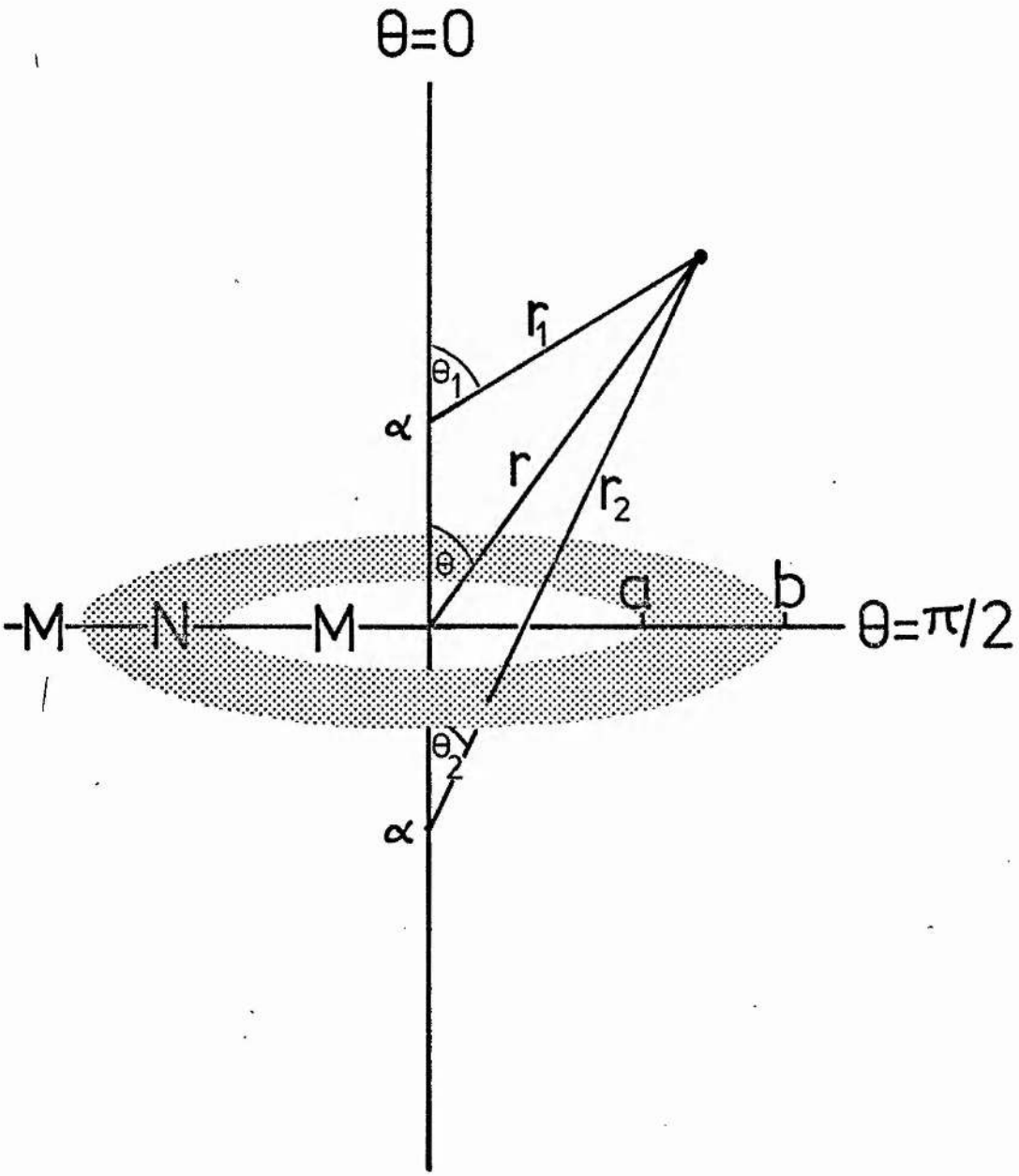

Figure 25.

Sketch illustrating some of the parameters used in the problem.

Subtraction of equation (3.12) from equation (3.10) therefore gives the boundary conditions on Φ_s, namely

$$\left[\frac{\partial \Phi_s}{\partial n}\right]_{\Theta=\pi/2} = \frac{-2D(r^2-2a^2)}{(r^2+a^2)^{5/2}} \qquad (r \text{ in } N), \tag{3.13}$$

$$\left[\frac{\partial \Phi_s}{\partial t}\right]_{\Theta=\pi/2} = 0 \qquad (r \text{ in } M).$$

These are the boundary conditions to be satisfied by the function Φ_s which is given in (3.9). Having substituted in (3.13) one finds, after some lengthy manipulation, that the second condition is automatically satisfied. This result may easily be deduced from physical considerations as follows. The magnetic field lines, in a plane ϕ = constant, due to the current sheet alone will form a family of closed loops about the two sections of the current sheet in that plane. Due to the symmetry of the problem, these field lines will be normal to the $\Theta = \pi/2$ axis in the M region, and hence $(\partial\Phi/\partial t)$ will be identically zero there. The first condition, however, yields the following integral equation for the unknown function $I(\rho)$.

$$2\pi \int_a^r \sum_{n=1}^{\infty} (-1)^{n+1} \frac{(2n)!\,(2n-1)\,P_{2n-2}(0)}{4^n (n!)^2 r} \left(\frac{\rho}{r}\right)^{2n} I(\rho)\, d\rho$$

$$- 2\pi \int_r^b \sum_{n=0}^{\infty} (-1)^n \frac{(2n)!\,(2n+1)\,P_{2n+2}(0)}{4^n (n!)^2 r} \left(\frac{r}{\rho}\right)^{2n+1} I(\rho)\, d\rho$$

$$= \frac{-2D(r^2 - 2\alpha^2)}{(r^2+\alpha^2)^{5/2}}, \qquad (a \le r \le b).$$

(3.14)

In the following section a numerical solution of this equation is presented.

3.2 NUMERICAL SOLUTION OF THE INTEGRAL EQUATION.

Expanding the Legrendre polynomials in equation (3.14), the integral equation for $I(\rho)$ may be written

$$2\pi \int_a^r \sum_{n=1}^{\infty} \left[\frac{(2n)!}{(n!)^2 4^n}\right]^2 2n \left(\frac{\rho}{r}\right)^{2n} \frac{I(\rho)}{r}\, d\rho$$

$$- 2\pi \int_r^b \sum_{n=0}^{\infty} \left[\frac{(2n)!}{(n!)^2 4^n}\right]^2 (2n+1) \left(\frac{r}{\rho}\right)^{2n+1} \frac{I(\rho)}{r}\, d\rho$$

$$= \frac{-2D(r^2 - 2\alpha^2)}{(r^2+\alpha^2)^{5/2}},$$

(3.15)

or in short

$$\int_a^r K_1(r,\rho)\, I(\rho)\, d\rho + \int_r^b K_2(r,\rho)\, I(\rho)\, d\rho = F(r), \tag{3.16}$$

where the kernels K_1 and K_2 and the function $F(r)$ are defined by comparison with the preceding equation.

This integral equation is not strictly a Volterra equation although the independent variable r appears as a limit of integration. Using the unit step function U, defined by

$$U(x-a) = \begin{cases} 0 & x < a \\ 1 & x > a \end{cases},$$

equation (3.16) may be written

$$\int_a^b \left[K_1(r,\rho)\left\{1 - U(\rho - r)\right\} + K_2(r,\rho)\, U(\rho - r) \right] I(\rho)\, d\rho = F(r),$$

which is a Fredholm equation of the first kind. However, this does not admit an analytic solution so a numerical procedure has been applied.

Firstly, the convergence of the kernels K_1 and K_2 must be examined. The ratio test reveals that the series converges provided

$$\begin{cases} \rho < r & \text{for } K_1 \\ \rho > r & \text{for } K_2 \end{cases}$$

when $\rho = r$, the ratio test fails to determine the convergence of the series. Instead, the asymptotic behaviour of the general term in either series is considered. Using Stirling's formula

$$n! \simeq (2\pi n)^{1/2} n^n e^{-n} ,$$

the n^{th} term in the series expansions for K_1 and K_2 may be approximated by

$$\begin{cases} \left[\dfrac{(2n)!}{(n!)^2 4^n}\right]^2 \dfrac{2n}{r}\left(\dfrac{\rho}{r}\right)^{2n} \simeq \dfrac{1}{\pi n} \cdot \dfrac{2n}{r}\left(\dfrac{\rho}{r}\right)^{2n} \\ \left[\dfrac{(2n)!}{(n!)^2 4^n}\right]^2 \dfrac{2n+1}{r}\left(\dfrac{r}{\rho}\right)^{2n+1} \simeq \dfrac{1}{\pi n} \cdot \dfrac{(2n+1)}{r}\left(\dfrac{r}{\rho}\right)^{2n+1} \end{cases} \qquad (3.17)$$

which, for $r = \rho$, imply divergent series.

Despite the divergent behaviour of the above series, the sum of the integrals of equation (3.15) can be shown as follows to be convergent at $\rho = r$. Substituting the above approximations into the left hand side of equation (3.15), this becomes

$$A + \frac{4}{r}\left[\int \sum_{n=n^*}^{\infty} \left(\frac{\rho}{r}\right)^{2n} I(\rho)\, d\rho - \int_{r}^{b} \sum_{n=n^*}^{\infty} \left(\frac{r}{\rho}\right)^{2n+1} \frac{(n+1)}{2n} I(\rho)\, d\rho\right]$$

where for a sufficiently large value of n, n^* say, A is the (finite) sum of the first $n^* - 1$ integrals. The range of integration for the remaining integrals may be aplit into three parts (a, r_-), (r_-, r_+) and (r_+, b), where r_- and r_+ are values of ρ lying close to r. Thus the above expression becomes

$$A + \frac{4}{r}\left[\int_{a}^{r_-} \sum_{n^*}^{\infty} \left(\frac{\rho}{r}\right)^{2n} I(\rho)\, d\rho - \int_{r_+}^{b} \sum_{n^*}^{\infty} \left(\frac{r}{\rho}\right)^{2n+1} \frac{n+1}{2n} I(\rho)\, d\rho\right.$$

$$\left. + \int_{r_-}^{r} \sum_{n^*}^{\infty} \left(\frac{\rho}{r}\right)^{2n} I(\rho)\, d\rho - \int_{r}^{r_+} \sum_{n^*}^{\infty} \left(\frac{r}{\rho}\right)^{2n+1} \frac{n+1}{2n} I(\rho)\, d\rho\right],$$

in which all but the last two integrals are finite. Evaluating these

integrals and rearranging, one has

$$A + B + \frac{4I(r)}{r} \sum_{n=n^*}^{\infty} \frac{r^{4n+1} - a^{2n+1} b^{2n}}{2n \; r^{2n} \; b^{2n}} \; ,$$

where B represents the finite integrals in the preceding expression and the current density function assumes its value at $\rho = r$. The ratio test confirms the convergence of this series, for $a < r < b$.

The divergent behaviour of the individual kernels at $r = \rho$ imposes a restriction on the numerical method used to solve equation (3.16). When choosing a quadrature formula to approximate the integrals, one which does not attempt to evaluate the integrand at the end points must be used to avoid this singularity. For simplicity the mid-point rule has been chosen (Isaacson and Keller, 1966, p. 316) namely

$$\int_{x_0}^{x_n} f(x)\,dx = \sum_{j=1}^{n} L f\left(\frac{x_j + x_{j-1}}{2}\right) + (x_n - x_0)\frac{h^2}{3} f''(\xi) \; ,$$

$$(x_0 \leq \xi \leq x_n) \; ,$$

where the range $\left[x_1, x_n \right]$ has been divided into n equal subintervals each of length L.

The solution to equation (3.16) is obtained by splitting the entire range of integration $\left[a, b \right]$ into n equal subintervals with step length h, and considering the resulting equations for n different values of r ($r_j = a + jh$, $j = 0, 1, \ldots\ldots, n-1$). In this way a system of n linear algebraic equations for $I\left(\frac{r_i + r_{i+1}}{2}\right)$ are generated, that is,

$$h \sum_{i=0}^{s-1} K_1 \left(r_s , \frac{\rho_i + \rho_{i+1}}{2} \right) I \left(\frac{\rho_i + \rho_{i+1}}{2} \right)$$

$$+ h \sum_{i=s}^{n-1} K_2 \left(r_s \frac{\rho_i + \rho_{i+1}}{2} \right) I \left(\frac{\rho_i + \rho_{i+1}}{2} \right) = F(r_s) , \qquad (3.18)$$

$$(s = 0, 1, 2, \ldots\ldots, n-1) ,$$

where $r_s = a + sh$,

and $\rho_i = a + ih$.

The coefficients K_1 and K_2 in system (3.18) are calculated from their respective series expansions (equation 3.15). The problem

of the divergence of the series at $r = \rho$ may now be turned to an advantage to improve the numerical estimates of these infinite series as follows. From equations (3.17), the coefficients in the two series behave like

$$\frac{2}{\pi r}\left(\frac{\rho}{r}\right)^{2n} \qquad \text{and} \qquad \frac{2}{\pi r}\left(\frac{r}{\rho}\right)^{2n+1}$$

for sufficiently large values of n. Each series therefore behaves approximately like a geometrical progression after some large number of terms (n^*, say) has been taken, and may be summed numerically using, for example,

$$\sum_{n=1}^{\infty} a_n\left(\frac{r}{\rho}\right)^{2n} = \sum_{n=1}^{n^*-1} a_n\left(\frac{r}{\rho}\right) + \sum_{n=n^*}^{\infty} a_n\left(\frac{r}{\rho}\right)^{2n}$$

$$\simeq \sum_{n=1}^{n^*-1} a_n\left(\frac{r}{\rho}\right)^{2n} + a_{n^*}\frac{(r/\rho)^{2n^*}}{1-(r/\rho)^2} ,$$

where a_n is the general coefficient of the series.

Finally it is noted that the factor $(2n)!/((n!)^2\, 4^n)$ appearing in both kernels, may be more conveniently expressed as

$$\frac{(2n)!}{(n!)^2\, 4^n} = \prod_{m=1}^{n} \left(\frac{2m-1}{2m}\right) ,$$

for computing purposes. In this way, generation of the large numbers arising from the factorials is avoided, which reduces the possibility of a systematic round-off error.

In Figure 26, the current $I(r)$ is plotted as a function of r. The four plots represent the results obtained by choosing step lengths of 0.1, 0.05, 0.033 and 0.025 for a current sheet with inner and outer radii of 1 and 2 respectively (with $\alpha \equiv 1$; $D \equiv 1$). For $n \geqslant 20 (h \leqslant 0.05)$ the plots converge fairly well to illustrate the shape of the current density function.

The current density function $I(r)$ is markedly skewed towards the lower end of the range. A possible explanation for this fact is that the magnetic field lines will be closer together, and hence the field itself stronger, near the inner ends of the current sheet annulus. Hence, the induced currents may be stronger near the inner boundary of the annulus.

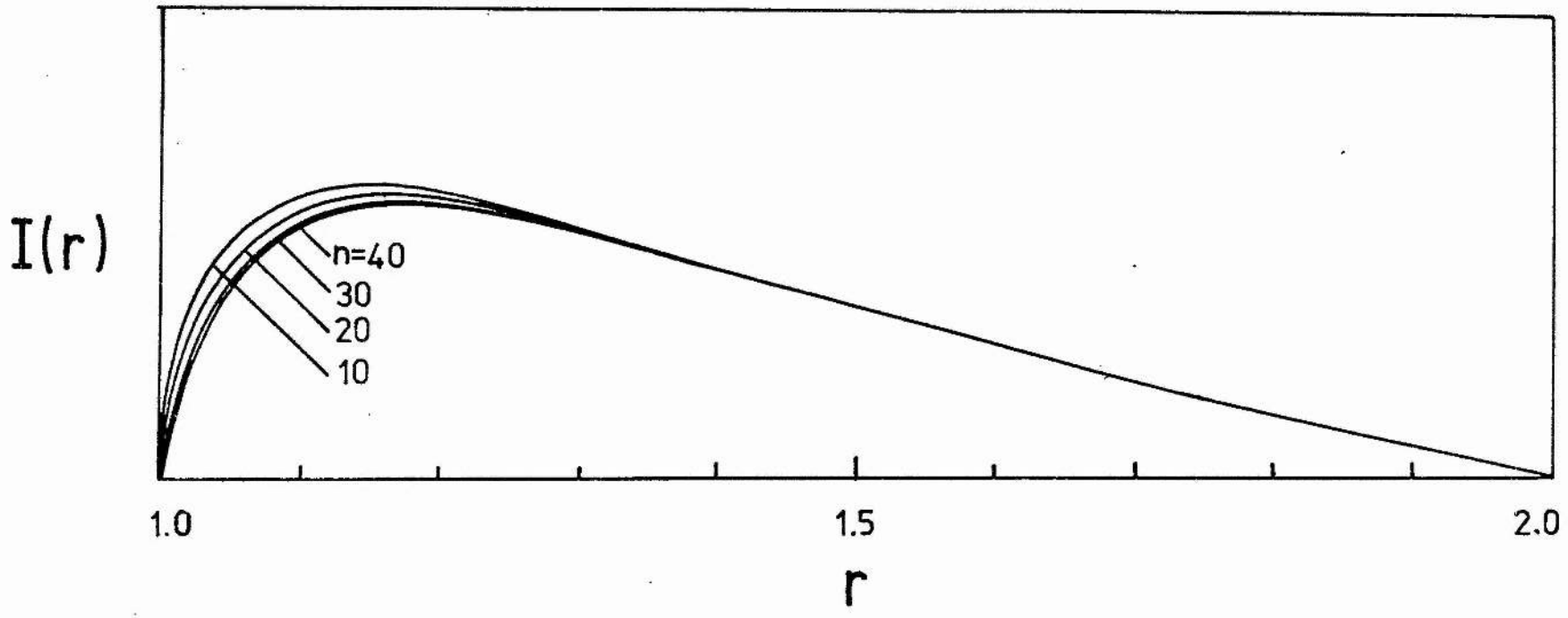

Figure 26.

The current density function I(r), plotted for D=1, a=1 and b=2 for illustration. The four plots correspond to the cases h=0.1, 0.05, 0.033 and 0.025 (n= 10, 20, 30, 40 respectively).

3.3 THE POSITION OF THE NEUTRAL SHEET, DETERMINED BY THE FLUX CONDITIONS.

Following the analogous two-dimensional model, the condition that the field be frozen-in may be applied to the problem to determine the inner and outer radii of the current sheet as the dipoles converge. That is, we wish to determine $a(\alpha)$ and $b(\alpha)$.

For the three-dimensional case, the relevant condition is that the flux

$$F = \iint_S \left(\hat{\underline{n}} \cdot \underline{B}\right)_s \, dS \quad , \tag{3.19}$$

across a surface s must be conserved under the transformation from the initial to the final state. For the axisymmetric configuration considered here, this becomes equal to the line integral

$$F = 2\pi \int_{r_0}^{r_1} \left(\hat{\underline{n}} \cdot \underline{B}\right)_T \, r\,dr$$

where the integrand is just r times the normal component of the field $\underline{B}$ along a radius vector T .

The first flux condition (as in the two-dimensional cases) is obtained from the requirement that the flux crossing the entire $\Theta = \pi/2$ plane remains constant. Initially the flux F_0 is given by

$$F_o = 2\pi \int_0^\infty \frac{2D(r^2 - 2\alpha_o^2)\, r\,dr}{(\alpha_o^2 + r^2)^{5/2}}$$

$$= 2\pi D \int_0^\infty \frac{(u - 2\alpha_o^2)\, du}{(\alpha_o^2 + u)^{5/2}} \qquad (3.20)$$

$$= 0 \quad ,$$

with a suitable substitution α_0 is the initial dipole separation. This result is to be expected from the physical considerations outlined in section 2.2.

After the deformation to form the field bearing the current sheet, the flux that threads the $\Theta = \pi/2$ plane may be written

$$F = 2\pi \int_0^\infty \left(\frac{\partial \Phi}{\partial n}\right) r\,dr$$

Using equation (3.9) for Φ_S and (3.11) for Φ_D ($\Phi = \Phi_S + \Phi_D$) and noting that the contribution to the integral between a and b must

be zero, this becomes

$$F = -4\pi^2 \int_{r=0}^{a} \int_{\rho=a}^{b} \sum_{n=0}^{\infty} (-1)^n \frac{(2n)!}{(n!)^2 4^n} \left(\frac{r}{\rho}\right)^{2n+1} P_{2n}(0) \frac{(2n+1) I(\rho, a, b)}{r} d\rho \cdot r dr$$

$$+ 4\pi^2 \int_{r=b}^{\infty} \int_{\rho=a}^{b} \sum_{n=1}^{\infty} (-1)^n \frac{(2n)!}{(n!)^2 4^n} \left(\frac{r}{\rho}\right)^{2n} P_{2n-2}(0) \frac{(2n-1) I(\rho, a, b)}{r^2} d\rho \cdot r dr$$

$$- 4\pi \left[\frac{b^2}{(b^2+\alpha^2)^{3/2}} - \frac{a^2}{(a^2+\alpha^2)^{3/2}} \right] D ,$$

in which the current density function I must be regarded as a function of the end points a and b of the sheet, as well as r. Hence, reversing the order of integration, further manipulation yields

$$F = 4\pi^2 \int_{a}^{b} \sum_{n=0}^{\infty} \left[\frac{(2n)!}{(n!)^2 4^n} \right]^2 \left\{ \frac{2n \rho^{2n}}{(2n-1) b^{2n-1}} - \frac{(2n+1) a^{2n+2}}{(2n+2) \rho^{2n+1}} \right\} I(\rho, a, b) d\rho$$

$$+ 4\pi D \left[\frac{b^2}{(b^2+\alpha^2)^{3/2}} - \frac{a^2}{(a^2+\alpha^2)^{3/2}} \right] ,$$

which, after equating to F_0 given by equation (3.20), gives one relationship between a and b, namely

$$\pi \int_a^b \sum_{n=0}^{\infty} \left[\frac{(2n)!}{(n!)^2 4^n}\right]^2 \left\{\frac{2n\rho^{2n}}{(2n-1)b^{2n-1}} - \frac{(2n+1)a^{2n+2}}{2n+2\ \rho^{2n+1}}\right\} I(\rho,a,b)\, d\rho \qquad (3.21)$$

$$+ D\left[\frac{b^2}{(b^2+\alpha^2)^{3/2}} - \frac{a^2}{(a^2+\alpha^2)^{3/2}}\right] = 0$$

A second condition may be derived by demanding that the flux through the circle bounded by the neutral line in the first instance is equal to that crossing the corresponding disc $r \leqslant a$ in the final situation. That is,

$$\int_{r=0}^{\sqrt{2}\alpha_0} \left[\frac{\partial\Phi}{\partial n}\right]_{\Theta=\pi/2} r\,dr = \int_{r=0}^{a} \left[\frac{\partial\Phi}{\partial n}\right]_{\Theta=\pi/2} r\,dr$$

which, after using equations (3.9) and (3.12), becomes

$$\frac{2D}{3^{3/2}\alpha_0} = \frac{Da^2}{(a^2+\alpha^2)^{3/2}} + \pi \int_a^b \sum_{n=0}^{\infty} \left[\frac{2n!}{(n!)^2 4^n}\right]^2 \frac{a^{2n+2}}{\rho^{2n+1}} \left(\frac{2n+1}{2n+2}\right) I(\rho,a,b)\, d\rho .$$

(3.22)

Equations (3.21) and (3.22) thus determine the end points a and b. A method for their numerical solution is outlined in the next section.

3.4 NUMERICAL SOLUTION OF FLUX CONDITIONS.

In order to obtain the inner and outer radii, $a(\alpha)$ and $b(\alpha)$ respectively, equations (3.21) and (3.22) must be solved numerically.

Firstly, if equations (3.21) and (3.22) are added, one obtains

$$\frac{2D}{3^{3/2}\alpha_0} = \frac{Db^2}{(b^2+\alpha^2)^{3/2}} + \pi \int_a^b \sum_{n=0}^{\infty} \left[\frac{(2n)!}{(n!)^2 4^n}\right] \frac{2n}{2n-1} \frac{\rho^{2n}}{b^{2n-1}} I(\rho,a,b)\, d\rho ,$$

(3.23)

This is precisely the flux condition one would obtain on equating the flux outside the circle $r = \alpha_0$ with its counterpart $r = b$ in the final configuration. Equation (3.23) is slightly more suitable for computation than equation (3.21) in that it contains a much shorter integrand, therefore reducing both the time involved in solving the

system and also the round-off errors.

The system of equations (3.22) and (3.23) may be expressed in the functional form

$$\underline{a} = \underline{g}(a) \quad , \quad \underline{a} = \left[a, b \right]^{tr} \tag{3.24}$$

suggesting the iterative scheme

$$\underline{a}^{(i+1)} = \underline{g}(\underline{a}^{(i)}), \quad i = 0, 1, 2.... \tag{3.25}$$

The vector function $\underline{g}$ should be chosen such that the sequence $\left\{ a^{(i)} \right\}$, generated by equation (3.25), converges to the solution vector. However, to test the convergence of a particular scheme analytically would be extremely difficult here as the partial derivatives of $\underline{g}(\underline{a})$ with respect to $\underline{a}$ are required (see, for example, Isaacson and Keller, 1966, p. 106). Instead one must resort to "trial and error" techniques for choosing $\underline{g}$.

The iterative process for solving the above system of equations is further complicated by the fact that we have effectively (n + 2) equations (not two) to solve simultaneously, n equations arising from system (3.18) for the current I(r). At each step of the solution of system (3.25) as new values of a and b are generated, the current density function, I(r,a,b) must be updated using the methods outlined in section (3.3). The full procedure is most conveniently illustrated by means of a flow chart (Figure 27).

The simplest choice for the iterating vector $\underline{g}$ that produced a convergent sequence was

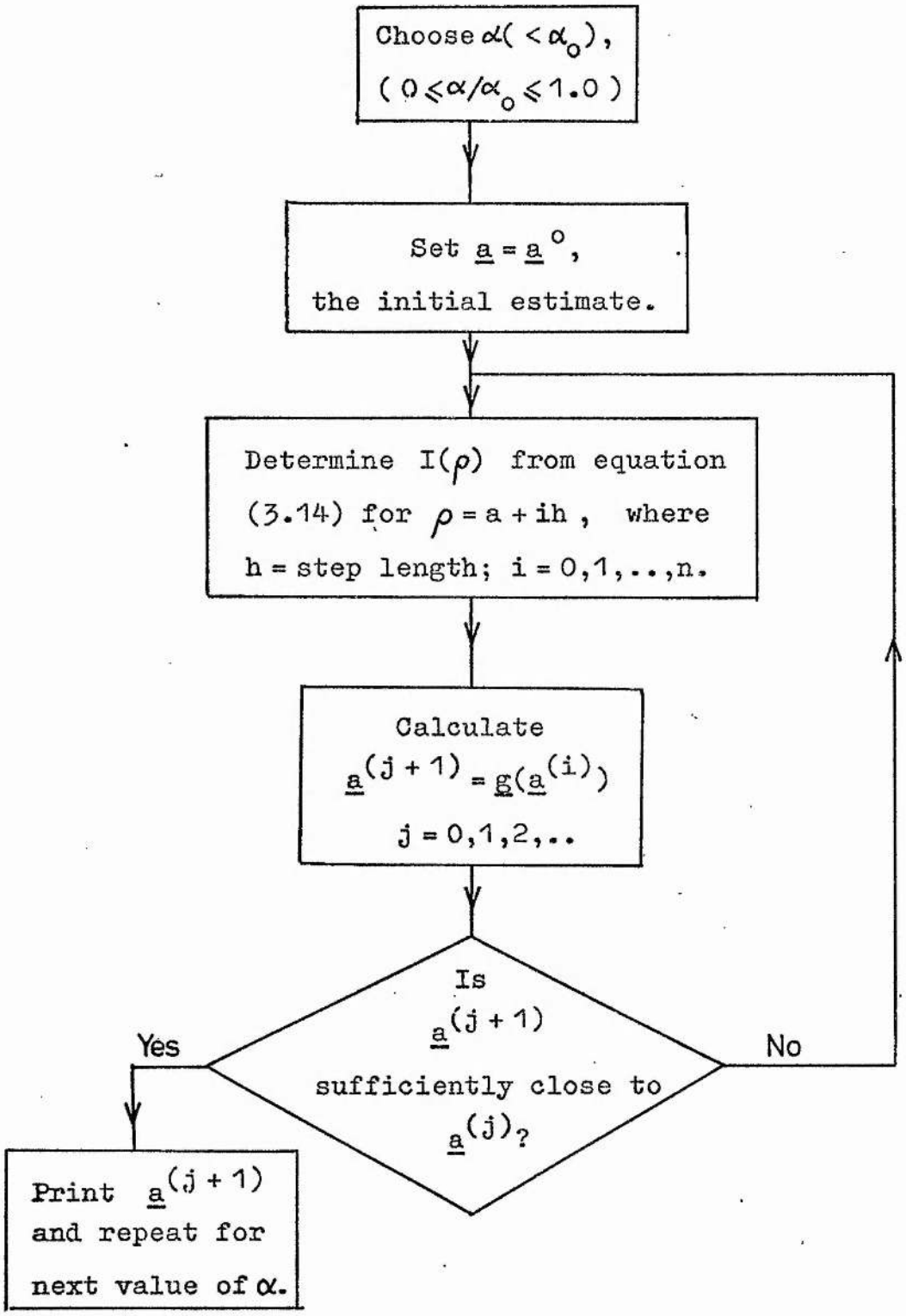

Figure 27

Flow diagram for the numerical solution of system (3.24).

$$a = (a^2+\alpha^2)^{3/2}\left[\frac{2}{3^{3/2}} - \pi\int_a^b\sum_{n=0}^{\infty}\left[\frac{(2n)!}{(n!)^2 4^n}\right]\frac{a^{2n+2}}{\rho^{2n+1}}\left(\frac{2n+1}{2n+2}\right)I(\rho,a,b)\,d\rho\right] \Big/ a$$

$$b = \left\{\left[b^2\Big/\left(\frac{2}{3^{3/2}} - \pi\int_a^b\sum_{n=0}^{\infty}\left[\frac{(2n)!}{(n!)^2 4^n}\right]\left(\frac{2n}{2n-1}\right)\frac{\rho^{2n}}{b^{2n-1}}\,I(\rho,a,b)\,d\rho\right)\right]^{2/3} - \alpha^2\right\}^{1/2}$$

Figure 28 shows the results of the numerical solution of system (3.24) for values of n ranging between 10 and 60. The lower branch is well defined for all n , but the outer limit of the current sheet is more difficult to determine with the equations only converging at all values of α/α_0 when n = 60. The wide discrepancy in the results for $b(\alpha)$ may be due to one or more of several inadequacies of the numerical techniques used. These shortcomings include: the truncation of infinite series after a large number of terms; the choice of an iterative scheme which, although convergent, may be a relatively slow one, and the use of a rather simple quadrature formula. The limitations were imposed by the time and core restrictions of the computer programme being used. Further work is being carried out to improve the numerical methods used for this problem.

These three-dimensional results indicate a somewhat larger current sheet than did the two-dimensional analysis. Also, no simple relationship between the end points (a and b) and the dipole separation (α/α_0) was found, unlike the inverse points for the ends of the two-dimensional sheet.

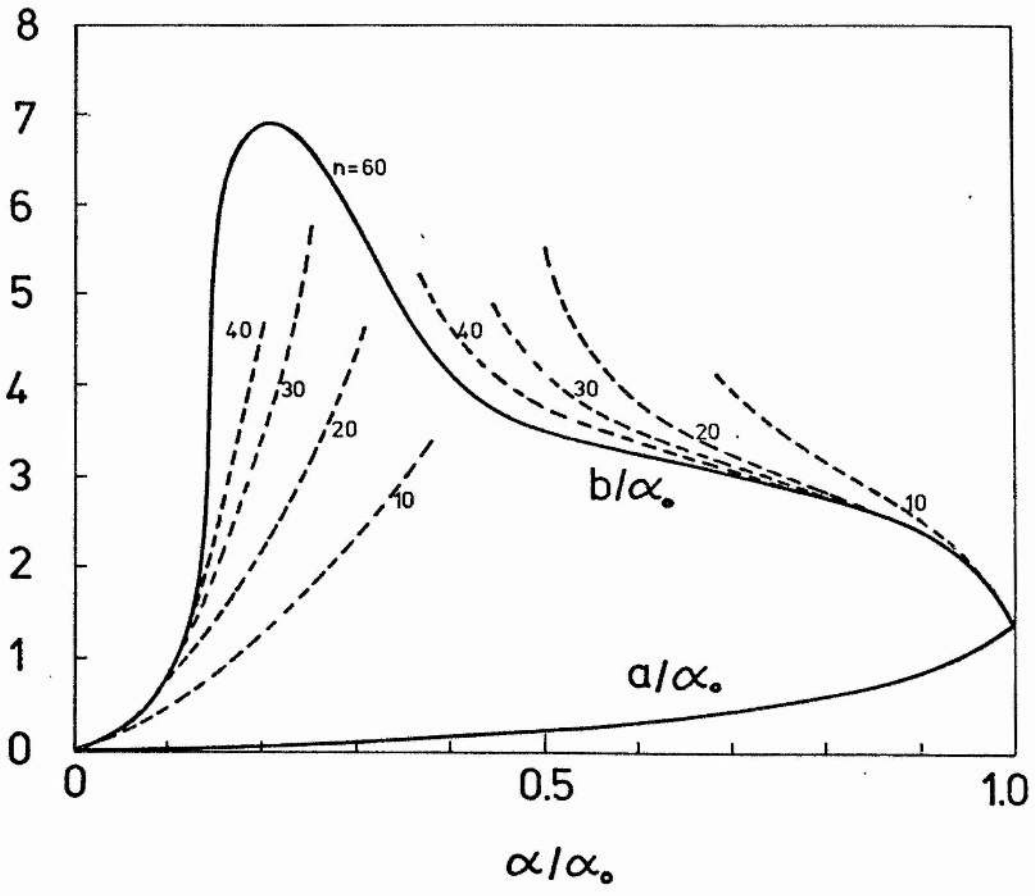

Figure 28.

The loci of the end points (a and b) of the current sheet as α/α_0 decreases. The iterative scheme did not converge for all values of α/α_0 until 60 subdivisions of the range of integration (a,b) were used (solid line). As n increases, the solution curves for $b(\alpha)$ get progressively closer.

In Figure 29 the loci of the end points are shown (for n = 60) with the current density function superimposed for several values of α/α_0.

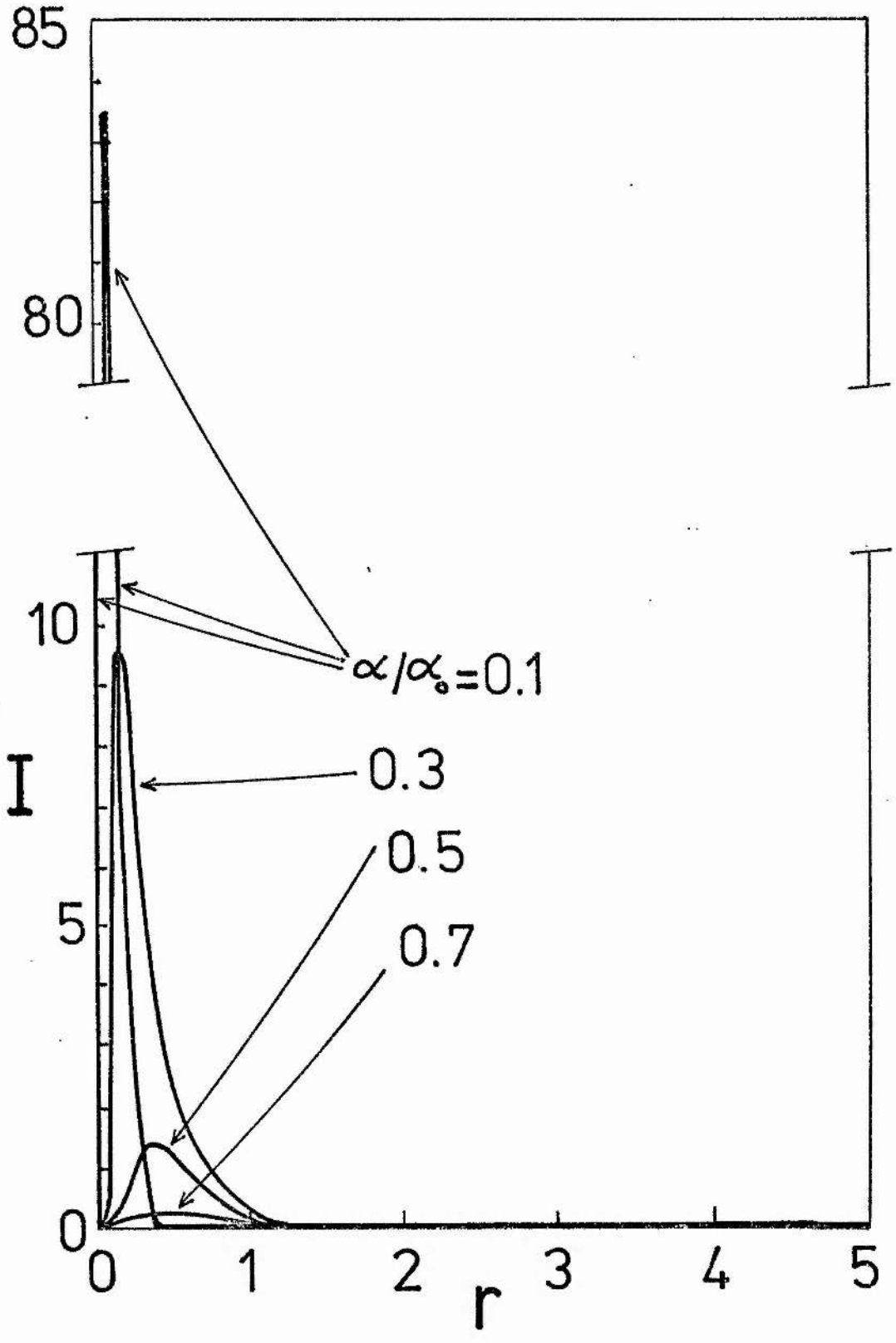

Figure 29.

The current density function I (r,a,b). Each plot corresponds to a particular value of the α/α_0 between 0.1 and 0.7. (60 subdivisions of the range of integration).

CHAPTER 4.

A TRIGGER MECHANISM FOR THE EMERGING FLUX MODEL OF SOLAR FLARES.

In this chapter, a possible trigger mechanism for solar flares is presented, extending the work of Heyvaerts and Priest (1976), outlined in the first chapter, and the emerging flux model for flares (Heyvaerts et al., 1976).

The emerging flux model is based on observations of flare activity associated with new magnetic flux emerging from below the photosphere. It is suggested (Heyvaerts et al., 1976) that many flares occur in three stages as loops of magnetic flux rise in the solar atmosphere. Firstly, a current sheet forms between the new and old magnetic flux, allowing continuous reconnection above a certain height. They equate this stage with the preflare heating phase characterised by the production of soft X-ray emission. At a critical height, thermal equilibrium becomes no longer possible, and the sheet heats up, rapidly seeking a new equilibrium state. During this stage, the current density exceeds the threshold for the onset of microinstabilities and the impulsive phase takes place. Eventually a new equilibrium state, the main phase of the flare, is reached in which steady reconnection can take place with a turbulent current sheet.

These qualitative ideas suggest that the thermal equilibrium of a current sheet rising in the solar atmosphere be investigated in more detail.

In Chapter 2 it was suggested that the solar atmosphere could

be divided into three regimes.

(i) Very low down where the velocity of emerging flux (v) is greater than or roughly equal to the local Alfvén speed (v_A).

(ii) Intermediate heights, typically the low chromosphere, where $v_{max} < v < v_A$, v_{max} being the maximum reconnection speed. Here a current sheet may form without significant reconnection.

(iii) Higher up, $v < v_{max}$ and the emerging flux reconnects with the overlying field

Heyvaerts and Priest (1976) considered only the third region in which reconnection between new and old flux could occur. In section 4.1 the energy balance in the current sheet is considered for the intermediate region where no reconnection occurs, while section 4.2 deals with the same equation, modified to allow for reconnection. Figures 31 (a) and 31 (b) show the heights above which $v_\infty < v_{max}$ and $v_\infty < v_A$ respectively, based on the model atmosphere given in Table 4.

4.1 THE TRIGGER MECHANISM (NON-RECONNECTING REGION).

The thermal instability of a current sheet, investigated by Heyvaerts and Priest (1976) was reviewed briefly in section 1.3 (c). The basic equation, a statement of the energy balance inside a current sheet, is repeated here for convenience. It is,

$$E = J + H + K - R \,, \tag{4.1}$$

where E represents the convective transfer of heat through the sheet, J, H and K represent the joule heating, mechanical heating and thermal

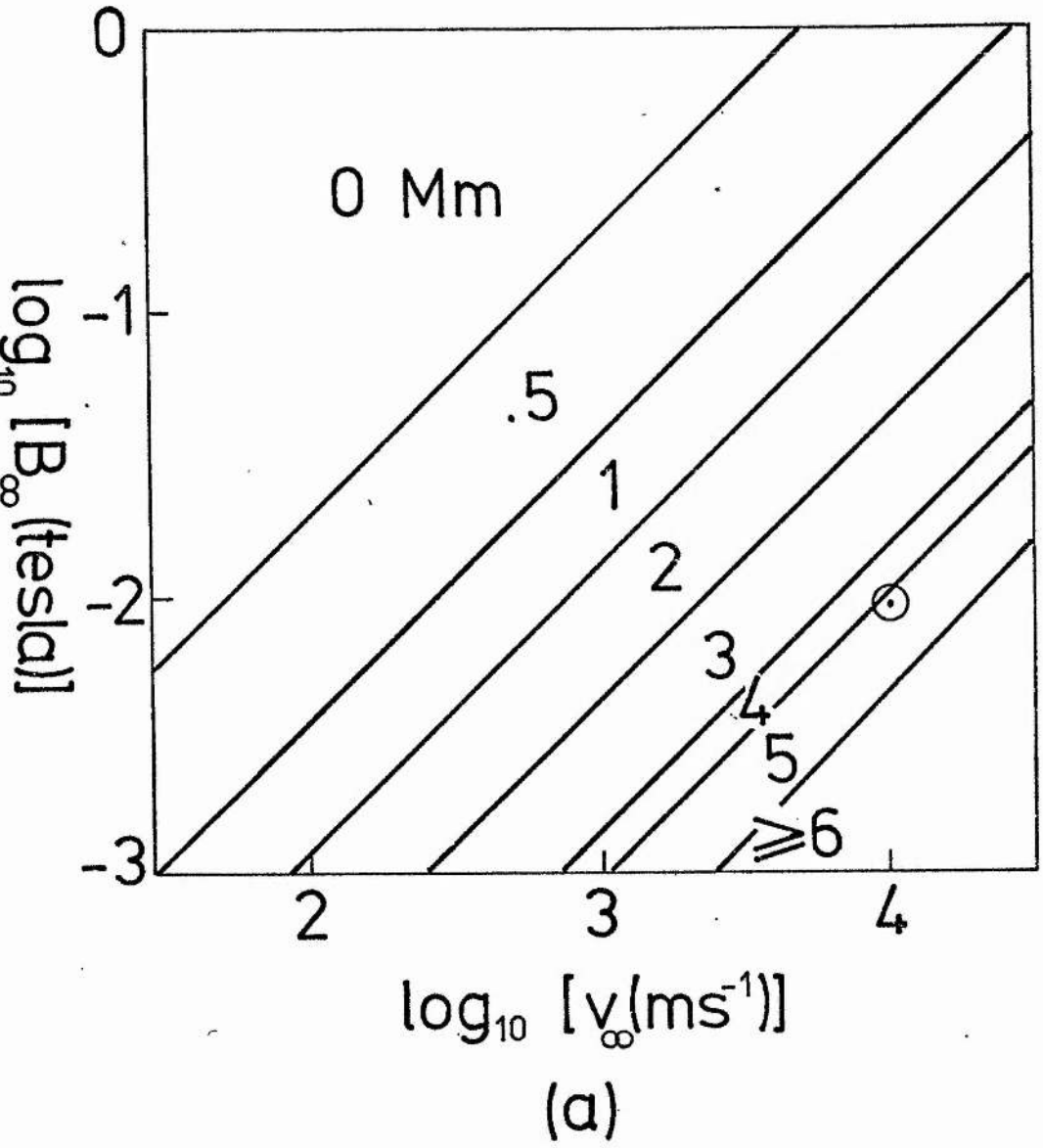

Figure 31.

The heights above which (a) $v_{\infty} < v_{max} = v_A/40$, and (b) (overleaf) $v_{\infty} < v_A$, as B_{∞} and v_{∞} vary, using the model atmosphere (Table 4). For example, with a field of 10^{-2} tesla and a speed of $10^4 ms^{-1}$ for the emerging flux (marked thus ⊙), $v_{max} < v_{\infty} < v_A$ above 0.5Mm and $v_{\infty} < v_{max}$ above 5Mm. That is to say, between 0.5Mm and 5Mm the sheet is in the regime in which no significant reconnection occurs, but above 5Mm, steady reconnection may occur.

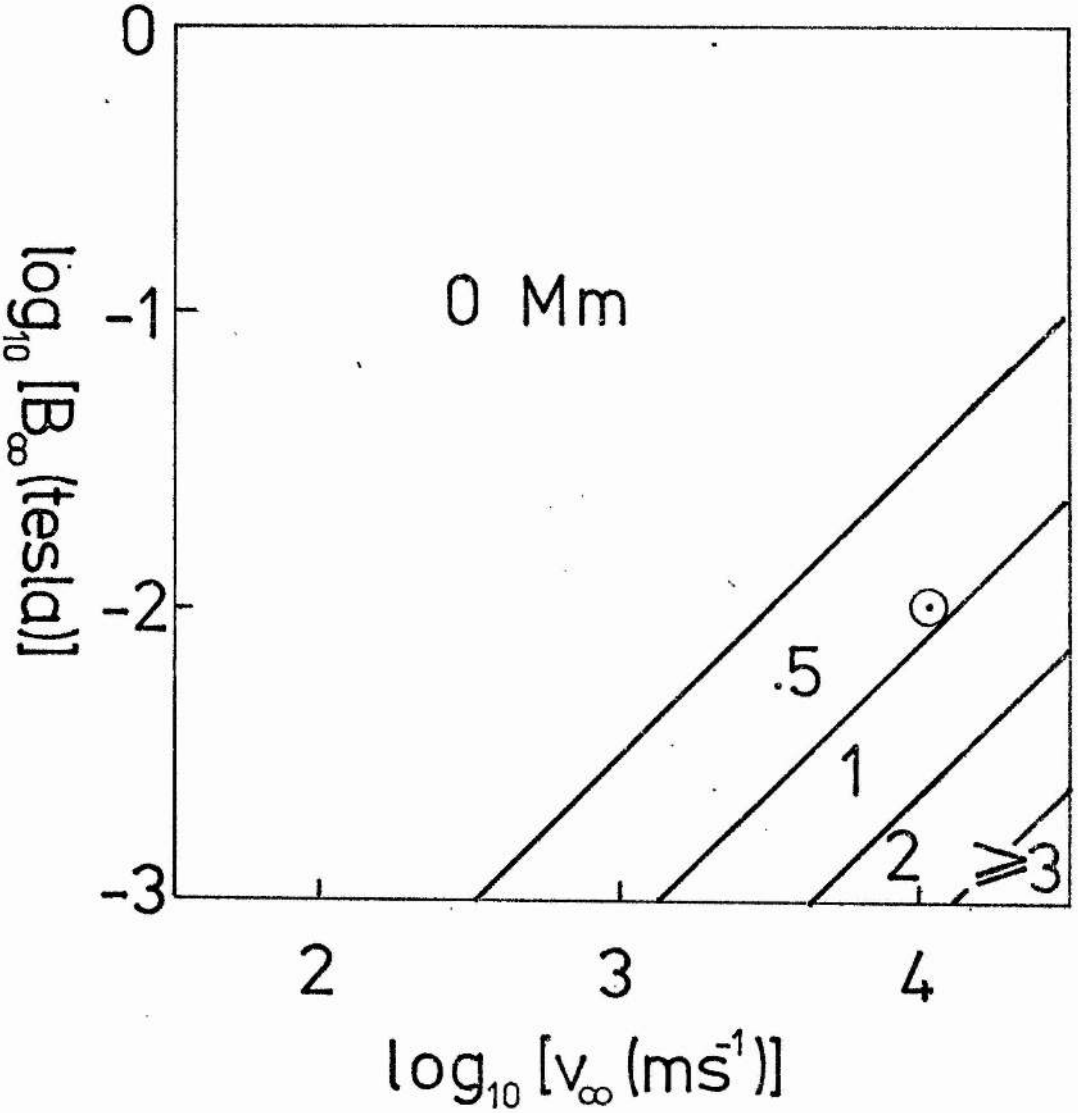

(b)

conduction respectively, and R denotes radiative loss. Each term may be written in terms of the parameters pertaining to the conditions inside the sheet (subscript c) and the ambient plasma (subscript ∞). If each term is exactly represented, equation (4.1) becomes a non-linear partial differential equation.

Fortunately, a full analytic or numerical solution may be avoided by approximating each term and solving the resulting algebraic equation for the temperature, T_c , inside the sheet. It will be seen that, as the height (h) of the current sheet in the solar atmosphere and its internal temperature vary, one or other of the terms in equation (4.1) becomes dominant. The terms which dominate vary throughout the (T_c, h) plane. Along the solution curve of equation (4.1), two or more of the terms dominate and balance each other.

The term by term approximation of equation (4.1) is set out below, indicating where the analysis of Heyvaerts and Priest has been improved.

The convective term E is exactly,

$$\frac{p^{\gamma}}{\gamma - 1} \quad \frac{D}{Dt}\left(\frac{p}{\rho^{\gamma}}\right) \quad , \tag{4.2}$$

(Boyd and Sanderson, 1969, p. 55), where p, T, ρ and γ are the gas pressure, temperature, density and adiabatic index (γ = 5/3 for a

monatomic gas), respectively. In this thesis a more accurate approximation than that of Heyvaerts and Priest is chosen for this term. After using the perfect gas law (1.3) for ρ, expression (4.2) may be alternatively written

$$\frac{\gamma}{\gamma-1}\,\frac{p}{T}\,\frac{DT}{Dt} - \frac{Dp}{Dt} \quad .$$

The convective derivative D/Dt reduces to $\underline{v}\cdot\nabla$, which in turn is approximated by

$$\underline{V}\cdot\underline{\nabla} \simeq \frac{V_\infty}{l} + \frac{V_{out}}{L} \quad ,$$

where l and L represent the width and length of the current sheet, and v_∞ and v_{out} are the ambient inflow and outflow velocities respectively (see Figure 30). However from continuity of mass,

$$\frac{V_\infty / l}{V_{out}/L} \simeq \frac{\rho_c}{\rho_\infty} \gg 1 \, ,$$

and so D/Dt is finally approximated by just v_∞ / l. The length L is determined by the model presented in section (2.4), where the current sheet formed above an emerging bipolar region is simulated. The width l is less easy to approximate. In Chapter 2 current sheets were studied in an idealized situation and were assumed to have negligible width. For the present theory, the width will be

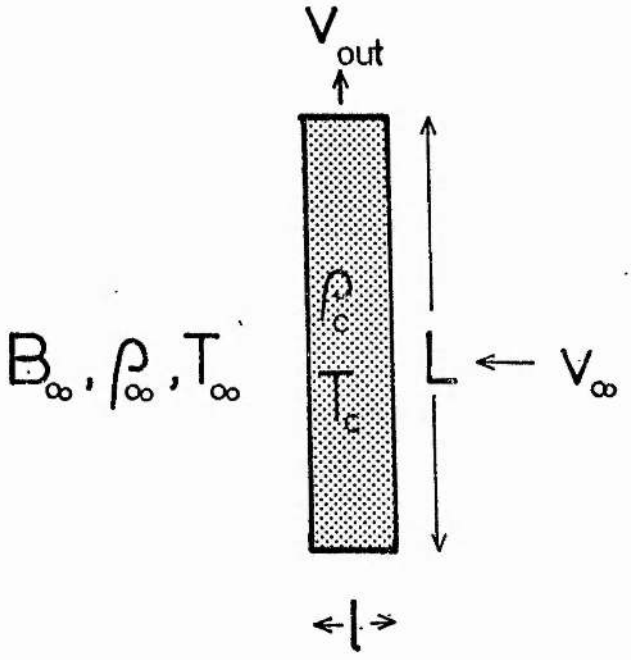

Figure 30.

Schematic representation of the current sheet illustrating some of the parameters used in the problem.

taken as

$$l = \frac{\eta}{v_{max}} \quad , \tag{4.3}$$

although this is only a lower bound for this parameter, obtained by taking the largest inflow velocity and magnetic Reynolds' number of order unity. The left hand side of equation (4.1) may therefore be written as

$$\frac{V_\infty}{l} \quad \frac{B_\infty^2}{2\mu} \left[\frac{\gamma}{\gamma-1} (1+\beta_\infty)\left(1-\frac{T_\infty}{T_c}\right) - 1 \right] \tag{4.4}$$

Here

$$\beta_\infty = \frac{p_\infty}{(B_\infty^2/2\mu)} \tag{4.5}$$

is the ratio of the hydrostatic and magnetic pressures outside the sheet, while B_∞/μ. is the strength of the ambient magnetic field. The balance between the gas pressure inside the sheet (p_c) and the total pressure (hydrostatic plus magnetic) outside,

$$p_c = p_\infty + \frac{B_\infty^2}{2\mu} \quad , \tag{4.6}$$

has been assumed in deriving expression (4.4).

The above approximation to E describes only the advection of thermal energy into the sheet, and is therefore suitable when discussing reconnecting or non-reconnecting current sheets.

The joule heating term (J) is generally approximated by

$$J = \frac{B_\infty^2}{(\mu^2 l^2 \sigma)} \quad (\text{Watt m}^{-3}) \tag{4.7}$$

where the conductivity σ is taken to be

$$\sigma(T_c) = 10^{-3} T_c^{3/2} \quad (\text{mho m}^{-1}) \tag{4.8}$$

from Spitzer (1962; p. 139).

The radiative cooling term R is taken as

$$R = n_c^2 Q(T_c) \quad (\text{Watt m}^{-3}) \tag{4.9}$$

where Q(T) is the radiative cooling function given, for example, by Hildner (1974), and is set out in Table 3 below. For the plasma density inside the sheet, the approximation

$$n_c \simeq n_\infty \left(1 + \frac{1}{\beta_\infty}\right) \frac{T_\infty}{T_c} \quad , \tag{4.10}$$

derived from equation (4.6) and the perfect gas law, is taken.

It is assumed that there is a balance between the radiative cooling

of the plasma outside the sheet and the mechanical heating (H) inside. If, furthermore one assumes that H is linearly dependent upon the internal density n_c ,

$$H = h\, n_c ,$$

say, for some constant h , then the mechanical heating term may be approximated by

$$H = n_c\, n_\infty \quad Q(T_\infty) \text{ (Watt } m^{-3}) \quad . \tag{4.11}$$

TABLE 3.

The radiative cooling function $Q(T) = \chi_i T^{\alpha i}$, after Hildner (1974).

Temperature	i	χ_i	α_i
$T \geq 8 \times 10^5$K	1	5.51×10^{-30}	- 1.0
8×10^5K $> T \geq 3 \times 10^5$K	2	3.94×10^{-21}	- 2.5
3×10^5K $> T \geq 8 \times 10^4$K	3	8.00×10^{-35}	0
8×10^4K $> T \geq 1.5 \times 10^4$K	4	1.20×10^{-43}	+ 1.8
1.5×10^4K $> T$.	5	4.92×10^{-67}	+ 7.4

The thermal conductive heating

$$K = \nabla \cdot (\underline{\underline{\kappa}}\, \nabla\, T),$$

may be split into two parts that describe the conduction along and perpendicular to the magnetic field lines. K then approximates to

$$\kappa_{\parallel} (T_\infty - T_c)/L^2 + \kappa_{\perp} (T_\infty - T_c)/l^2 \quad (\text{Watt } m^{-3}), \tag{4.12}$$

where the coefficients of thermal conduction are given by

$$K_{\parallel} = 10^{-11}\ T_c^{5/2} \quad \text{(Watt m}^{-1}\text{ deg}^{-1}\text{)}, \tag{4.13}$$

and

$$K_{\perp} = 2 \times 10^{-31}\ n_c^{2}\ T_c^{-3}\ B_{\infty}^{-2}\ K_{\parallel} \quad \text{(Watt m}^{-1}\text{deg}^{-1}\text{)} \tag{4.14}$$

Taking $n_c = 10^{18}$ m^{-3}, $T_c = 10^5$ deg. and $B_\infty = 10^{-2}$ tesla for the sake of illustration, one sees that the conduction coefficient along the magnetic field lines is some 2×10^6 times greater than that across the field. Even so, the larger area presented by the sides of the current sheet (compared with its ends) may significantly increase the total amount of heat conducted across the field lines. For example, using the above figures for n_c, T_c and B_∞, the perpendicular and parallel coefficients would be roughly equal for l/L equal to 10^{-3} not an unrealistic value.

TABLE 4.

Temperature (T_∞) and number density (n_∞) for a model solar atmosphere (from Heyvaerts and Priest, 1976)

Height $h(m)/10^6$	T_∞ ^0K	n_∞ (m^{-3})
0.0	4.4×10^3	7.94×10^{21}
0.5	4.9×10^3	3.16×10^{20}
1	5.2×10^3	3.98×10^{19}
2	5.8×10^3	3.98×10^{18}
3	6.3×10^3	3.98×10^{17}
4	7.4×10^3	2.00×10^{17}
5	1.3×10^4	5.00×10^{16}
6	3.0×10^4	1.58×10^{16}
7	5.5×10^4	6.31×10^{15}
8	1.6×10^5	2.51×10^{15}
9	3.0×10^5	1.41×10^{15}
10	4.0×10^5	7.94×10^{14}
11	4.9×10^5	6.30×10^{14}
12	5.7×10^5	5.00×10^{14}
13	6.9×10^5	4.00×10^{14}
14	8.5×10^5	3.16×10^{14}
15	1.0×10^6	3.16×10^{14}
16	1.2×10^6	3.16×10^{14}

Heyvaerts and Priest did not include the effects of conduction across the field lines since they expected it to be unimportant. However, when ℓ / L becomes small enough, the effects of transverse

conduction become important and in practice may sometimes dominate in equation (4.1).

Taking the diffusivity η to be $8 \times 10^{8} T_c^{-3/2}$ $(m^2 s^{-1})$, equation (4.1) may be solved for the internal temperature of the sheet T_c for any given set of parameters T_∞, B_∞ v_∞ and n_∞ for the surrounding atmosphere. A model solar atmosphere (Table 4) relating n_∞ and T_∞ to height h is chosen, and T_c plotted as a function of h.

4.2. THE RECONNECTING REGION.

When the velocity of the emerging flux is less than the maximum reconnection speed, steady reconnection may occur at the sheet. This situation used by Heyvaerts and Priest when setting up their analysis, causes one or two alterations to be made to the energy equation (4.1).

The joule heating term, given by equation (4.7) may be simplified in view of the fact that the magnetic Reynold's number

$$R_m = l\, v_\infty \mu \sigma$$

is of order unity. J therefore becomes

$$J = \sigma v_\infty^2 B_\infty^2 \quad (\text{watt } m^{-3}) \qquad (4.15)$$

The width of the current sheet may now be taken to be

$$l \simeq \eta / v_\infty \quad , \qquad (4.16).$$

with $R_m \simeq O(1)$, and the length is therefore given by mass continuity as

$$L \simeq l \frac{(V_{out})}{(V_\infty)} \frac{\rho_c}{\rho_\infty} , \qquad (4.17)$$

Here, v_{out} is the outflow speed from the reconnection region, and is given by the Alfvén speed based on the density of the plasma being ejected, ρ_c. Thus

$$v_{out} = \frac{B_\infty}{\sqrt{\mu \rho_c}} \qquad (4.18)$$

Heyvaerts and Priest took v_{out} to be the Alfvén speed based on the ambient density, and therefore their estimate for the length of the sheet was a factor $(n_c/n_\infty)^{\frac{1}{2}}$ larger than the present value.

With l and L being modified, the remaining terms in equation (4.1) will take the same form as for the non-reconnecting region.

As B_∞ and v_∞ vary, so does the form of the solution of the energy equation. Several examples are shown in section (4.5) In addition a somewhat more realistic case is investigated in which the magnetic field B_∞ decreases with height, from a typical value for the low, active chromosphere (10^{-1} tesla) to 10^{-3} tesla in the corona.

4.3. CURRENT SHEET WIDTH LIMITATIONS.

The width (ℓ) of the current sheet given by equation (4.16) is based upon a fluid description of the plasma and is therefore invalid below some small length scale λ , say. Strictly speaking, when λ is of the order of a mean free path, the fluid equations should be abandoned in favour of a collisionless description. The mean free path for thermal electrons or ions is

$$\lambda = 3 \times 10^{7} \frac{T_c^{2}}{n_c} \quad (m) \qquad (4.19)$$

whereas the width of the current sheet is,

$$\ell = 8 \times 10^{8} / (T_c^{3/2} v_\infty), \qquad (4.20)$$

having used equation (4.16) with

$$\eta = 8 \times 10^{8} T_c^{-3/2}$$

The condition that ℓ is greater than λ is therefore given by

$$T_c^{9/2} < 7.7 \times 10^{29} \frac{B_\infty^{2}}{v_\infty} , \qquad (4.21)$$

having substituted for n_c from equations (4.5) and (4.10) with $\beta_\infty \ll 1$. This condition is a severe one. For $B_\infty = 0.01$ tesla and $v_\infty = 10^{3}$ ms^{-1} , ℓ is less than λ for internal temperatures greater than 1.2×10^{5} °K .

Vasyliunas (1975) claims that equation (4.16) remains valid

even when λ falls below the mean free path, provided that it does not become so small as to fall below the electron inertial length

$$\lambda_e = \left[\frac{m_e}{\mu_0 n_c e^2} \right]^{1/2} \quad (m) \qquad (4.22)$$

where m_e and e are just the electron mass and charge respectively. Accordingly he writes the width of the current sheet as

$$l = \frac{\eta}{2v_\infty} + \left(\frac{\eta^2}{4v_\infty^2} + \lambda_e^2 \right)^{1/2} . \qquad (4.23)$$

Clearly for $\eta / v_\infty \gg \lambda_e$, the above equation reduces to the form (4.16), while, at the other extreme, l tends asymptotically to λ_e. Comparing equations (4.20) and (4.22), the width of the sheet will be determined by η / v_∞ or λ_e depending whether T_e, defined by

$$T_e = 1.67 \times 10^8 \left(\frac{B_\infty}{v_\infty} \right)^{1/2} , \qquad (4.24)$$

is much greater than or less than T_c, respectively. So for example with $B_\infty = 10^{-2}$ tesla and $v_\infty = 10^2$ ms^{-1}, the current sheet width will be λ_e for temperatures much greater than 1.7×10^6 deg.

For T_c of the same order of magnitude as T_e, the full equation (4.23) must be used for ℓ.

The electron inertial length λ_e is not universally accepted as being the minimum sheet width. Sonnerup (1973), for example, maintains that the half-width of the sheet must be limited by the ion gyroradius

$$R_i \simeq 1.34 \times 10^{-6} \; T_c^{\frac{1}{2}} / B_\infty \quad (m) \qquad (4.25)$$

in view of simple considerations of the particle orbits in the current sheet. This leads to a lower critical current sheet temperature

$$T_{Ri} \simeq 2.45 \times 10^{7} \left(\frac{B_\infty}{v_\infty} \right)^{\frac{1}{2}} .$$

Vasyliunas (1975), in the appendix to his paper, disputes the ion gyroradius limit and demonstrates that only the shorter length scales λ_e or R_e (the electron gyroradius) are suitable candidates for the minimum current sheet widths.

In the examples of the temperature dependence on height shown in section (4.5), the width of the sheet has been taken as being described by equation (4.23). However, the graphs (Figures 34 and 35) depicting the general trends as B_∞ and v_∞ vary has been repeated for the three cases: (a) with no width limit, (b) for $\ell \gg \lambda_e$ and (c) for $\ell \gg R_i$.

Having chosen an alternative expression for the current sheet width (equation (4.23) instead of equation (4.20)), one must find how

the maximum reconnection speed v_{max} is affected.

To accomplish this the latest reconnection model, due to Soward and Priest (1976), is reinvestigated as follows.

The governing equations: (1.43), (1.44), (1.45), (1.48), (1 49) and (1.51) are given in section (1.3B). Among these, the first must be replaced by

$$\lambda = \lambda_e \tag{4.26}$$

where $T_c \gg T_e$. Eliminating all the unknowns except the Alfvén-Mach number M_i for the inflow speed, equation (1.52)

$$\frac{\pi}{8M_e} = \frac{\pi}{8M_i} + \frac{1}{2} \log_e (R_{me}^2 M_i M_e) ,$$

is then replaced by

$$\frac{\pi}{8M_e} = \frac{\pi}{8M_i} - \log_e \frac{\lambda_e}{L_e} \tag{4.27}$$

This new equation for M_e and M_i does not depend explicitly on R_{me}. Also, m_e no longer takes a maximum at $M_i = \pi/4$ as in equation (1.52), but tends to

$$\frac{\pi}{8} \left[\log_e \frac{\lambda_e}{L_e} \right]^{-1} \tag{4.28}$$

from below, thus providing an upper limit for the reconnection rate.

In practice, $M_i \ll 1$, for a current sheet whose width is far less than its length, (see equation (1.44)). In Figure 32 $M_{e(max)}$ is plotted as a function of (λ_e/L_e).

Comparing λ_e with the classical width η/v_∞, one finds

$$\left(\frac{\lambda_e}{\eta/v}\right) = \frac{\lambda_e}{L_e} R_{me} \cdot M_e \qquad (4.29)$$

$$\simeq \left(\frac{\lambda_e}{L_e}\right) R_{me} M_{e\,max},$$

since Mi_{max} and M_e is slowly varying compared with L/λ_e. Figure 8 can therefore be revised to include the effects of sheet width limitations. For a given value of λ_e/L_e, the curve will remain unaltered while

$$\frac{\lambda_e}{L_e} R_{me} M_{e\,max} \ll 1,$$

but when

$$\left(\frac{\lambda_e}{L_e}\right) R_{me} M_{e\,max} \gg 1,$$

the curve levels into a straight line, $M_{e\,max}$ being independent of R_{me}. A few cases are illustrated in Figure 33. For the solar flare problem, with $B_\infty = 10^{-2}$ tesla, $T = 10^6$ °K and $L_e = 10^6$ m, say, λ_e/L_e is of the order of 3×10^{-9}, and so the reconnection rate is not seriously affected for the conditions that prevail in the solar atmosphere.

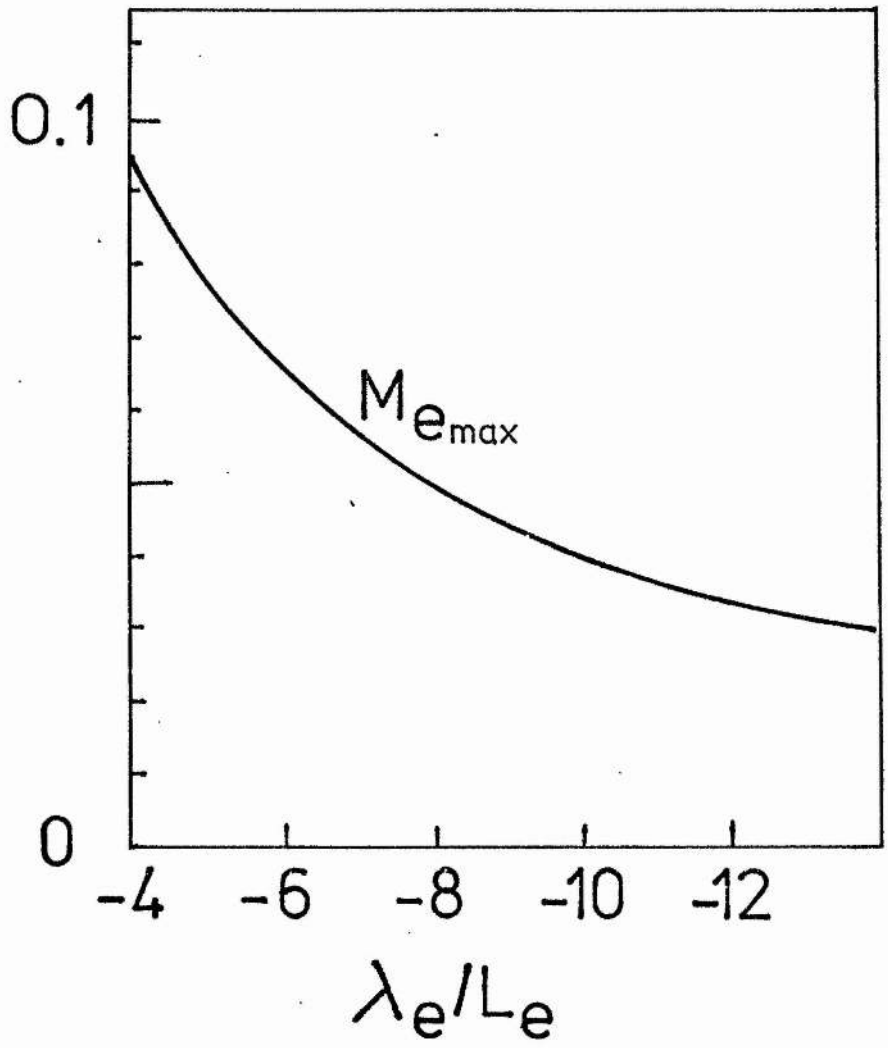

Figure 32.

The maximum Alfvén-Mach number, for $M_i=1$ as a function of λ_e/L_e.

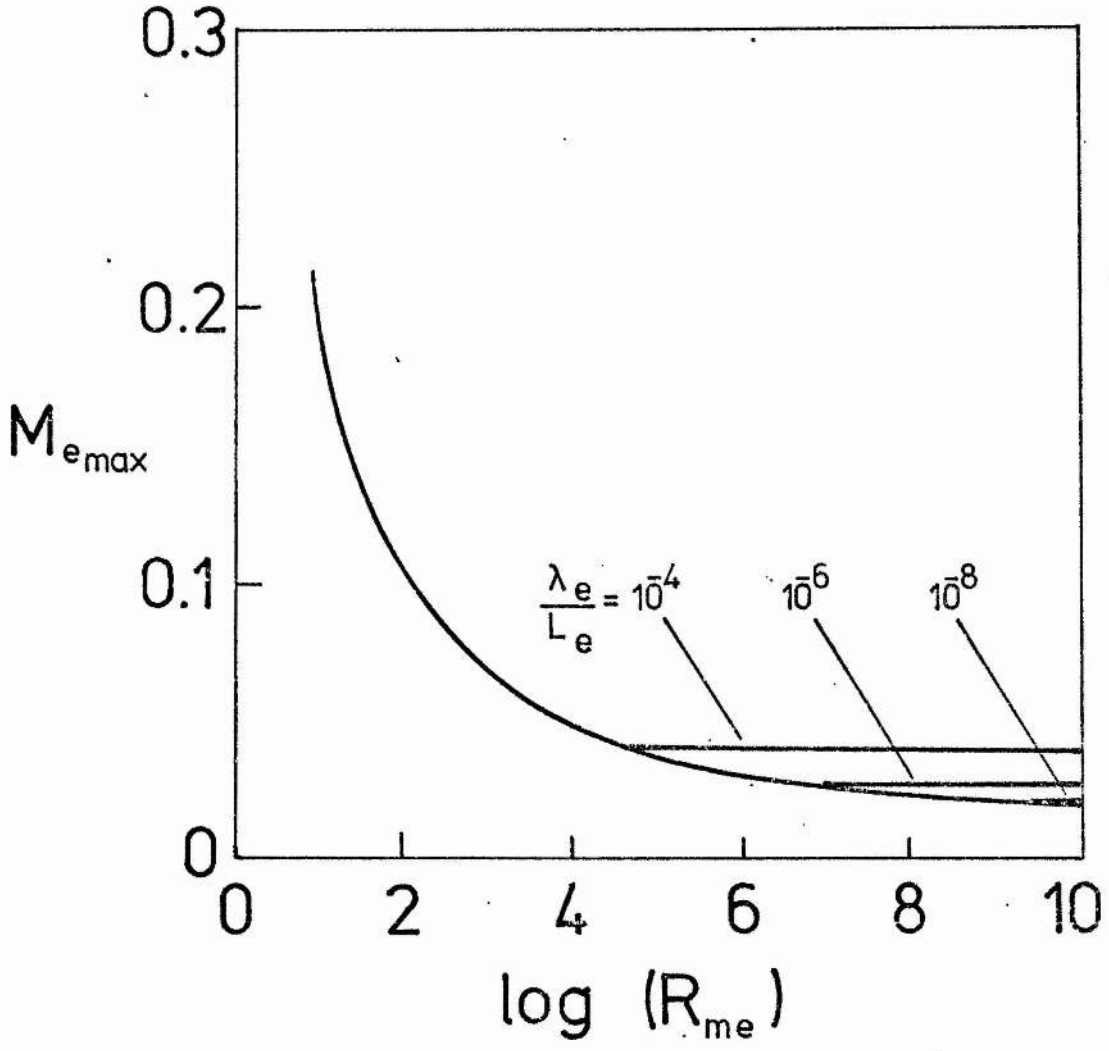

Figure 33.

The maximum Alfvén-Mach number as a function of R_{me}. The curve follows the horizontal branches when λ_e/L_e takes the values shown.

4.4. THE ONSET OF TURBULENCE.

The current density j inside the sheet is approximately

$$j = B_\infty / (\mu_0 \ell) , \tag{4.30}$$

which, after using the classical electrical conductivity (Spitzer, 1962)

$$\sigma \simeq 1.54 \times 10^{-2} T_c^{3/2} / \log \Lambda \quad (\text{mho m}^{-1}), \tag{4.31}$$

and equation (4.3), becomes

$$j = 10^{-3} v_\infty B_\infty T_c^{3/2} \quad (\text{Am}^{-2}). \tag{4.32}$$

Above some critical value

$$j_{turb} = n_c e v_{tc} ,$$

where v_{tc} is the sound speed in the centre of the current sheet, the plasma becomes susceptible to Buneman microinstability (Buneman 1959). Hence using equations (4.5) and (4.10), j_{turb} becomes

$$j_{turb} = 1.8 \times 10^{13} \frac{B_\infty^2}{T_c^{\frac{1}{2}}} \text{ A m}^{-2}). \tag{4.33}$$

Comparing equations (4.32) and (4.33), the threshold temperature for the onset of turbulence, T_{turb}, is therefore given by

$$T_{turb} = 1.34 \times 10^8 \left(\frac{B_\infty}{v_\infty} \right)^{\frac{1}{2}} . \tag{4.34}$$

The internal temperature T_c may exceed T_{turb} in two

rather different circumstances.

Firstly, as the current sheet gains in height, T_c may increase monotonically in the neighbourhood of T_{turb}, and the critical value will be slowly surpassed, the sheet passing from a stable to an unstable state on a time scale determined by the speed at which it rises.

On the other hand, if the graph of T_c becomes triple-valued, the threshold for instability may be reached on a much shorter time scale as the sheet undergoes a dynamic transition from one stable part of the curve to another (see section (1.3c)).

The dynamics of the increase in T_c between points B and C (Figure 10) presents a more complex problem than the simple energetics discussed in the preceding sections. Clearly, the sheet will never attain the new equilibrium position D on the upper branch of the curve since it becomes turbulent before reaching this point. At C the sheet becomes unstable, its width increasing with the onset of a turbulent electrical resistivity. As a result, the current density will be decreased and the sheet may remain marginally stable for temperatures above T_c.

The resulting marginally stable temperature T_c^*, may be calculated in the following manner. The electrical conductivity σ^*, corresponding to T_c^*, is expected to lie between the classical (Spitzer) value, and the turbulent value, σ_{turb}, obtained from Buneman's numerical work. Using the critical value j^* for the current density in the marginally stable sheet, the conductivity becomes

$$\sigma^* = 1.8 \times 10^{13} \frac{B_\infty}{v_\infty (T_c^*)^{1/2}} , \qquad (4.35)$$

using equations (4.33) with

$$\sigma^* = \frac{1}{\mu_0 \eta^*} \qquad (4.36)$$

and

$$\eta^* = \ell^* v$$

$$= \frac{B_\infty v_\infty}{\mu_0 j^*} \qquad (4.37)$$

Equation (4.1) may now be solved as before, using the above revisions to deduce T_c^* corresponding to h_{crit}. The resulting turbulence onset temperatures are shown on the various graphs in the next section.

4.5. RESULTS AND DISCUSSION.

In Figures 34 and 35 the general behaviour of the solution curve to equation (4.1) is demonstrated. Each figure shows a region of the (v_∞, B_∞)-plane, the parameters covering ranges that one might typically find in the solar atmosphere. For some v_∞ and B_∞, $T_c(h)$ is a monotonically increasing function (region M in the figures), while elsewhere it becomes triple-valued. The latter region may be further divided in two. In the upper portion (N_1) the threshold for the onset of instability is

crossed, as depicted in Figure 10, during the transition between stable branches of the graph. The remaining area (N_2), represents those curves which although triple-valued do not include T_{turb} within the jump between the two branches of the curve.

The (v_∞ , B_∞)-plane for which the width is limited by the electron inertial length λ_e , is shown in Figure 34. Figures 35(a) and 35(b) show the same plane, but for (a) unlimited width and (b) the ion gyroradius limit.

Several examples are taken from the (v_∞ ,B_∞)-plane drawn in Figure 34. On each one, the solution to equation (4.1) is given when (i) reconnection occurs ($v_\infty < v_{max}$) and (ii) no reconnection is allowed ($v_{max} < v_\infty < v_A$), the relevant heights for these limits corresponding to those shown in Figure 31. Below a certain height, v_∞ is of the order v_A, and neither theory is adequate; the example curves do not extend into this region. In addition, both the length of the current sheet and also the critical temperatures, T_{turb} and T_c^* , are included. The final graph in this series shows how the dominance of various terms in equation (4.1) can vary with T_c and h. These examples collectively form Figure 36.

The final Figure 37 shows the results obtained using a steadily decreasing magnetic field. Taking typical values of 10^{-1} tesla at the base of the chromosphere and 10^{-3} tesla in the corona , the field falls off as an inverse square law,

$$B_\infty (h) = \frac{A}{(h - h_0)^2} \quad ,$$

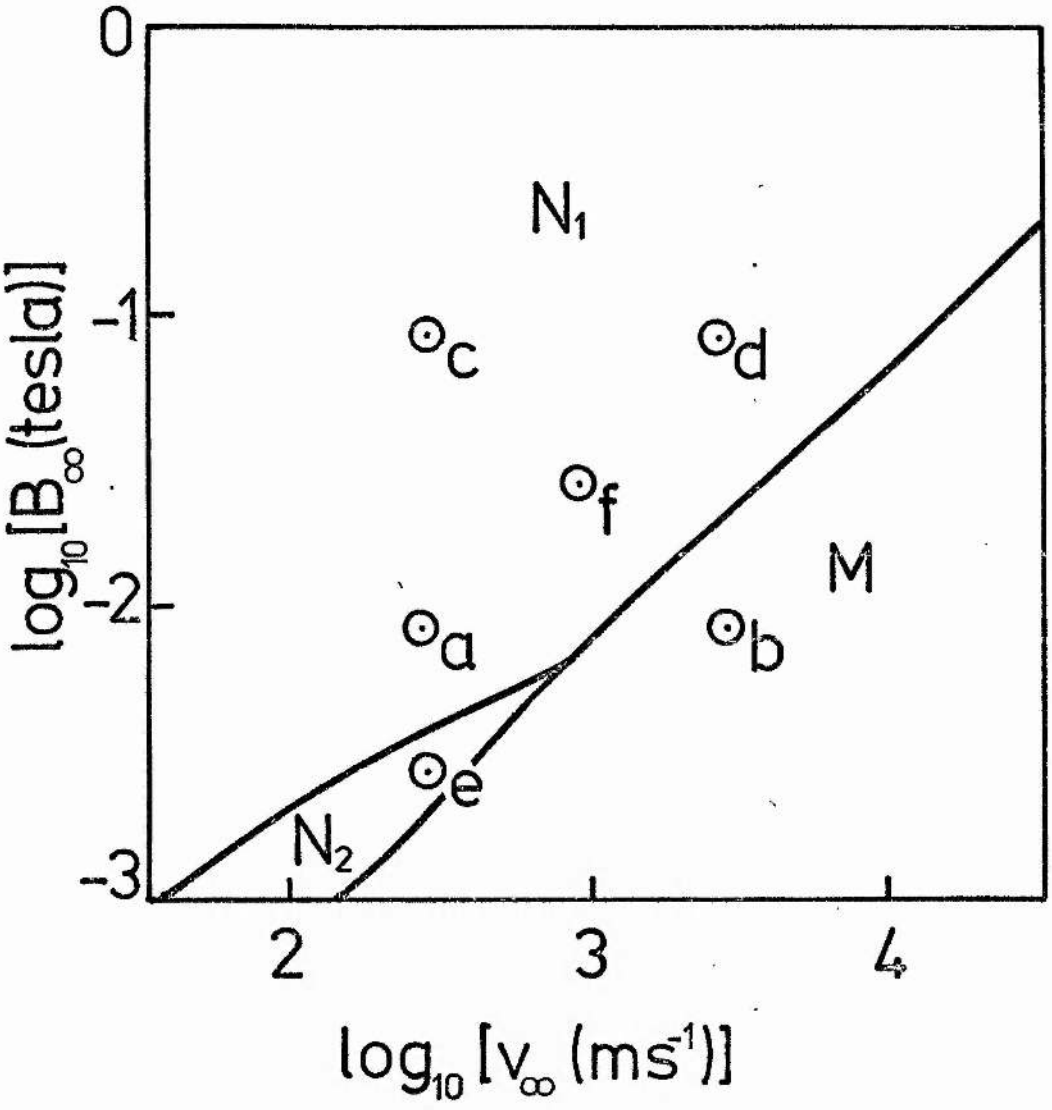

Figure 34.

The (v_∞, B_∞)-plane for current sheet widths limited by λ_e. $T_c(h)$ is singled valued in M and triple valued for some h, in N_1 and N_2. In N_1 the Buneman stability limit is surpassed as the sheet transfers between the cool and hot branches of the curve.

Examples of $T_c(h)$ are shown in Figure 36 for the points marked thus ⊙

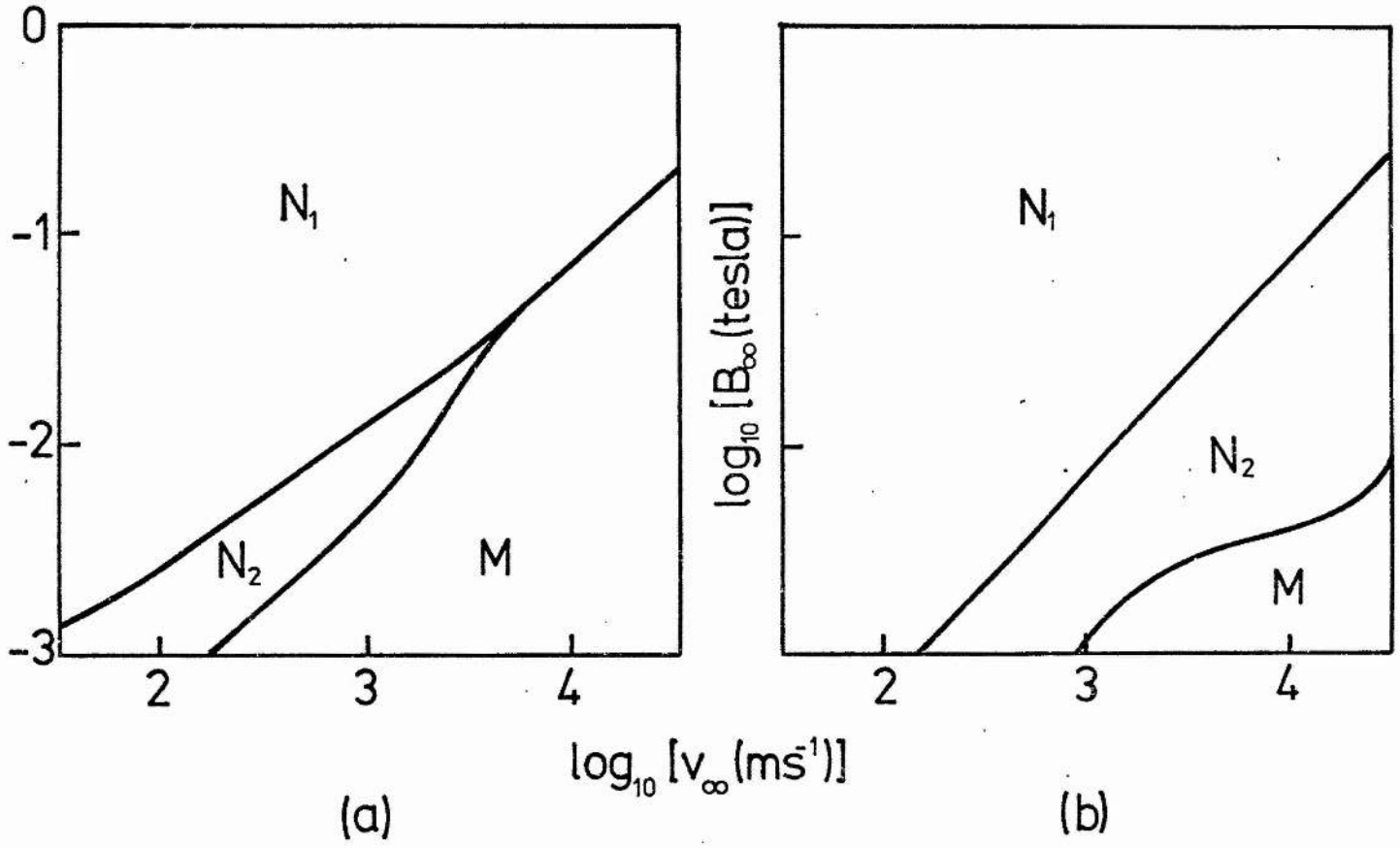

Figure 35.

The (v_∞,B_∞)-plane for (a) no current sheet width limitation, and (b) the ion gyroradius limit.

Figures 36 (a) to (f).

Figures 36(a) to (e) show the variation of the internal current sheet temperature (T_c) and length (L) with height (h). Each plot is for some pair of values of v_∞ and B_∞ indicated in Figure 34.

In Figure 36(f), the region where each term in equation (4.1) dominates is indicated for $v_\infty = 10^3 ms^{-1}$ and $B_\infty = 0.32 \times 10^{-2}$ tesla.

T_c ——————

L – – – – – –

T_c^* —·—·—·—·—

Figure 37.

The internal current sheet temperature, ($T_c(h)$) for a solar atmosphere in which B decreases in magnitude. The corresponding values of the turbulent threshold temperature, T_{turb}, are plotted.

$v_\infty = 10^2 ms^{-1}$ ——————

$v_\infty = 10^3 ms^{-1}$ — — —

$v_\infty = 10^4 ms^{-1}$ – – – – –

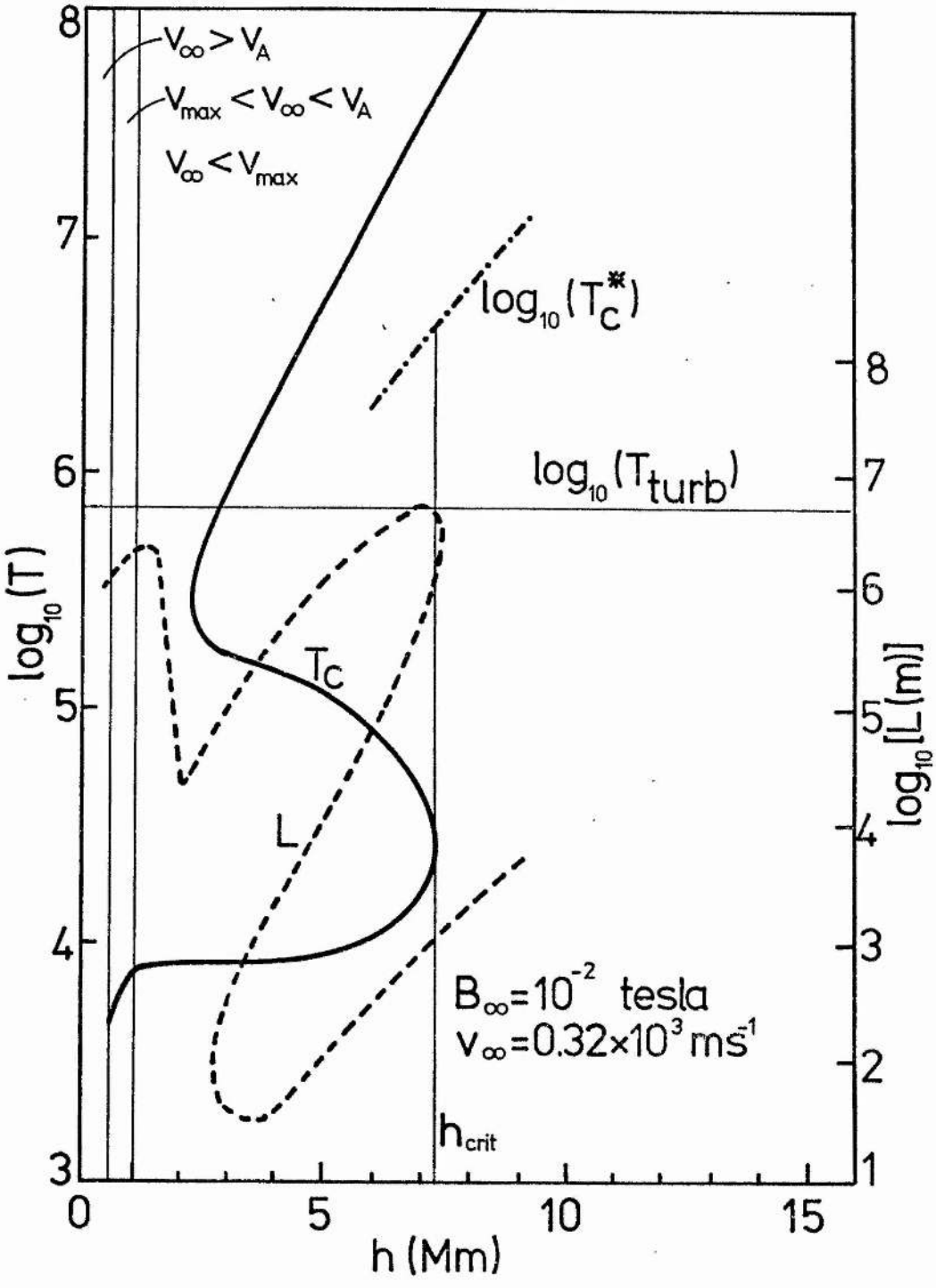
$V_\infty > V_A$
$V_{max} < V_\infty < V_A$
$V_\infty < V_{max}$
$\log_{10}(T_C^*)$
$\log_{10}(T_{turb})$
T_C
L
$B_\infty = 10^{-2}$ tesla
$v_\infty = 0.32 \times 10^3$ ms^{-1}
h_{crit}
$\log_{10}(T)$
$\log_{10}[L(m)]$
h (Mm)
0
5
10
15
3
4
5
6
7
8
1
2
3
4
5
6
7
8

36(a)

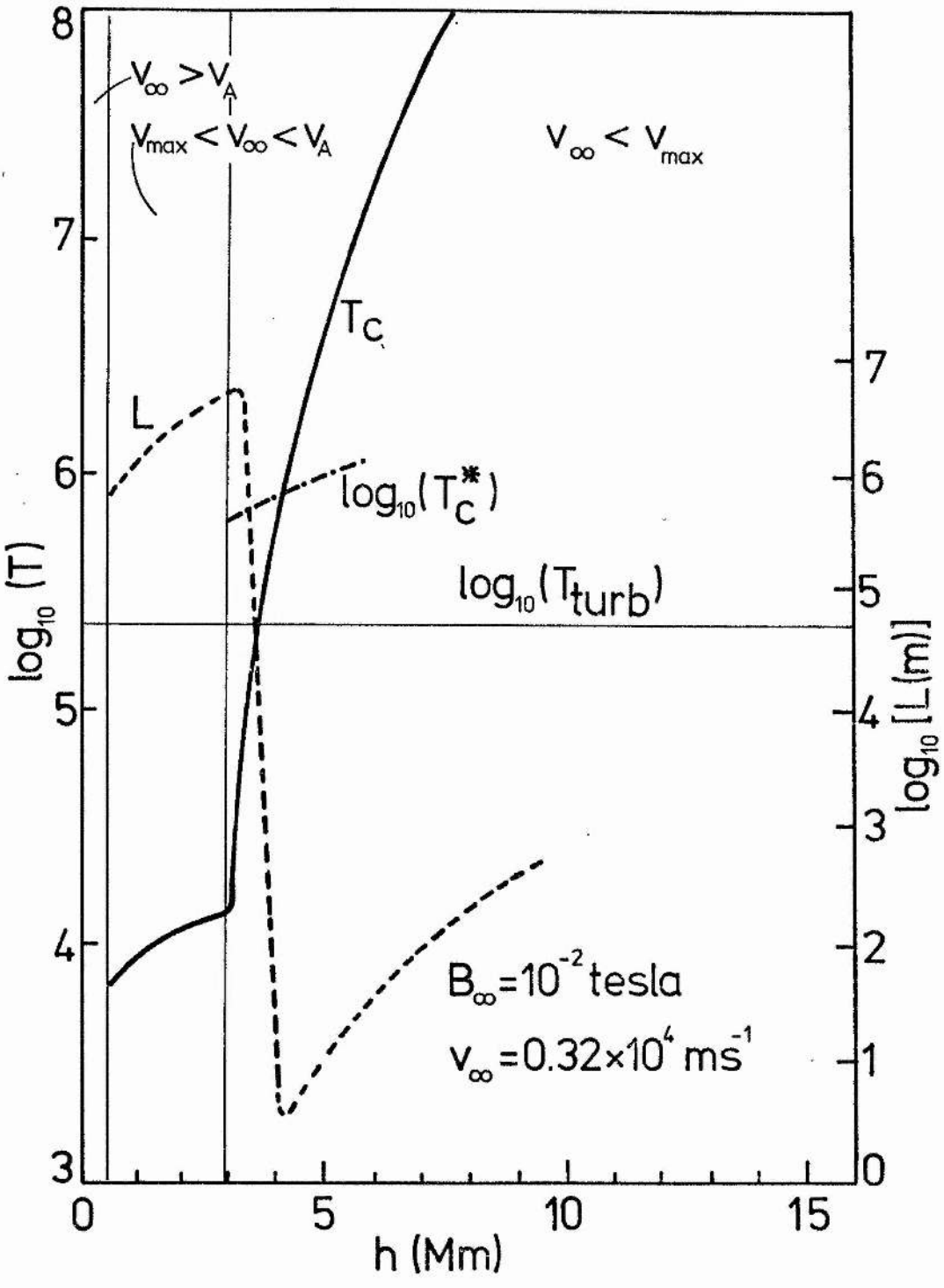
$V_\infty > V_A$
$V_{max} < V_\infty < V_A$
$V_\infty < V_{max}$
T_c
L
$\log_{10}(T_c^*)$
$\log_{10}(T_{turb})$
$B_\infty = 10^{-2}$ tesla
$v_\infty = 0.32 \times 10^4$ ms^{-1}
$\log_{10}$ (T)
$\log_{10}$ [L(m)]
h (Mm)
0
5
10
15
3
4
5
6
7
8
0
1
2
3
4
5
6
7

36(b)

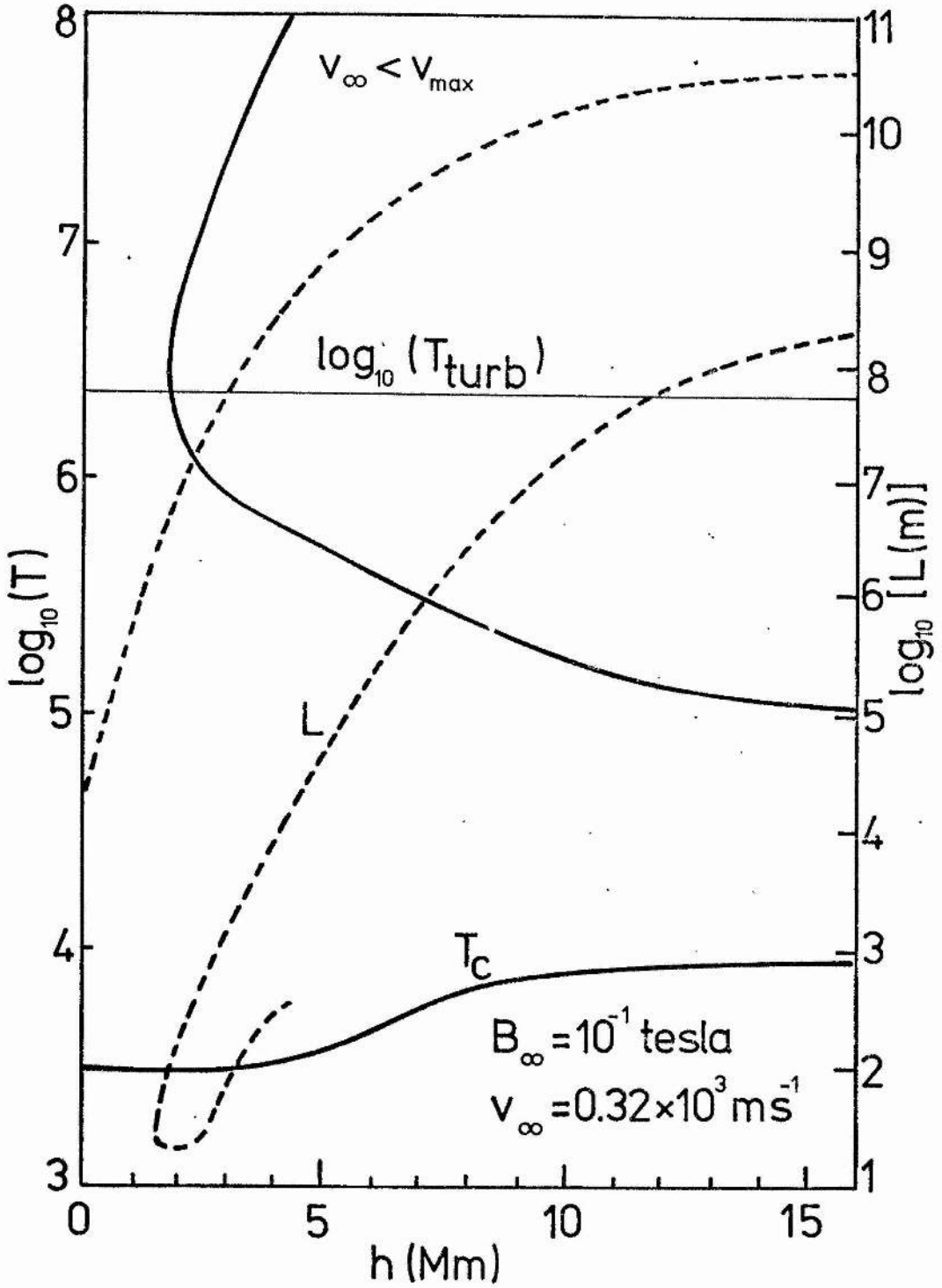
$v_\infty < v_{max}$
$\log_{10}(T_{turb})$
L
T_c
$B_\infty = 10^{-1}$ tesla
$v_\infty = 0.32 \times 10^3 ms^{-1}$
$\log_{10}(T)$
$\log_{10}[L(m)]$
h (Mm)
0
5
10
15
3
4
5
6
7
8
1
2
3
4
5
6
7
8
9
10
11

36(c)

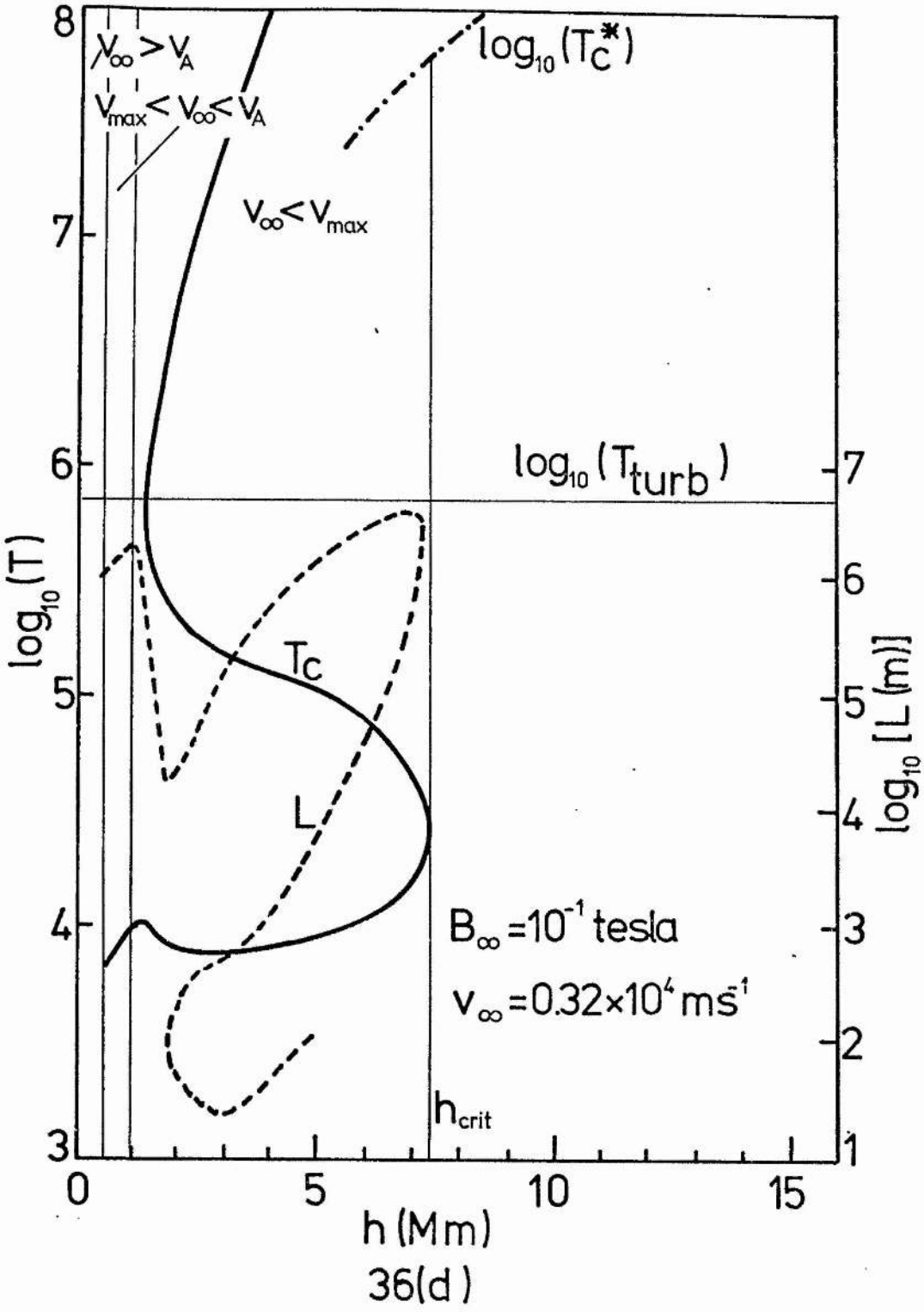
$v_\infty > v_A$
$v_{max} < v_\infty < v_A$
$v_\infty < v_{max}$
$\log_{10}(T_c^*)$
$\log_{10}(T_{turb})$
T_c
L
$B_\infty = 10^{-1}$ tesla
$v_\infty = 0.32 \times 10^4$ ms^{-1}
h_{crit}
$\log_{10}(T)$
$\log_{10}[L(m)]$
h (Mm)
36(d)
8
7
6
5
4
3
0
5
10
15

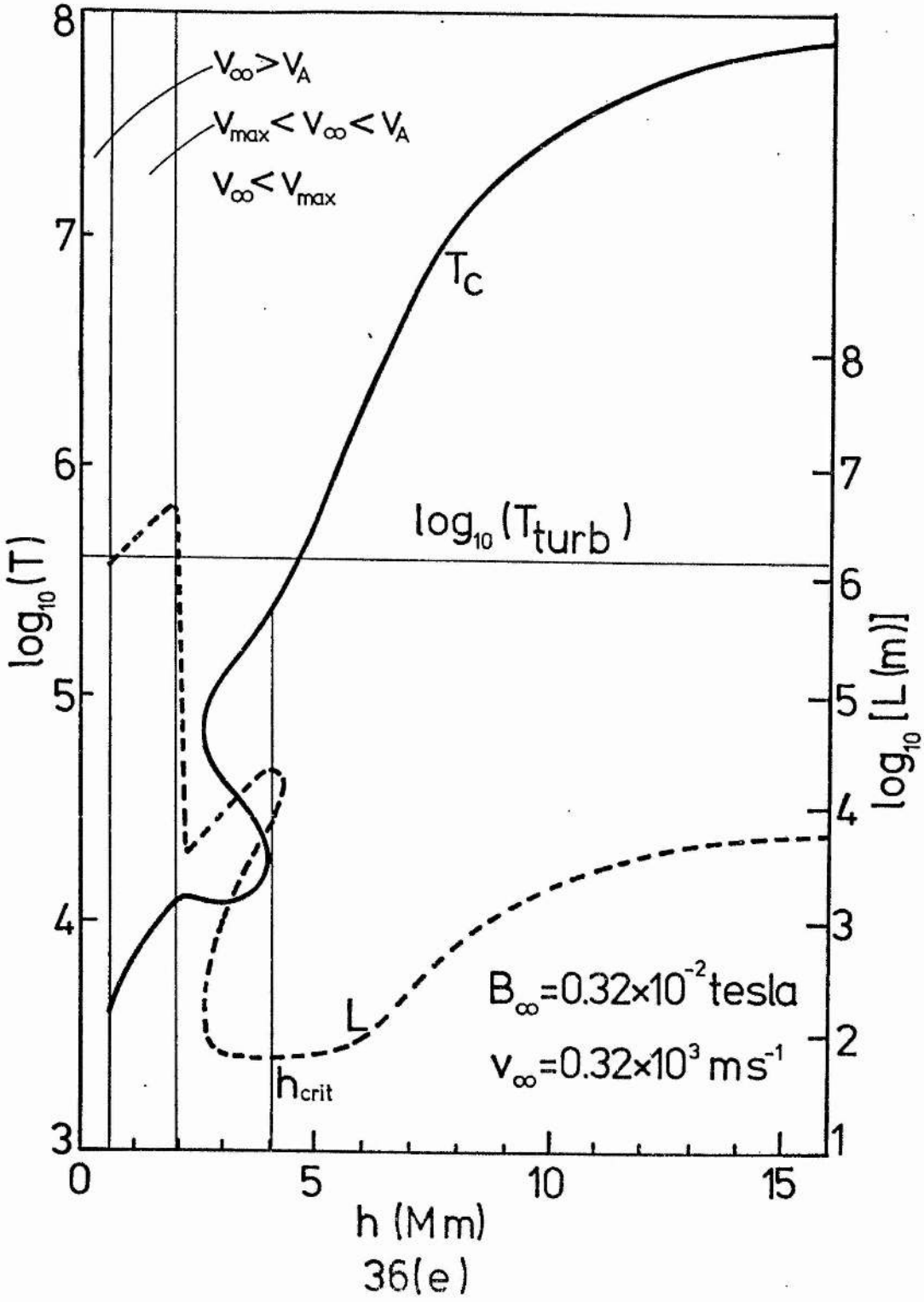
$V_\infty > V_A$
$V_{max} < V_\infty < V_A$
$V_\infty < V_{max}$
T_c
$\log_{10}(T_{turb})$
L
h_{crit}
$B_\infty = 0.32 \times 10^{-2}$ tesla
$v_\infty = 0.32 \times 10^3$ m s^{-1}
$\log_{10}(T)$
$\log_{10}[L(m)]$
h (Mm)
0
5
10
15
3
4
5
6
7
8
1
2

36(e)

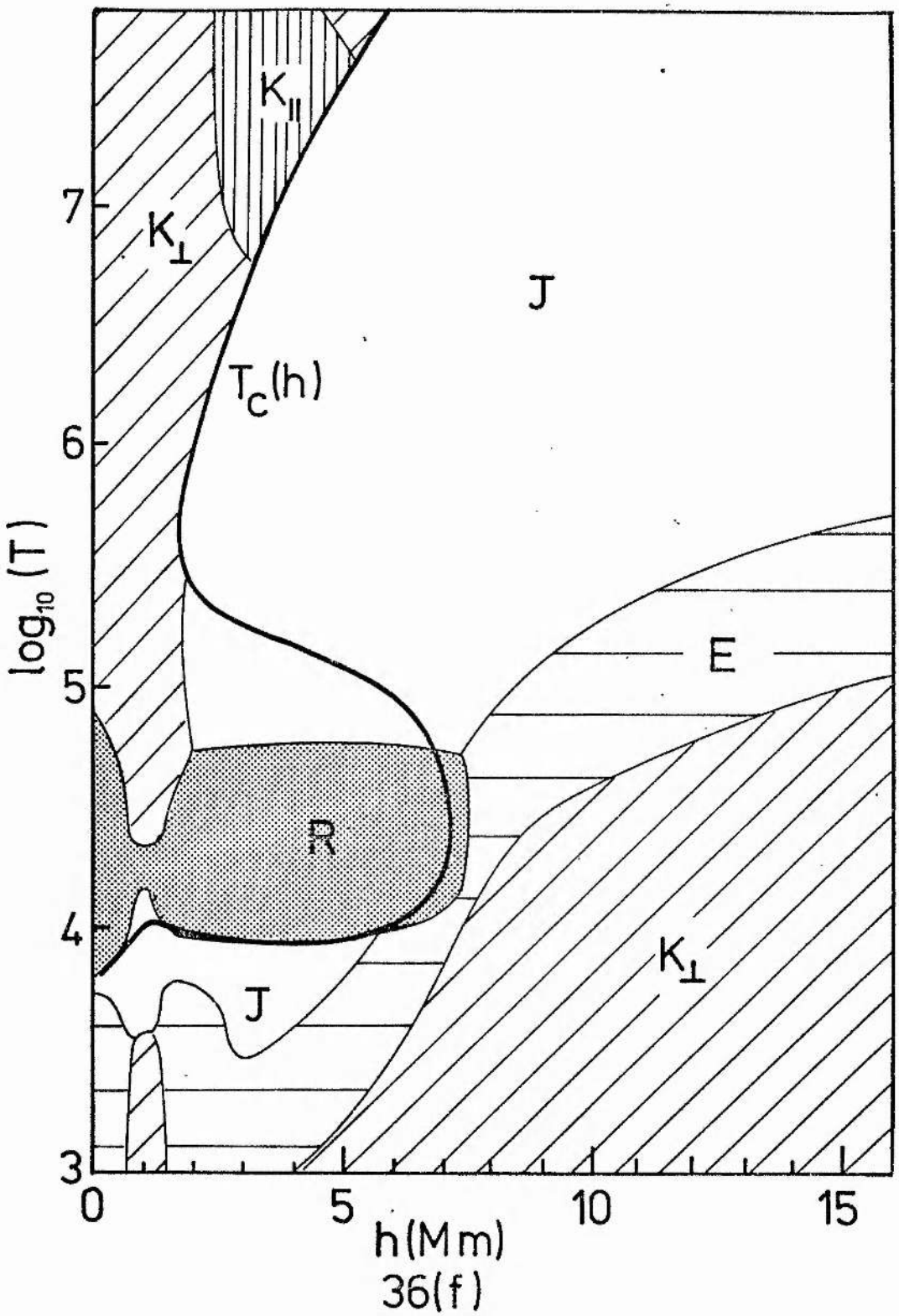
$K_{\parallel}$
$K_{\perp}$
J
$T_c(h)$
E
R
J
$K_{\perp}$
7
6
5
4
3
$\log_{10}(T)$
0
5
10
15
h(Mm)
36(f)

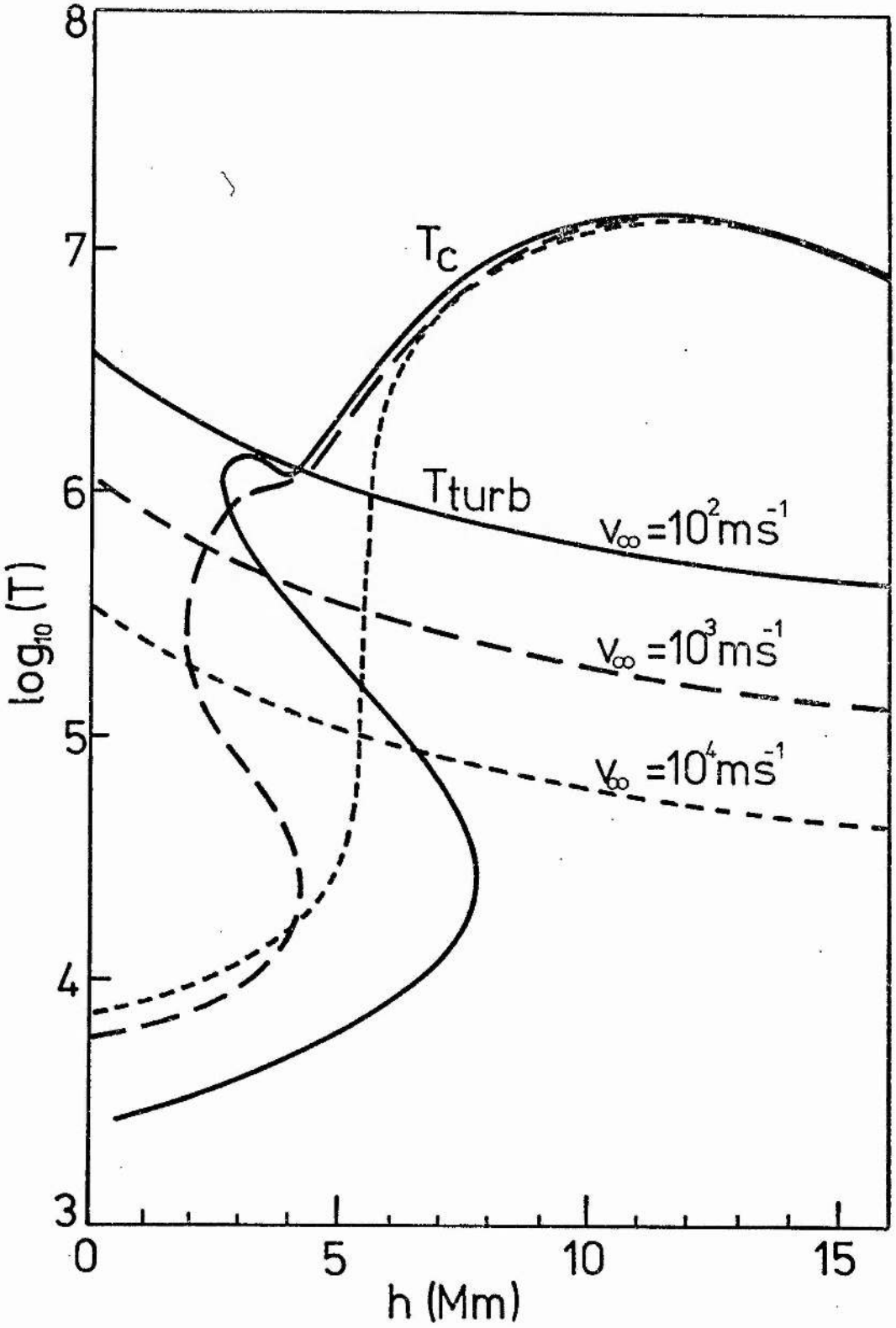
8
7
6
5
4
3
0
5
10
15
h (Mm)
log10 (T)
Tc
Tturb
v∞ =10^2 ms^-1
v∞ =10^3 ms^-1
v∞ =10^4 ms^-1

for suitable constants A and h_0, $T_c(h)$ is plotted for several values of v_∞.

Comparing these results, many interesting trends emerge.

Firstly, on the (v_∞, B_∞)-plane itself, the effect of introducing finite current sheet width limitations is to change the boundaries of the regions M, N_1 and N_2. These changes are, however, not greatly significant in view of the many approximations used, and the regions N_2 and M remain (collectively) in roughly the same position relative to N_1.

The existence of two distinct types of graph for $T_c(h)$ is, perhaps, the most important outcome of the analysis. If the onset of a microinstability is the mechanism for triggering a solar flare, then there must in consequence, be two different ways in which the trigger is accomplished. Flux emerging with a high velocity or into a relatively low ambient field will have a single valued temperature function, $T_c(h)$, or at least one which crosses T_{turb} on a stable branch. Alternatively, if the emerging flux finds itself in a region of high magnetic field strength, the current sheet so formed will become unstable in its transition from the cool branch of the $T_c(h)$ curve to the upper hotter one. This time the trigger may be expected to have a more dramatic effect, perhaps exhibiting an impulsive phase associated with the sudden heating of the current sheet.

Recent observations by Rust and Roy (1974) tend to support these ideas. In this paper, they report on their intensive study of two particular flares observed during the "Campaign for Integrated Observations of Solar Flares" (CINOF). The X-ray burst associated

with the first event was thermal in nature, and displayed a slow rise to maximum flux. This flare was observed in a region of relatively weak field strength. In contrast the second flare exhibited an impulsive phase, characterised by a large hard X-ray burst and occurred in a region of high magnetic field strength in a compact sunspot group. Despite the very different nature of the two flares, both were reported to have been triggered by the emergence of new magnetic flux.

Many flares may be categorised in this way. Zirin (1974) notes the distinction between the "slow rise" and "fast rise" flares in his classification of their physical properties. The great August 7, 1972 flare discussed in the opening chapter was of the impulsive type, and it too evolved from a region of relatively high magnetic field strength.

Some general conclusions may be drawn from Figures 36(a) to (f):

(i) If B_∞ and v_∞ increase by equal amounts the graphs of $T_c(h)$ do not vary to any great extent (This result is based on the evidence of some graphs that cannot be included here. However, compare graphs 36 (a), (d) and (f), all of which lie on a line in the (v_∞, B_∞) plane.)

(ii) The critical height at which the sheet becomes unstable varies considerably as either v_∞ decreases or B_∞ increases, h_{crit} increases in value, often giving a site for the flare which is well into the corona, (Figure 36(c)) for example. For B_∞ and v_∞ close to the dividing line between regions M and N_1, h_{crit}

is typically 7.5×10^6 m above the photosphere.

(iii) The Buneman instability threshold T_{turb} increases with increasing B_∞ and v_∞ .

(iv) For large field strengths and low velocities (Figure 36 (c), the sheet length (L) exceeds the upper realistic value of 10^7 to 10^8 m , and the present theory may be invalid in this regime. Figure 36(e) is included as an example in which $T_c(h)$, although triple-valued, is not of the "impulsive trigger" type.

The results of Figure 37 for the height-dependent magnetic field are qualitatively not unlike the previous ones. As v_∞ increases, the curve is progressively flattened from its triple-valued shape to a single-valued curve. One difference between this and the previous set of graphs lies in the behaviour of the current sheet temperature at large heights. Now, instead of increasing rapidly along the upper branch of the curve, it reaches a maximum around 10^7 K. The actual value of this maximum temperature will depend on the particular model one takes for B_∞ , but it is not significantly dependent upon v_∞ .

In conclusion, it must be stressed again that these results are derived from order of magnitude relationships and should therefore be interpreted in the same spirit. Therefore, while the details of each graph may not be too significant, the overall pattern that emerges from them may be.

CHAPTER 5.

CONCLUSION AND SUGGESTIONS FOR FURTHER WORK.

Certain aspects of current sheet theory have been investigated in this thesis and applied to the solar flare problem. These applications have dealt primarily with the early stages of flares, that is, the storage of energy in the preflare magnetic field, and a trigger mechanism. The techniques used have varied greatly. They include the more exacting analytical approach in Chapters 2 and (parts of) 3, numerical techniques for the remainder of Chapter 3 and the approximate analysis in the final chapter on trigger mechanisms.

The sections dealing with two-dimensional current sheets leave little doubt that these are a viable and efficient energy storage mechanism, provided that the sheet is formed at a much faster rate than it can be destroyed by diffusion and reconnection. At the same time, a method is developed for handling curved current sheets such as one would expect to find occurring naturally. The stability of these configurations has not been questioned in this chapter, and it would be of interest to determine the stability criteria for a curved current sheet. The sheet may, for example, become unstable for some critical value of its curvature.

A further application of the section on current sheet formation between a dipolar and uniform field has already been mentioned. This is the problem of current sheet formation in the

terrestrial magnetosphere. If, instead of increasing the moment of the dipole in a uniform stationary field, the dipole were to be kept fixed while the ambient field moved towards it, then a current sheet may again form with a topology not unlike the one shown in Figure 17(b). At least, this would be the sort of picture one may expect in the upper-half plane. Below the real axis, the passing ambient field would tend to draw out the dipolar field into a somewhat different configuration. The model may be used to simulate the formation of current sheets in the dayside region between the earth's (approximately dipolar) field, and the solar wind.

In Chapter 3, an attempt is made to break away from the limitations imposed by considering two-dimensional structures. The gain in generality in that sense has been shown to be costly in terms of the greatly increased complexity of the field equations and the need to resort to numerical methods to complete the problem. Comparing the results for those obtained for the symmetric, two-dimensional case, one sees that the current sheet formed is larger in three dimensions. This increase is mainly due to the larger values for the outer perimeter of the sheet, but, as the current density tails off rapidly at this edge, the result should not be regarded as highly significant.

An alternative approach to the three dimensional problem would be to drop the more rigorous treatment in favour of an approximate analysis. If the current sheet were represented simply by a line current, the field sufficiently far away would assume the same form as in the more exact situation. With this model, the restrictions

of symmetry could be relaxed and the results more realistically applied.

The flare trigger mechanism studied in Chapter 4 is very much an order-of-magnitude theory. However, within this stringent limitation, some important ideas have emerged, the main ones being: (i) solar flares may well be triggered in the manner described and (ii) that the trigger can be activated in two distinct ways, each producing its own characteristics during the initial stages of the flash phase. Several avenues of research may be followed from this initial theory.

Certainly, it would be useful to obtain an analytic solution to equation (4.1), but to tackle the entire equation analytically would be a formidable task. One approach might be to split the (T_c,h) plane as, for example, in Figure 36(f) and solve the reduced energy equation (in each area) with only the dominant terms appearing. The solution for the entire range of values could then be constructed by matching techniques. Alternatively, the full equation could be solved numerically by using finite difference formulae for the derivatives and integrating over a thin rectangular box representing the current sheet.

The dynamics of the transition between stable states, too, requires further attention. It was found in section (4.4), for instance, that the sheet would heat up to some marginally stable temperature T_c^*. This result, again, is only based upon order-of-magnitude arguments and should be further investigated.

Finally, it was assumed that the Buneman microinstability was responsible for the onset of turbulence in the sheet. However, other microinstabilities may exist with even lower temperature thresholds. Furthermore, the sheet may, possibly before the onset of turbulence, become so thin in comparison with its length that the tearing mode instability (Furth et al. 1963) may occur to disrupt the current sheet.

REFERENCES

Alfvén, H. and Carlqvist, P. (1967) Solar Phys. 1, 220-228.

Anzer, U. (1968) Solar Phys. 3, 298-315.

Anzer, U. (1973) Solar Phys. 30, 459-471.

Baum, P.J., Bratenahl, A., Kao, M. and White, R.S., (1973(a)) Phys. Fluids 16, 1501-1504.

Baum, P.J., Bratenahl, A. and White, R.S., (1973(b)) Radio Sci. 8, 917.

Boyd, T.J.M. and Sanderson, J.J. (1969) "Plasma Dynamics". Nelson.

Bratenahl, A. and Baum, P.J. (1976) "Impulsive Flux Transfer Events and Solar Flares", (submitted to Geophys. J. Roy.Astron.Soc.).

Brown, J.C. (1975) I.A.U. Symposium No. 68, 245-282. (Ed. Kane).

Buneman, O. (1959) Phys. Rev. 115, 503-517.

Chapman, S. and Kendall, P.C. (1963) Proc. Royal Soc. A. 271, 435-448.

Coulson, C.A. (1958) "Electricity" (5th edition), Oliver and Boyd, Edinburgh and London.

De Jager, C. (1969) "Solar Flares and Space Research". De Jager and Švestka (eds.), North Holland Publ. Co., Amsterdam.

Dodson, H.W. and Hedeman, E.R. (1970) Solar Phys. 13, 401-419.

Dungey, J.W. (1953) Phil. Mag. 44, 725-738.

Ecker, (1972) "Theory of Fully Ionized Gases". Academic Press.

Ferraro, V.C.A. and Plumpton, C. (1966) "Magneto-fluid Mechanics". Oxford University Press.

Fritzova-Svestkova, L., Chase, R.C. and Svestka, Z. (1976) Submitted to Solar Physics.

Fukao, S. and Tsuda, T. (1973(a)) J. Plasma Phys. 9, 409-427

Fukao, S. and Tsuda, T. (1973(b)) Planet. Space Sci. 21, 1151-1178.

Furth, H.P., Killeen, J. and Rosenbluth, M.N. (1963) Phys. Fluids 6, 459-484.

Giovanelli, R.G. (1939) Astrophys. J. 89, 555.

Golub, L., Krieger, A.S., Silk, J.K., Timothy, A.F. and Vaiana, G.S. (1974) Astrophys. J. 189 , L93-L97.

Green, R.M. (1965), I.A.U. Symposium No. 22, 398-404.

Green, R.M. and Sweet, P.A. (1966) Astrophys. J. 147, 1153-1156.

Harvey, J.W. (1974) in "Flare-related magnetic field dynamics", Y. Nakagawa and D.M. Rust (eds.), NCAR, Boulder, Colorado.

Heyvaerts, J.H. and Priest, E.R. (1976) Solar Phys. (submitted for publication).

Heyvaerts, J.H., Priest, E.R. and Rust, D.M. (1976) Astrophys. J. (In press).

Hildner, E. (1974) Solar Phys. 35, 123-136.

Isaacson, E. and Keller, H.B. (1966) "Analysis of Numerical Methods", Wiley and Sons, Inc., New York.

Jeans, J.H. (1911)"Electricity and Magnetism", C.U.P.

Low, B.C. (1973) Astrophys. J. 181, 209.

Matres, M.J.,Michard, R., Soru-Escaut, I. and Axisa, F. (1972) Nature (Physical Sci.) 236, 25-27.

Matres, M.J., Michard, R., Soru-Escaut, I. and Tsup, T. (1968) I.A.U. Symposium No. 35, 318-325.

Matres, M.J., Soru-Escaut, I. and Rayrole, J., (1971) I.A.U. Symposium No. 43, 435.

Moreton, G.E. and Ramsay, H.E. (1960) Publ. Astron. Soc. Pacific 72, 357-358.

Muskelishvili, N.I. (1946) "Singular Integral Equations" 2nd edition, (Translation by Radok and Woolnough, Dept. of Supply and Development, Aeronautical Research Lab., Melbourne, Australia, 1949).

Petscheck, H.E. (1964) "AAS/NASA Symposium on the Physics of Solar Flares." (ed. Hess) 425-439.

Priest, E.R. (1972) Mon.Not. Royal Astron. Soc. 159, 389-402.

Priest, E.R. (1976) "The Solar Flare Phenomenon", Proceedings of the Solar-Terrestrial Physics Symposium, Boulder, 1976.

Priest, E.R. and Heyvaerts, J.H. (1974) Solar Phys. 36, 433-442.

Priest, E.R. and Raadu, M. (1975) Solar Phys. 43, 177-188.

Priest, E.R. and Soward, A.M. (1976) I.A.U. Symposium No. 71 "Basic Mechanisms of Solar Activity", (Bumba and Klaczek eds.).

Roberts, B. and Priest, E.R. (1975) J. Plasma Phys. 14, 417-431.

Roberts, P.H. (1967) "An introduction to Magnetohydrodynamics", Longmans, London.

Rust, D.M. (1972) Solar Phys. 25, 141-157.

Rust, D.M. and Hegwen, F. (1975) Solar Phys. 40, 141-157.

Rust, D.M. and Roy, J.R. (1974), U.S.A.F. Cambridge Research Laboratories, Environmental Research Paper No. 474.

Severny, A.B. (1953) Izv. Krym. Astrofiz. Obs. 20, 22.

Severny, A.B. (1959) "Solar Flares and Sp. Research" (De Jager and Svestka eds.) North Holland Publ. Co., Amsterdam.

Sheeley, N.R., Bohlin, J.D., Brueckner, G.E., Purcell, J.D., Scherrer, V. and Tousey, R. (1976) "XUV Observations of Coronal Magnetic Fields", E.O. Hulbert Center for Space Research, Washington D.C.

Smith H.J. and Smith E.V.P. (1963) "Solar Flares" MacMillan, New York.

Sonnerup, B.U.Ö. (1973) N.A.S.A. Symposium on "High Energy Phenomena on the Sun", Greenbelt, Maryland (NASA-GSFC X-693-73-193), 357-376.

Soward, A.M. and Priest, E.R. (1976) Phil. Trans. Royal Soc. (In press).

Spitzer, L. (1962) "Physics of Fully Ionized Gases", Interscience, New York.

Sturrock, P.A. (1972) Solar Phys. 23, 438-443.

Švestka, Z. (1973) Solar Phys. 31, 389-400.

Sweet, P.A. (1958(a)) I.A.U. Symposium No. 6, 123-134 (Lenhert ed.)

Sweet, P.A. (1958(b)) Nuuvo Cimento, Suppl. 8, Ser. X, 188-196.

Syrovatskii, S.I., (1976) Soviet Astron. letters 2, 35-38.

Vasyliunas, V.M. (1975), Rev. Geophys. Space Phys. 13, 303-336.

Vorpahl, J.A. (1973) Solar Phys. 28, 115-122.

Voslamber, D. and Callebaut, D.K. (1962) Phys. Rev. 128, 2016-2021.

Woltjer, L. (1958(a)) Proc. Nat. Acad. Sci. (U.S.A.) 44, 489-491.

Woltjer, L. (1958(b)) Astrophys. J. 128, 384-391.

Yeh, T. and Axford, W.I. (1970) J. Plasma Phys. 4, 207-229.

Zirin, H. (1966) "The Solar Atmosphere", Blaisdell Publ. Co., Massachusetts.

Zirin, H. (1974) Vistas Astron. 16, 1-34.

Zirin, H. and Taraka, K. (1973) Solar Phys. 32, 173-207.